Dimensional Dependence of Light Interaction with Nanowires

A Thesis

Submitted to the Faculty

of

Drexel University

by

Zhihuan Wang

in partial fulfillment of the

requirements for the degree

of

Doctor of Philosophy

June 2017

DEDICATIONS

This thesis is dedicated to my family. Their unconditional support and love was the foundation of success for my graduate study. I want you to know that I love you so much and this thesis was only possible thanks to you.

ACKNOWLEDGMENTS

This dissertation summarized the research work I have accomplished during my graduate study in Drexel University. Over all these years, I obtained tremendous help from all the people around and I cannot leave the dissertation without expressing my gratitude to them.

This work would not have been possible without the support of my advisor, Dr. Bahram Nabet. His guidance helped to shape and provided much needed focus to my work. I would also like to thank my dissertation committee of Dr. Timothy Kurzweg, Dr. Baris Taskin, Dr. Nagarajan Kandasamy, and Dr. Goran Karapetrov for their support and insight throughout my research.

Many thanks to our generous collaborators, Dr. Adriano Cola, Dr. Anna Persano, Dr. Paola Prete at IMM-NCR in Italy, Dr. Nico Lovergine at University of Salento in Italy and Dr. Marc Currie from Navel Research Laboratory in Washington D.C. for their tremendous efforts in fabrication of the AlGaAs/GaAs core-shell nanowires and electro-optically sampling, micro-photoluminescence measurements of the devices. Although, I have not had the opportunity of meeting them yet, it is still a great pleasure to communicate with them in Email and I appreciate their valuable thoughts and discussions in many of the experimental results. I would also like to dedicate many thanks to Dr. Fernando Camino, Dr. Aaron Stein, Dr. Chang-Yong Nam, Dr. Mircea Cotlet and many other staffs at CFN of Brookhaven National Laboratory in Long Island for their assistance and suggestions in characterizing the devices.

I would also like to thank my friends in the Photonics Lab for all the help and support they provided, and especially for providing such a friendly and awesome place to work and study at. Pouya Dianat, Weston Aenchbacher and Shrenik Vora have spent countless hours listening to me talk about my research, helping me flesh out my ideas. And a special thanks to Jiajia Liu for accompanying me

during all these years and bringing countless happiness to my life.

Finally, my parents deserve my most sincere gratitude. I appreciate you spent one or two months each year to be in the states with me, and they always believe in, encourage and love me even when they live on the other side of the earth.

TABLE OF CONTENTS

LIST OF TABLES

LIST OF FIGURES

ABSTRACT

Dimensional Dependence of Light Interaction with Nanowires
Zhihuan Wang
Advisor: Dr. Bahram Nabet

Semiconductor nanowires have been used in a variety of passive and active optoelectronic devices including waveguides, photodetectors, solar cells, LEDs, Lasers, sensors, and optical antennas. We review the optical properties of these nanowires in terms of absorption, guiding, and radiation of light, which may be termed light management. Analysis of the interaction of light with long cylindrical structures with sub-wavelength diameters identifies radial resonant modes, such as Leaky Mode Resonances, or Whispering Gallery modes. The two-dimensional treatment should incorporate axial variations in volumetric modes which have so far been presented in terms of Fabry-Perot, and Helical resonance modes. We report on FDTD simulations with the aim of identifying the dependence of these modes on: geometry (length, width), tapering, shape (cylindrical, hexagonal), core-shell versus core-only, and dielectric cores with semiconductor shells. This demonstrates how NWs form excellent optical cavities without the need for top and bottom mirrors. However, optically equivalent structures such as hexagonal and cylindrical wires can have very different optoelectronic properties meaning that light management alone does not sufficiently describe the observed enhancement in upward (absorption) and downward transitions (emission) of light in nanowires; rather, the electronic transition rates should be considered. We discuss this rate-management scheme showing its strong dimensional dependence, making a case for photonic integrated circuits that can take advantage of the confluence of the desirable optical and electronic properties of these nanostructures.

CHAPTER 1

INTRODUCTION

The practice of staining galss for decorative purposes dates to ancient Rome, but the investigation of light matter interaction starts even back to the begining of history for human beings, when ancient lifes first notice the existence of sun or the first time to use torch for hunting. People never stop to study how the light interact with our world, meanwhile, implement our understanding to build a better world with lighting technology. The stained-glass windows such as the one inside of the St. Patrick's Cathedral in Fig. 1.1 served as a 'poor man's Bible' in the Middle Ages, allowing believers who could not read Latin to learn the story of the Gospels. The term stained glass refers to glass that has been coloured by adding metallic salts during its manufacture. Then this coloured glass is crafted into stained glass windows in which small pieces of glass are arranged to form patterns or pictures. Even nowadays, people are still surprised about how beautiful they are and wondering how the light interact with these pieces of art crafts. Besides the arts, lighting technology is also evolving very rapidly, from the ancient torchs to the bulb that Thomas Edison invented and to the modern LEDs such as the one in Fig. 1.1. From balckbody radiation to electroluminescence, i.e., from thermal radiation to electrons-holes recombination, we are now capable to generate light more clean and more efficiently.

Now we find ourselves living through a new revolution in the age of information technology, one with consequences every bit as dramatic and likely even more profound as the data transmission by light. Electrons served us very well for the recent few decades, until the explosion of data growth nowadays. The storage and the transmission of data consumed large amount of power and

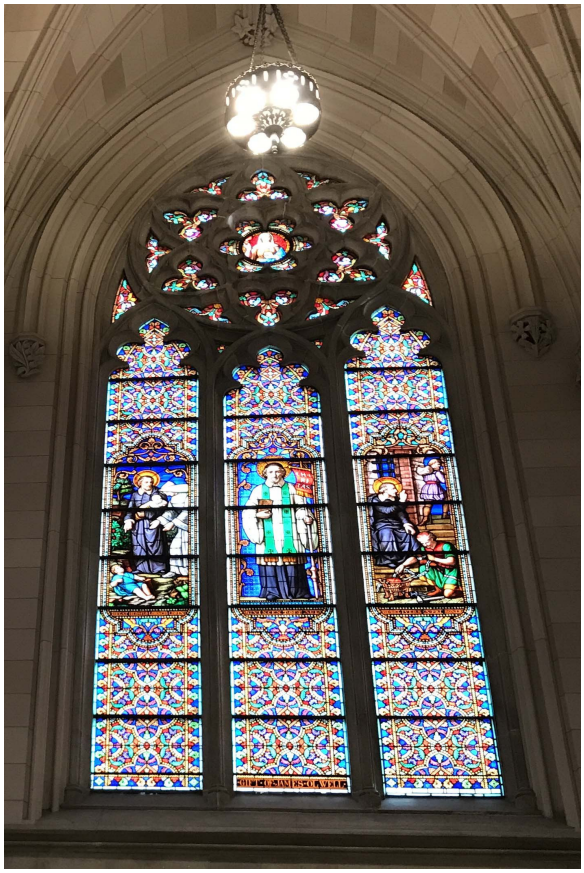

Figure 1.1 The Stained-glass window and the top modern lamps inside of the St. Patrick's Cathedral, 5th Ave, New York, NY.

time, simultaneously. Meeting the energy needs of the commnuication of information, together with storage and computation form a "grand challenge" of the information age.

One good example of huge amount of power comsumption by data transmission and coputation is the data centers, which currently consume 1.5% of global energy production, and up to approximately 4% of U.S. energy produced. Though the statistics seems small, a 1000 times increase in the volume of data is predicted by 2025. Google data center alone consumes enough electricity to power 200,000 homes, since an average Google search or a YouTube video or a message through Gmail uses 0.3 watt-hours of electricity. Having efficient data computaion and transmission tools will greatly reduce the total data center power consumption into a greener number. And the data pipelines of light can certainly be very helpful in this regime.

1.1 Background

1.1.1 Photonics and Optoelectronics

Photonics involves the generation, control and detection of light waves and photons, which are particles of light, in free space or in matter. Optoelectronics is the study and application of effects related to the interaction of light and electronic signals, and usually considered a sub-field of photonics. Both photonics and optoelectronics study the light, and explore a wider variety of wavelengths besides visible lightwave range, from gamma rays to radio, including X-rays, ultraviolet and infrared light.

The invention and development of solar cells[3,4], photodetector[5,6], modulators[7,8], LEDs[9–11] and lasers[12,13] certainly set the example of breakthroughs due to the manipulation of photons in thin films and semiconductor bulk crystals. The continuing success of photonic technologies relies on the discovery of new optical materials and the miniaturization of optoelectronic devices that feature better performance, low cost and low power consumption. For the last few decades, countless efforts in nano-scale materials and devices research has created a rich collection of nanostructures where size, shape and composition can be readily controled. Many such nanostructures exhibit fascinating optical properties that could have significant impact in the future for photonic technology.

1.1.2 Core-Shell Nanowires

The primary principle for constantly miniaturizing the device is not only about the size, but also to have better electronic and optical properties. And this is achieved by quantization, or to be more specific, the confinement of electrons and photons. At the very dawn of electronics, the idea of using heterostructures (i.e., the structure with two layers or regions of dissimilar crystalline semiconductors) has emerged. After Shockley proposed the idea, Alferov and Kroemer introduced the concept that heterojuctions could possess high injection efficiencies in comparison with homojunctions, and we know now which is due to the confinement of carriers[14]. It would be very difficult today to imagine solid-state physics without semiconductor heterostructures for both electronc-based and optical-based applications. The heterostructures and especially double heterostructures, including quantum wells, nanowires, and quantum dots, are the fundamental building blocks for current nanoscience research.

Quantum well is a potential well which confines particles to only move freely in two dimensions in stead of three dimensions, by forcing them to occupy a planar region. These wells are formed in semiconductors by having a narrower bandgap material sandwiched between two layers with wider bandgap materials. Electrons in quantum wells are confined in two dimensions either naturally or by doping the barrier of a quantum well, thus a two-dimensional electron gas (2DEG) may be formed at the heterointerface. Not only an increasing of the density of states, but also a better performance in optoelectronics devices such as laser diodes, High Electron Mobility Transistors (HEMTs), photodetectors, and solar cells.

Quantum dots, as another most common nanostructure in semiconductor physics, exhibit much more enhanced optical properties. They are normally only several nano-meters in size, and either synthesized or self-assembled into a bulk solid. As the particles in the quantum dots are confined in three dimensions, which leave them zero degree of freedom. As a result, the density of states changed to a delta function compare to a smooth square root dependence that is found in bulk materials. The narrower peak spectra and larger magnitude of intensity make them even better candidates in

the application of solar cells, lasers and light emitting diodes (LEDs).

However, since the introduction in the 1990s, another important class of semiconductor nanostructures has emerged: structures with cross-sections of tens or hundreds of nano-meters and lengths up to several micro-meters. These structures are named as 'nanowires'[15] different from quantum dots as they are confined only in two dimensions, thus allowing electrons, holes or photons to propagate freely along the third dimension. Besides their own outstanding electro-optical properties, the high-aspect-ratio of these new semiconductor nanostructures allows for the bridging of the nanoscopic and macroscopic world. As Dr. Peidong Yang said in their review paper, "This nano-macro interface is fundamental to the integration of nanoscale building blocks in electrical or optoelectronic device applications. Conventional photonic platforms often consist of features with large aspect-ratios such as interconnects and waveguides, typically with micrometre dimensions. Thus, when semiconductor nanowires emerged they were immediately recognized as one of the essential building blocks for nanophotonics." [16]

The development of sophisticated nanowires growth techniques[17,18], either bottom-up[19,20] or top-down[21], has stimulated a large body of new work in semiconductor nanowires over the last twenty years or so. Previously, the research activities focus on the growth of higher quality nanowires[22] and the variation of materials. At that time, most of the nanowires are core-only with ZnO[22], GaAs[23], Si[24], or Ge[25]. However, later on, researchers found out that growing an additional layer of shell can increase quantum yield by passivating the surface trap states. In addition, the shell provides protection against environmental changes, photo-oxidative degradation, and provides another route for modularity. Precise control of the size, shape and composition of both the core and the shell enable the emission wavelength to be tuned over a wider range of wavelengths than with either individual semiconductor.

Undoubtedly, much of this interest was further stimulated by the possibility of novel physics and applications in core-shell nanowires.

New physical discovered in inversion channels and heterostructures, and the first heterostructure

electronic devices, such as modulation-doped field-effect transistors and heterojuntion bipolar transistors, are now being commercially exploited. Linear optical spectroscopic techniques, such as absorption, luminescnence and modulation spectroscopy, have for a long time been important tools in understanding the basic physics of semiconductor materials. Also over the last fifteen years or so, semiconductor optical and optioelectronic properties have become of increasing technological importance in their own right. The ever-growing application of semiconductor diode lasers and related optoelectronic technology in communications and consumer products has helped to give yet further impetus to research on semiconductor optical properties.

The successes of semiconductor optoelectronics and promising physical mechanisms and novel devices using quantum-confined structures have, furthermore, enlivened the debate over possible applications of optics for other functions such as logic and switching in communications and computation.

It is important to emphasize at the outset that quantum confinement and produce not only quantitative but also qualitative differences in physics from that in bulk structures, which is of course another major motivation for the interest in them. There are many examples of these differences. The optical absorption spectrum breaks up into a series of steps associated with the quantum-confined electron and hole levels. Excitonic effects become much stronger because of the quantum confinement, giving clear absorption resonances even at room temperature. The relative importance of direct Coulomb screening and exchange effects is quite different in quantum wells (the Coulomb screening is relatively much weaker), giving very different optical saturation behaviour.

1.2 Literature Review

Since their introduction in the 1990s, semiconductor nanowires have been extensively studied and much insight has been gained on tuning their electrical and optical properties. Nanowire related articles have shown a healthy increase in number published from 2005 to 2016, as Fig. 1.2 (blue bars) shows. Article with topics on optical properties of nanowires comprise a good portion in all the nanowire-related papers published in the recent decade, showing clear increasing trend in the number of papers on NW optics or photonics (green bars), presently comprising more than four-fifth

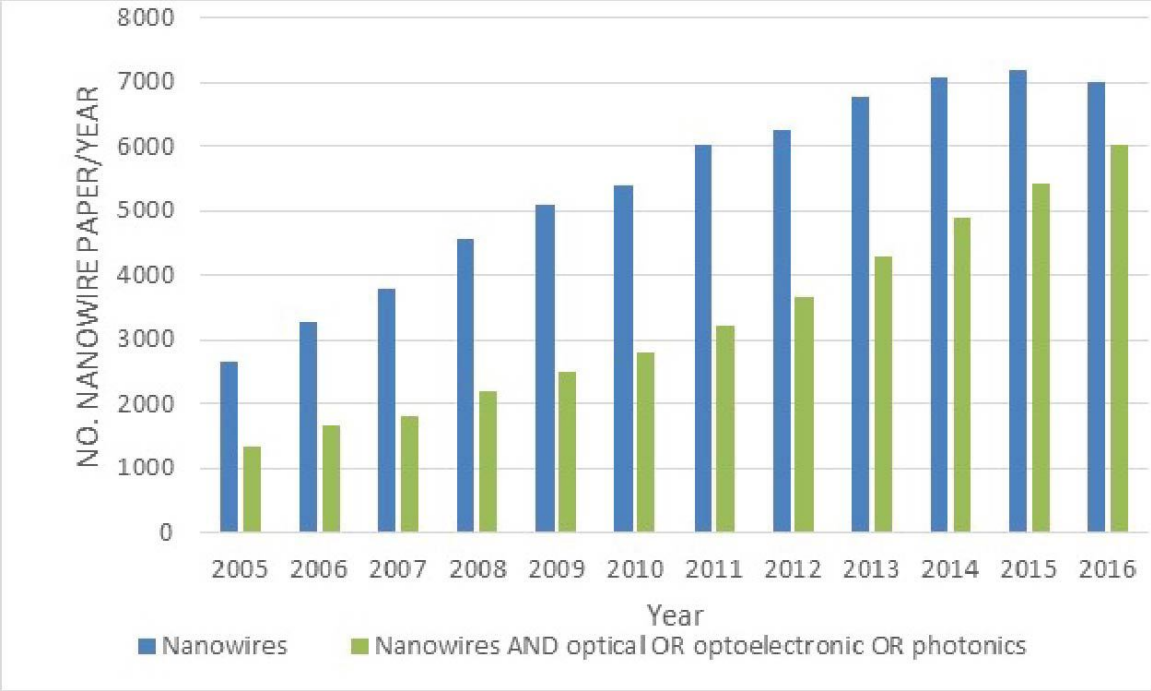

Figure 1.2 Article with topics on optical properties of nanowires consist of a large portion of all the nanowire realted papers published from 2005 to 2016. (Source: ISI website, keyword: Nanowire (blue), Nanowire AND optical OR optoelectronic OR photonics (grey))

of the nanowire-related articles.

1.3 Scope and Organization of the Dissertation

This thesis is structured as follows. The growth techniques and electro-optical properties of core-shell nanowires are presented in Chapter 2. After introducing four different light confinement mechanisms, i.e., Leaky Mode Resonance, Whispering Gallery Modes, Fabry-Perot Resonant Mode and Helical Resonance Modes, Chapter 3 presents our findings for a generalized volumetric modes with light management of sub-wavelength cavities. Chapter 4 presents our methods and findings for calculating band-bending and electronic distribution in both cylindrical and hexagonal core-shell nanowire by solving Poisson-Schrodinger equations self-consistantly. In Chapter 5, we apply the inter-band optical transition rates study to understand the extremely enhanced optical properties of hexagonal core-shell nanowires. and rule out three primary factors (overlap integral, oscillator strength and

joint optical density of states) which are strong function of dimensionality. The quantum machenical derivation based on perturabtion theory and Fermi's Golden Rule used in this chapter are outlined in more detail in Appendix A. The modeling of lasing threshold based on the optical transition rates in Chapter 6 confirmed that our theoretical explanation, analysis and calculation of optical properties of core-shell nanowire have a very strong dependence on electron confimentent. Finally, we present our conclusions in Chapter 7.

Throughout this work we use the term *nanowires* (NWs) to represent a specific quantum confined structure with cross-sections of 2-300 nm and lengths upwards of several micrometers. There are other research groups using terms such as *nanopillars*, *nanotubes* or *quantum well wires* (QWRs) to discuss the same nanostructures.

CHAPTER 2

OPTICAL ENHANCEMENT OF CORE-SHELL NANOWIRE

Given that the profound enhancement of optoeletronic properties of nanowires is the major theme of this dissertation, it is dutiful to first summarize the major experimental results, such as fabrication and characteristics of core-shell nanowires (CSNWs).

Electron systems in lower dimensions are adequately treated through perturbation methods. For 1D electron systems (1DES) the correlations among electrons are much more significant due to higher degrees of confinement. The electron can either be moving to the left or right and any small or localized interaction can cause a collective response from the whole system. This is the condition of broken symmetry, in which the overall status of the system has to be reformulated. For a 2DES, a broken symmetry occurs at very low densities of fermions, in which formation of a Wigner lattice is expected, which is due to the Coulombic interactions of electrons. Interestingly for a 1DES, the direction of movement for fermions is restricted to the left or right. Consequently, the density of the system becomes irrelevant with respect to the determination of the status of the system. Such a 1D many electron system is often called a *Lüfinger* Liquid, as he was the first person who successfully formulated these systems.

Importantly, a 1DES can experimentally be realized in various material systems. These include carbon nanotubes, electrons at the edges of a 2DES, and in nanowires.

A core-shell nanowire (CSNW) is a quasi-one dimensional structure with a wide band gap materials, such as AlGaAs, wrapping around a low band gap semiconductor, such as GaAs.

It is expected that the lower dimensionality in CSNW to have a significant influence on both optical and electrical properties of the structure. Fot instantce,

Electrically it is important account for the electron correlations in order to determine the behavior of the structure. The significant values of exchange and correlation energies in 1DES, makes them an interesting candidate for probing their energy dynamics. This, however, imposes various experimental challenges and theoretical considerations and are deferred to future investigations.

2.1 Growth of Nanowires

Freestanding quasi-one-dimensional semiconductor nanostructures (nanowires) based on III-V compound semiconductors, owing to their unique physical properties, are considered ideal building blocks for the realization of photonic and electronic nanodevices.

Currently, two bottom-up approaches to the fabrication of freestanding nanowires are considered: (i) selective area epitaxy (SAE)[26] and (ii) metal-catalyst assisted grouth through the so-called vapor-liquid-solid (VLS) mechanism[27,28]. The latter method relies on the alloying of a metal catalyst (usually Au) nanoparticle with the semiconductor constituent elements, supplied through a vapor phase. The as-formed alloy acts as an initial nucleation site for the material and further guides the nanowire growth, the diameter of the nanowire being controlled by that of the metal nanoparticle.

An advantage of the VLS method over SAE is that it does not require nanolithograpic processing of the substrate; furthermore, it is compatible with most advanced epitaxial grouth techniques for III-V compounds, such as molecular beam epitaxy, chemical beam epitaxy, and metalorganic vapor phase epitaxy (MOVPE).

GaAs nanowires were grown by low (50mbar) pressure MOVPE using an Aixtron reactor model AIX200 RD. TMGa and TBAs were used as gallium and arsenic precursors, respectively. Au nanoparticle deposited on $(\bar{1}\bar{1}\bar{1})B$ GaAs were used to catalyze the nanowire growth. To this purpose, VGF-grown semi-insulating (undoped) GaAs wafers oriented $(\bar{1}\bar{1}\bar{1})B$ were used. The substrates were then first degreased in isopropanol vapors, etched in $4H_2SO_4 : 1H_2O_2 : 2H_2O$ solution for 8 min at

around 40 °c, ringsed in de-ionized water and finally dried under pure N_2. Au nanoparticles with $\sim 60nm$ diameters were prepared by reaction of $HAuCl_4$ with sodium citrate in aqueous solution and randomly deposited on the as-prepared GaAs surface by dropping a small amount of colloidal solution onto the substrate. The solvent (water) was then evaporated by holding the samples on a hot plate (in air) or a few minutes; Au nanoparticle surface densities thus achieved ranged around (1-4).

After loading the sample into the reactor chamber, its temperature was raised, and sample annealing was then performed for 10 min to absorb GaAs surface oxides and organic residues originating from the Au nanoparticle synthesis. This annealing step would also allow the initial uptake of Ga atoms from the GaAs substrate into the Au nanoparticles.

2.2 Scanning Electron Microscopy Images

Figure 2.1 is top view scanning electron microscopy (SEM) image of nanowires of with $\sim 100nm$ diameter core of GaAs, and $\sim 40nm$ thick AlGaAs, with the four figures showing at different magnifications and view angles. These images demonstrate the rather sparse distribution of the wires. In addition, the wires are not fully arrayed with various growth directions and lengths. The most magnified view for the left bottom figure clearly indicate the CSNWs have hexagonal structure and tapering effect along the wire growth direction.

2.3 Electrical Characterization of Nanowire

The as-grown CSNWs are used to perform optical characterization measurement. However, in order to measure the CSNWs electrical performance, additional treatments have been taken to make Ohmic contacts between nanowires and transmission lines.

Characteristic current-voltage (I-V) curves of the nanowire device are given in Fig. **??**. The I-V curve exhibits rectifying behavior, confirming that the device is a well=behaved diode structure with the electric contact on one side (Al) ohmic and the other (Pt) Schottky. The reverse bias dark current of the device is very small, $\sim 20pA$ at -1V, and could be further improved by properly passivating

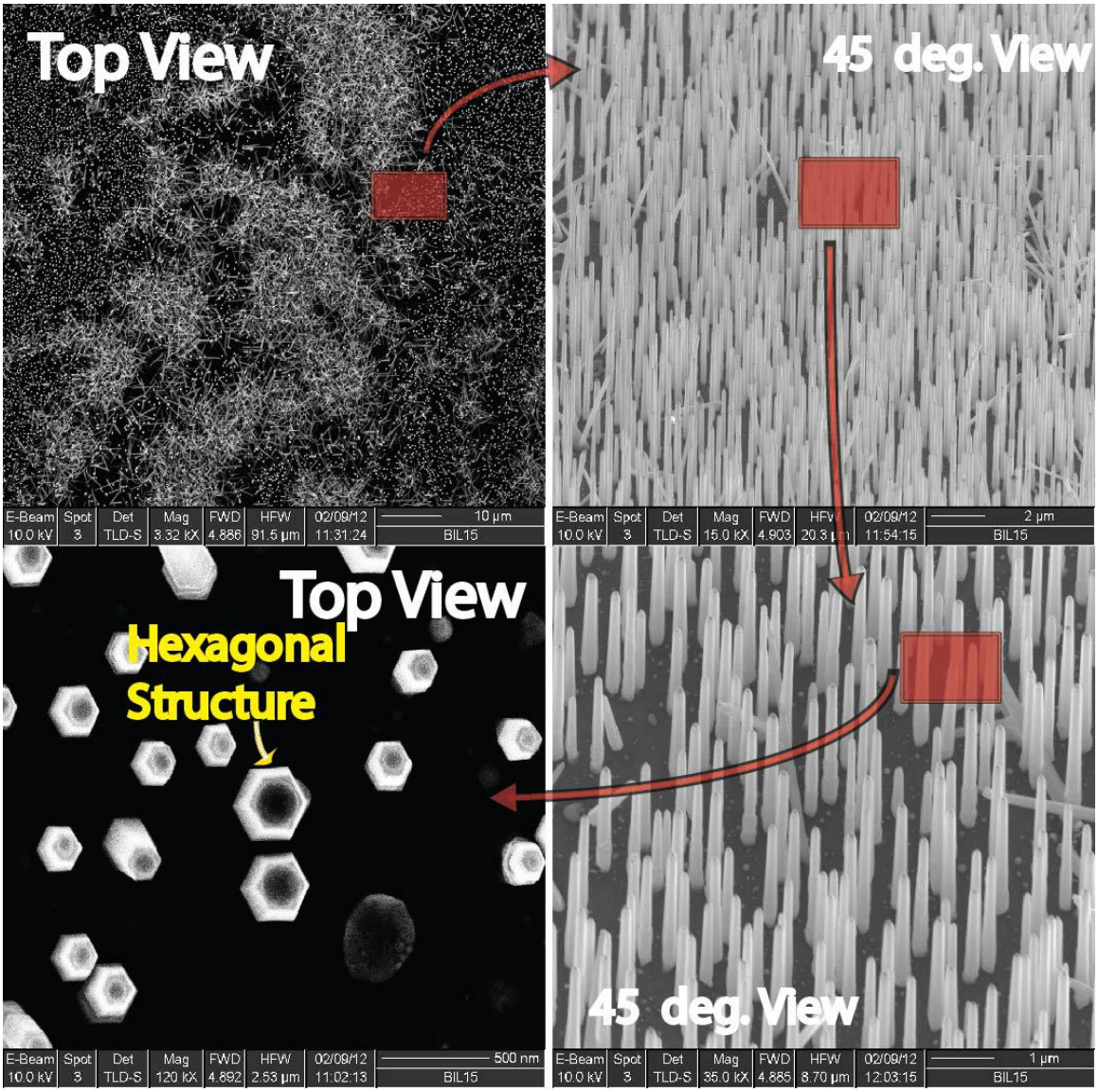

Figure 2.1 Scanning Electron Microscopy image of as-grown GaAs/AlGaAs core-shell nanowires on Si taken at different magnifications and view angles (Image courtesy of Dr.Pouya Dianat)

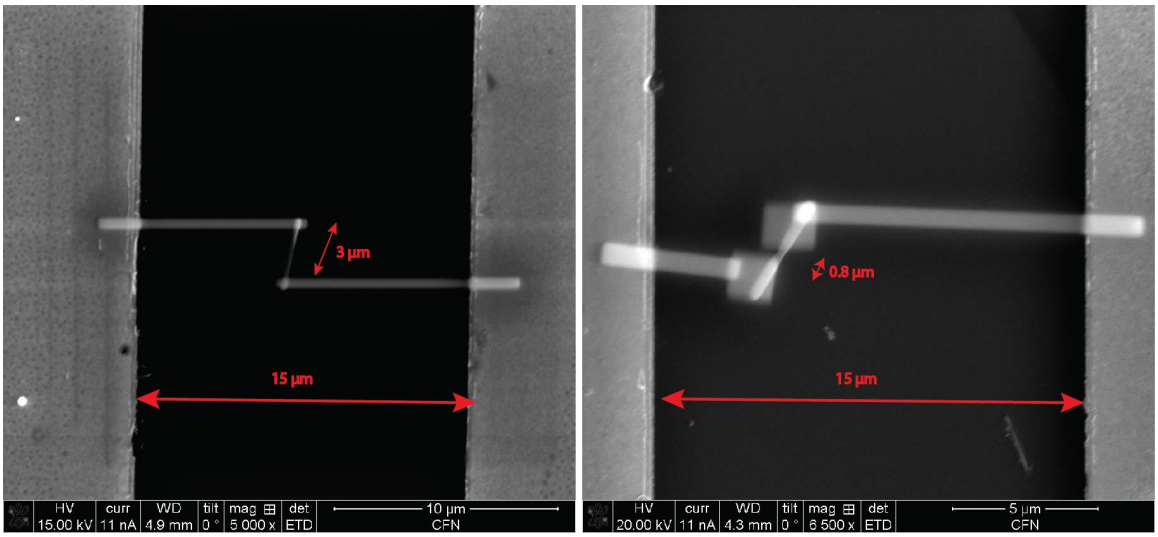

Figure 2.2 Scanning Electron Microscopy (SEM) image of one dispersed core-shell nanowire connecting with the transmission line by Focus Ion Beam (FIB).

the CSNW surface. Upon illumination, the device shows a prnounced photovoltaic response due to the built-in potential from the Schottky junction. The short length of the nanowire device and the large depleted region by the built-in potential enable the nanowire photodetector to be operated at zero bias. Fig. **??** shows the photocurrent of the device at zero bias as a function of irradiance. The linearity of the device was demonstrated up to at least at a 632 nm wavelength. The excellent linear response is in part based on the good crystalline quality of the nanowires, as confirmed by transmission electron microscopy. In addition, the capactiance of a typical device () is calculated to be 5 aF based on a simple parallel-plate model and thus its cutoff frequency is mainly limited by the transit time of the photo-generated charge carriers in the device, which may in principle reach 100 GHz after certain parameter opti

2.4 Absorption Enhancement

Figure 2.5 shows the reflectivity of a GaAs wafer on which 50 nm thin film of AlGaAs is grown, and compared this to the reflectivity spectrum of a Si substrate. As expected, about 30% to 55% of a normally incident light is reflected in bulk Si and GaAs, with a sharp change for wavelengths near

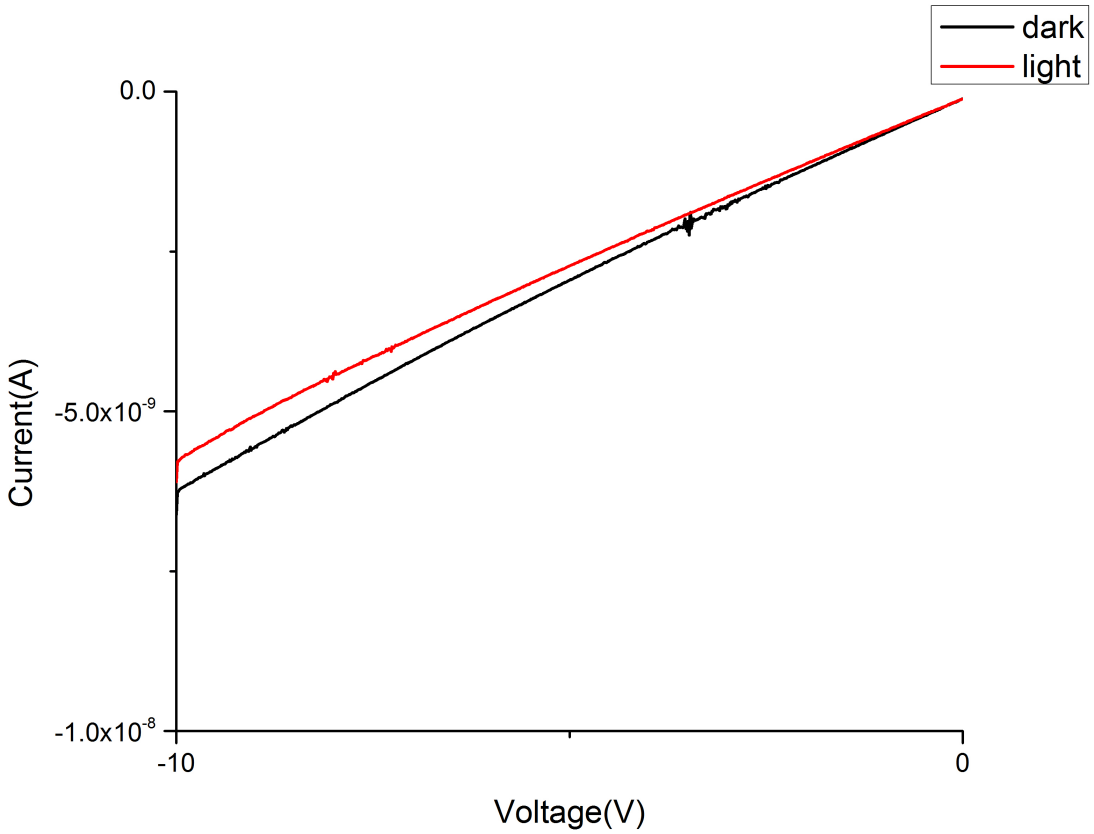

Figure 2.3 Current versus Voltage Measurement under illumination of Single Core-Shell Nanowire.

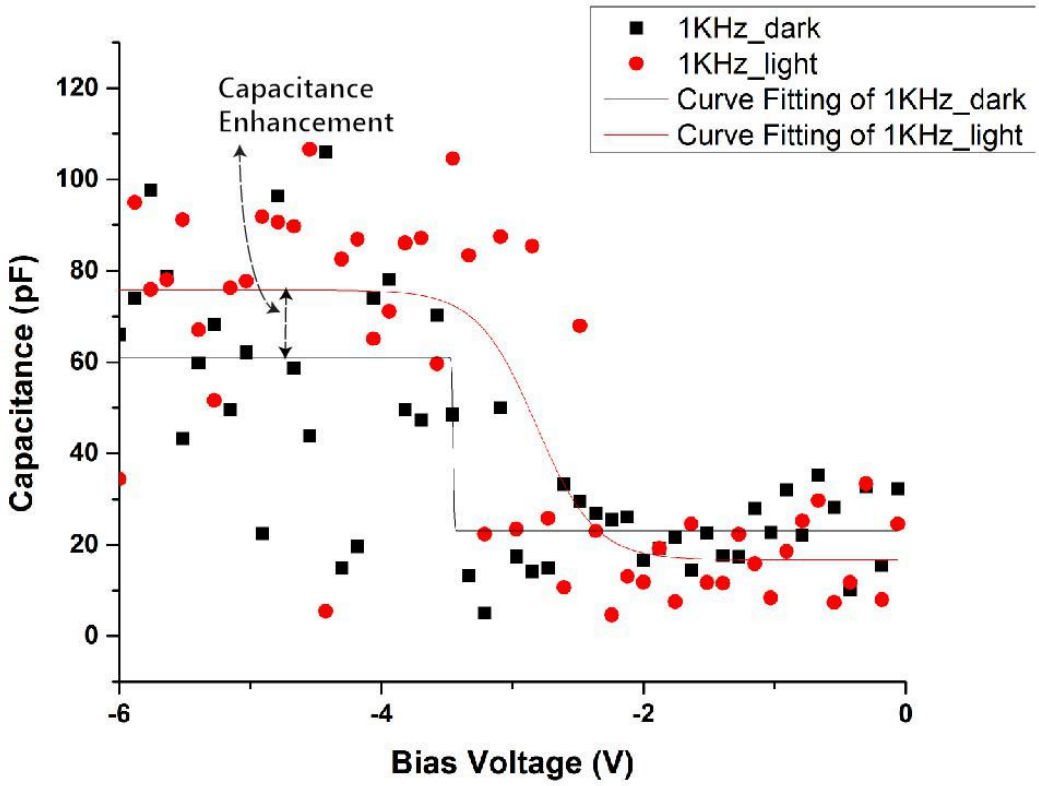

Figure 2.4 Capacitance versus Voltage Measurement under illumination of Single Core-Shell Nanowire.

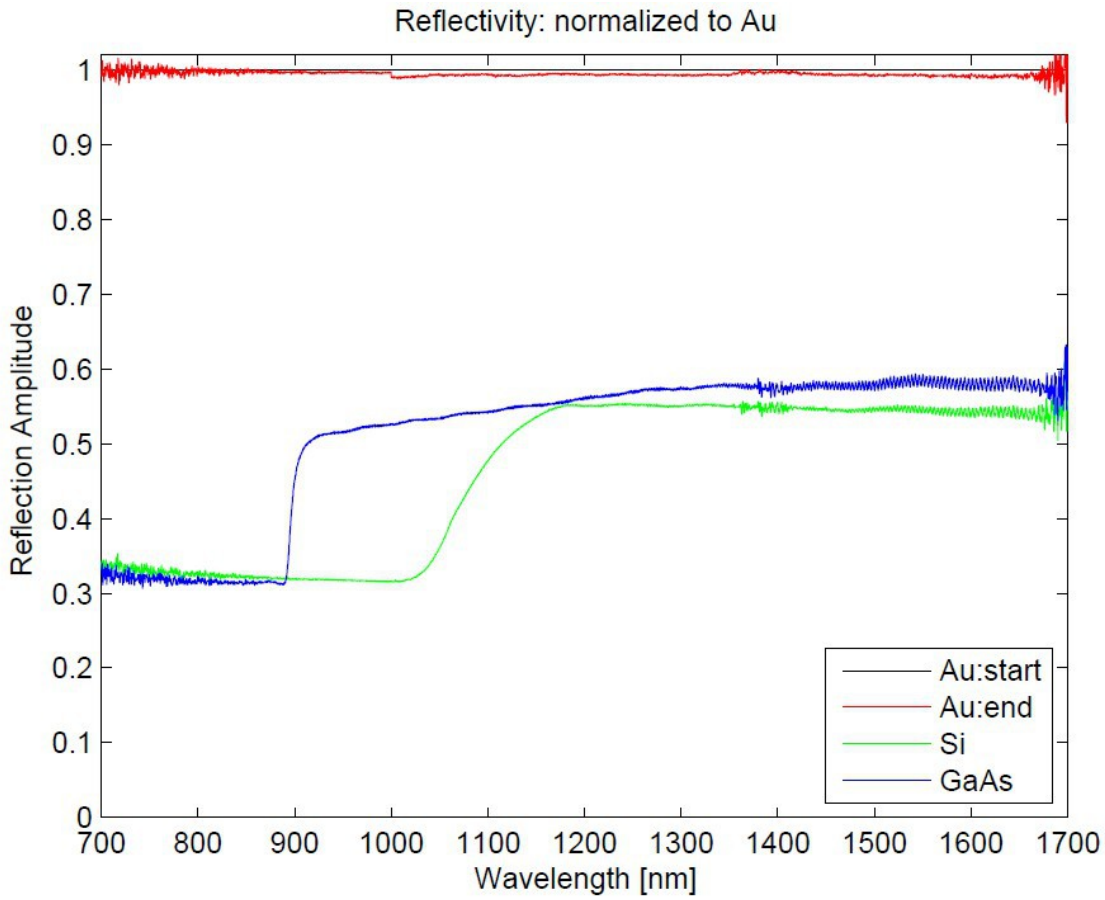

Figure 2.5 Reflectivity of GaAs (blue) and Si (green) substrates measured with $\sim \mu m$ normally incident beam.

their respective band gaps. All the data are normalized to the reflectivity of gold (Au).

Figure 2.6 contrasts this with the measured absorption spectrum of two types of GaAs core, AlGaAs shell nanowires (CSNWs): those grown on a GaAs substrate (black), and the others heteroexpitaxially grown on a Si substrate (red). The spectra show that both cases have the signature change of reflectivity at badgap of GaAs, i.e., these are due to the GaAs/AlGaAs CSNWs, not the substrate. Importantly, for the wavelength range of 700-1200nm these core-shells which only occupy 15% of the volume compared to thin films of the same height, reflect 2-4% of light for the CSNWs grown on Si, and 3-7% of light for those grown on GaAs substrate. The beam-width of the incident light being $\sim 1\mu m$, this shows that only a few NWs are interrogated by ligth and, normalized to volume,

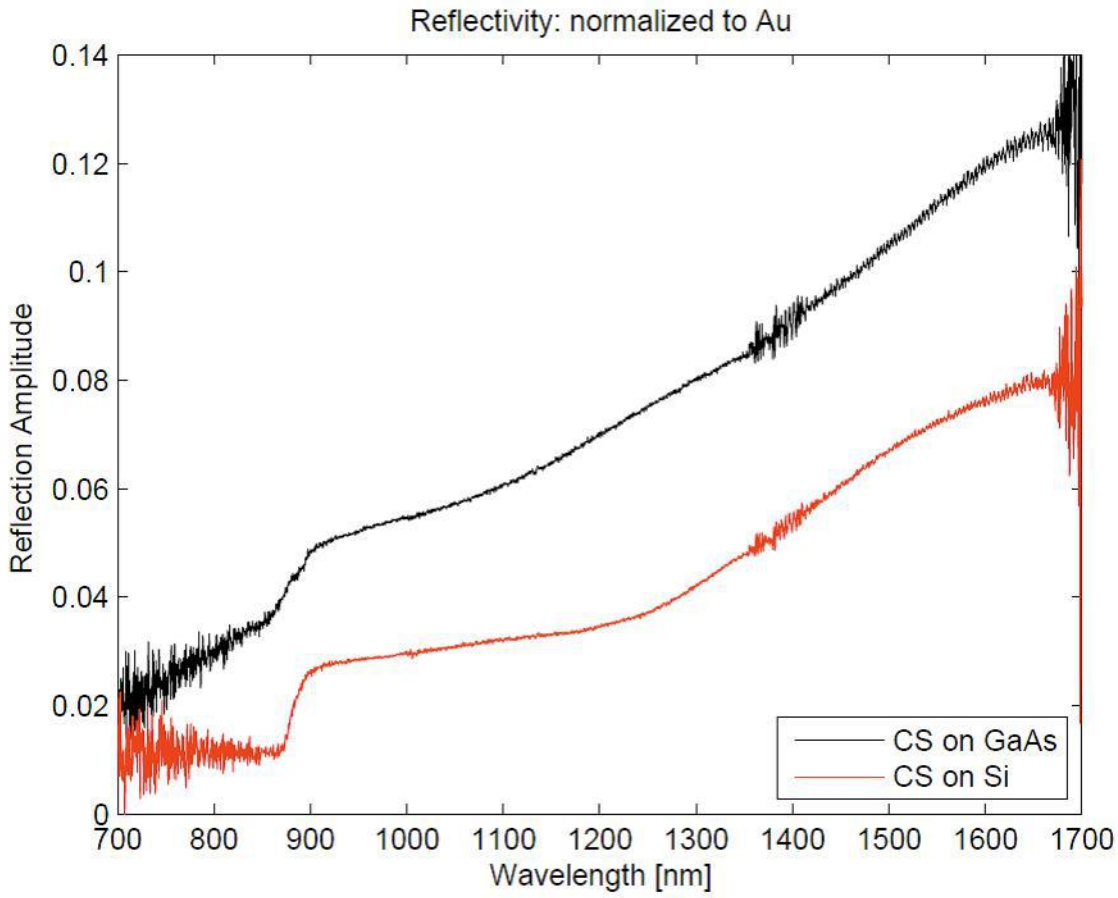

Figure 2.6 Reflectivity spectrum of GaAs/AlGaAs core-shells grown on Si (red) and GaAs (black) substrates shows, normalized to volume, nearly two orders of magnitude more absorption of ligth.

these wires absorb more than two orders of magnitude more ligth than their thin-film counterparts.

2.5 Emission Enhancement

Figure 2.7 compares room temperature micro photoluminescence (PL) spectrum of bulk GaAs to CSNWs grown on GaAs, and two cuts of Si. The ratio of peak luminescence of a) CSNWs on GaAs, B) CSNWs on Si[111] and c) Si(miscut) substrates to bulk GaAs are, respectively, 923, 311 and 10. Considering the beam width of $\sim 1\mu m$, 5-10 NW were excited, yet emitted over three order of magnitude more light compared to bulk.

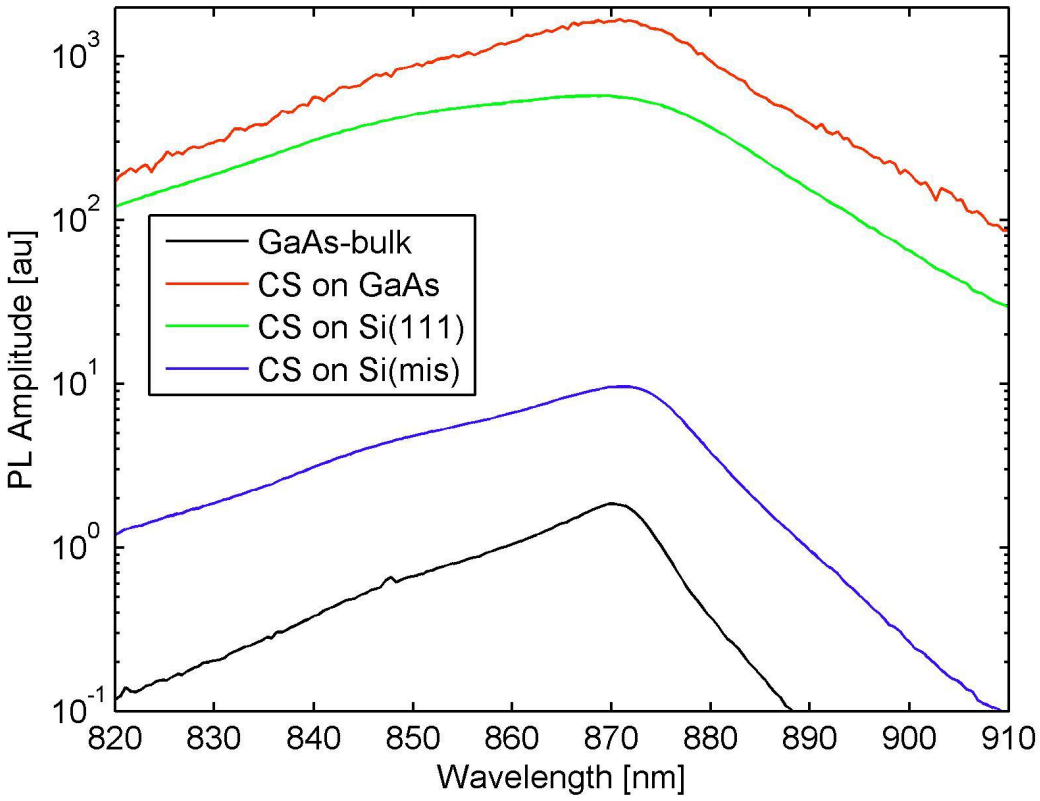

Figure 2.7 Photoluminescence of bulk GaAs, Core-Shell Nanowires grown on GaAs and Si.

2.6 Lasing

Photoluminescence (PL) of bulk GaAs to CSNWs grown on GaAs, and on two directions of Si showed that normalized to the fraction of the volume that these wires occupy, nearly 10,000 times more brightness is observed in these wires compared to thin-film as in Fig. 2.7. In the case of stimulated emission of light, the photon mode density $(1 + u_\varepsilon)$ plays a crucial role. Figure 2.8 is the photoluminescence (PL) spectrum at various optical pump intensities. As the excitation laser power increase beyond $5\mu W$ a sudden and highly nonlinear increase in the emission intensity is observed, with pronounced peaks emerging from 800nm to 850nm that rapidly grows to become several orders of magnitude stronger than the background emission. The lasing amplitude versus excitation power demonstrates a threshold of around $5\mu W$, followed by saturation near $12\mu W$. This nonlinear threshold behavior shows in detail in the L-L plot, (i.e., The pumping power intensity (L) versus output light power intensity (L)) as in Fig. 2.9. The sharp peak has a full width half maximum (FWHM) that varies from 1.5 to 3.5 nm. This remarkable behavior is achieved in the as-grown wires with no vertical structure.

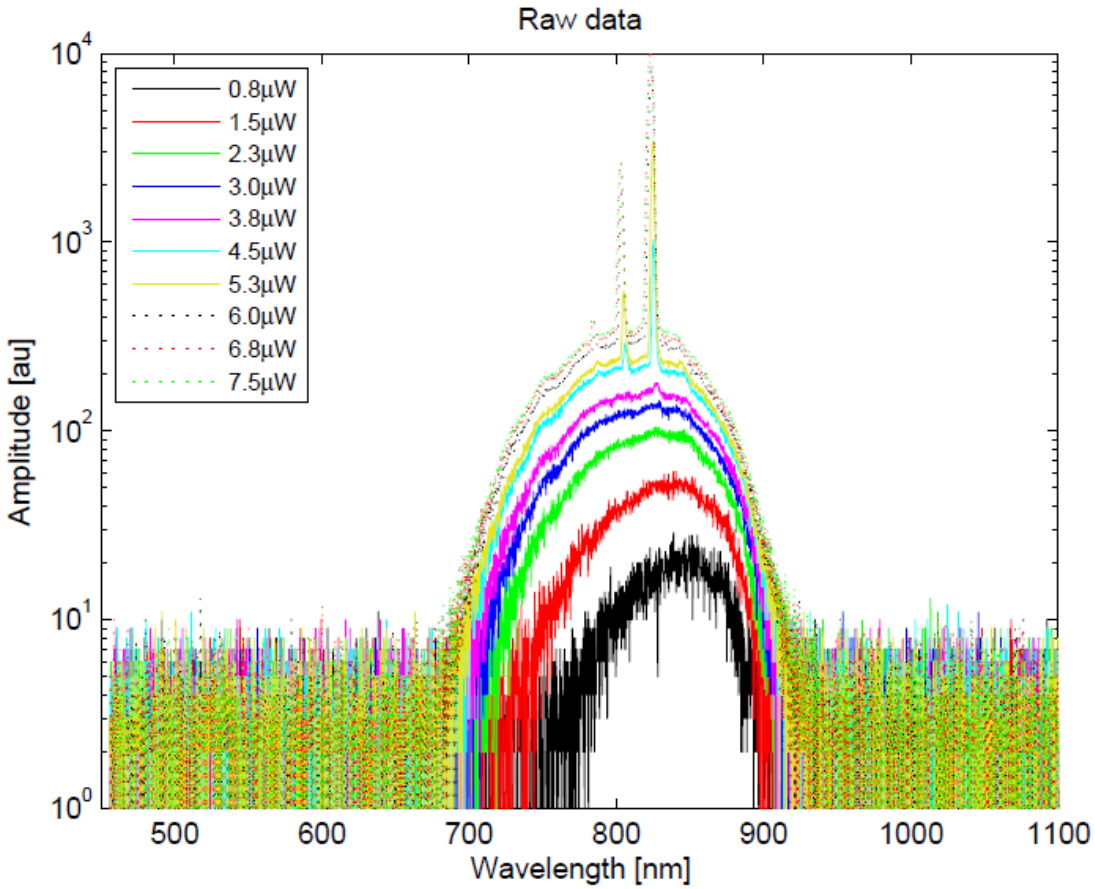

Figure 2.8 Micro-Photoluminescence measurements with fs-pulsed, 532-nm laser excitation at 250kHz repetition rate shows lasing of the as-grown wires.

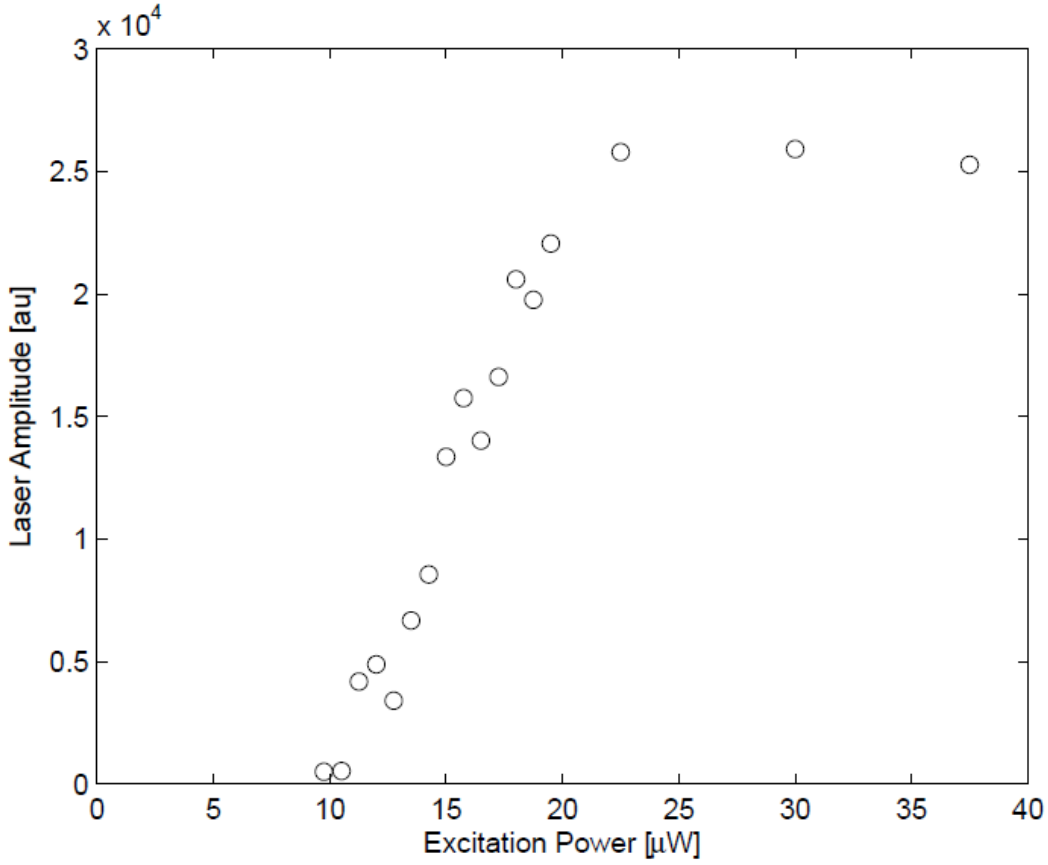

Figure 2.9 *L-L curve of as-grown core-shell nanowire. The pumping power intensity (L) versus output light power intensity (L) of as-grown core-shell nanowire operating at room temperature with a low threshold of* $\sim 10\mu W$ *and followed by saturation near* $22\mu W$.

CHAPTER 3

LIGHT CONFINEMENT IN SUB-WAVELENGTH NANO-STRUCTURE

3.1 Light and Nanowire

3.1.1 Leaky Mode Resonance

Interaction of light with a dielectric or metallic cylindrical medium is analyzed by solving Maxwell's equations with the appropriate boundary conditions in the classical waveguide theory [80] which leads to highly confined modes in optical fibers and microscale dielectric resonators. In an infinitely long cylinder, even at deep sub-wavelength diameters this results in a characteristic equation the solution to which are the transverse magnetic (TM) and transverse electric (TE) resonant modes. We can define the electromagnetic modes of localized resonators as time-harmonic solutions of the form to the source-free Maxwell equations. This solution shows that the longitudinal field component distributes outside the NW, and is in resonance with the natural modes, such as TE11, TM02, etc., supported by the NW. These modes have been termed leaky-mode resonances (LMR) [81, 82], and provide an intuitive tool to facilitate the understanding and optimization of the resonance effect in such nano-structures. We replicate these results using MEEP, a widely used open-source finite-difference time-domain (FDTD) simulation package [83], to identify how light is confined in an infinitely long GaAs nanowire. The top row of Fig. 1 shows several configurations of TM LMR modes for a NW with diameter of 220nm, with excitation single wavelength light being incident parallel to the NW axis. The blue and red color codes represent the polarization of the electric fields. The TE modes are primarily identical to the TM modes shown here with the electric and magnetic fields

exchanged. If the light is incident with an arbitrary angle, then so-called hybrid HE and EH leaky modes will be excited instead of the pure TE or TM mode. The bottom row of Fig. 1 shows the directional energy flux density of the electromagnetic field, the Poynting vector, at different time frames with light being incident perpendicular to the NW axis from the right side. The light is seen to propagate from the right and then mostly remain confined at the left part of the cylinder. It is notable that in either case the light energy is spatially distributed along the cross section of the wire but, as expected from a 2D treatment does not vary axially. Figure 1 demonstrates that the LMR can gently confine light within subwavelength semiconductor nano-structures, similar to the intuitive ray-optics picture of multiple total internal reflections from the periphery of the cylinder. As shown by in Ref. [81], these LMRs depend on the radius and the height of the dielectric, which allows light engineering of the nanowires so as to increase its absorption efficiency at pre-determined wavelength, e.g., to maximize absorption of sunlight spectrum for higher efficiency solar cells, or to radiate as optical antennas.

3.1.2 Whispering Gallery Modes

Infinitely long cylindrical or hexagonal NW structures can also support Whispering Gallery (WG) modes [78, 79, 84-90]. To calculate the resonant WGMs, Maxwells equations have to be solved numerically [91] taking into consideration the spectral dependence of the material of interests index of refraction. However, we can deduce a simple plane-wave model from theoretical derivations, and the relationship between resonance wavelength and the corresponding mode serial number N can be obtained [92]. The WG modes can also reflect and confine light in the (subwavelength) nanostructure by total internal reflection from the curvature of the structure boundaries. However, a light wave can interfere with itself only when having completed one full circulation within the resonator, which means only the light with one or multiple wavelengths are allowed to perform multiple circulations generating a standing wave. Figure 2 from reference 85 shows near-field intensity patterns of low-order TM polarized hexagonal WGMs for n=1 and refractive index =2.1. Each mode pattern is labeled by its respective mode number m (lower right number) and its symmetry class (upper right

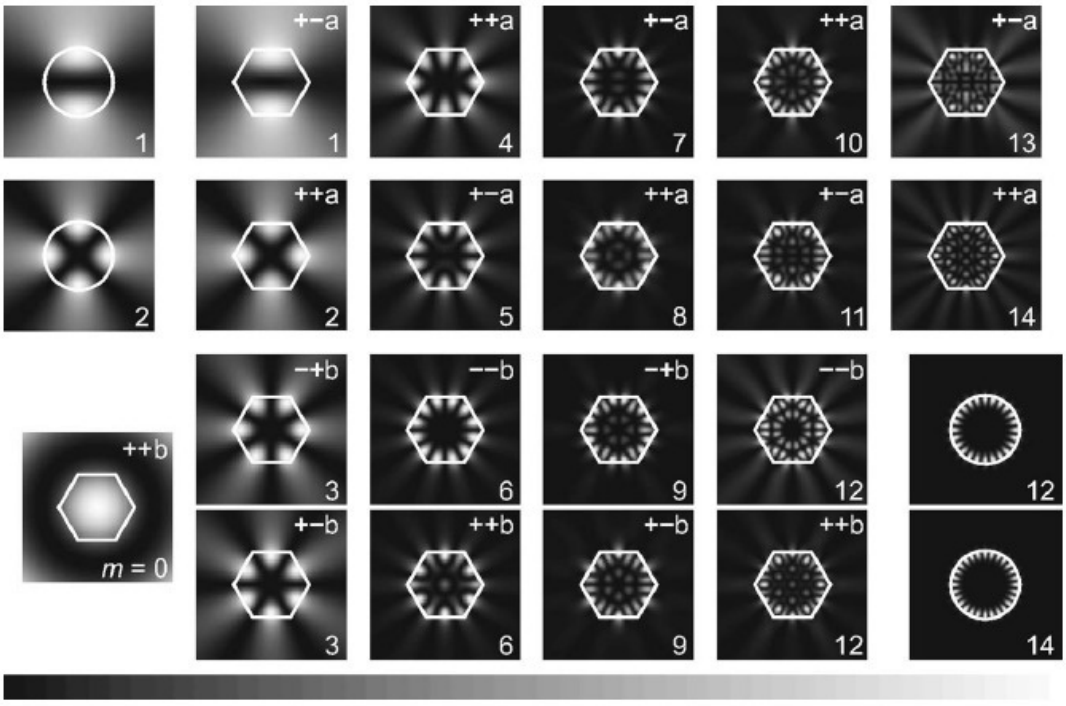

Figure 3.1 Several configurations of Whispering Gallery resonance modes in infinite long cylindrical and hexagonal nanowire. For comparison, four mode patterns of the circular cavity are given in the upper and lower right together with their angular mode number. (Reprinted with permission from [1] , ©2005 by the American Physical Society.)

symbol). For comparison, four mode patterns of the circular cavity are given in the upper left and lower right together with their angular mode number. We again observe the radial spatial dependence of light intensity. Furthermore, the low order WG modes of hexagonal NWs are essentially similar to the cylindrical ones, but for higher order modes additional features will arise on the facets of the hexagonal NWs [85]. Simulation results also show little difference between WG mode and Leaky modes in lower order modes for both hexagonal and cylindrical structures. As with the LMR, the resonant WG modes have been used as the basis for a precise theoretical explanation of the enhanced optical behavior of hexagonal NWs, such as enhanced light absorption [81, 93-96] and emission [78, 97-99]. Furthermore, these numerical solutions have lead to reproduction of experimental resonance spectra, e.g., polarization-resolved micro-photoluminescence (-PL) and cathodeluminescence (CL) spectroscopy.

3.1.3 Fabry-Pérot Resonant Mode

The above analysis and results apply to long structures, hence, provide two-dimensional radial modes, independent of the NW axis. However, light confinement has strong axial dependence, necessitating three-dimensional analysis of the cavity modes. FDTD simulation in 3D are used to identify the axial dependence of resonant modes in these nano-structures, revealing modes which are volumetric in nature. Fabry-Perot (FP) modes have been analyzed for sub-microcavity, or nano-cavity, NWs with cylindrical or hexagonal structures, specifically in order to determine the axial dependence of the resonance modes [29]. At least two mirrors are needed to construct the reflection structure inside the cavity, whether they are the top and bottom ends, i.e., the air and substrate interfaces with the nanowire, or any of the two opposite facets along the nanowire axis. For subwavelength structures, the longitudinal WG modes have high scattering losses due to diffraction, and axial FP waveguide modes will dominate[30]. However, due to small difference of the refractive index between the substrate and the nanowire dielectric, the existence of the FP mode will only be valid if the nanowire has relatively large radii, e.g., larger than 200 nm[31]. Under these conditions, besides the top and bottom ends, the lateral facets of nanowire can also be treated as two parallel slabs, and with the dielectric in between, it can support the FP mode with mode spacing inversely related to the nanowire length. An application of this analysis is in the design of NW lasers, since the optical cavity modes are observed at threshold for lasing, and have been investigated for both optical and electrical pumped cases [32,33]. As a results the FP resonance mode based nanoscale lasers are not only capable of covering a wide spectral regions, but can also can be integrated as single or multi-color laser source arrays in silicon based photonic integrated circuit or microelectronic devices [32,33]. However, the FP modes supported by the nano-cavity structure have relatively small quality factor due to the small difference of the refractive indices of the substrate and the NWs. In order to address this issue, Bragg gratings can be produced at the NW ends, alternatively, NWs can be placed on metal substrates in order to increase the FP resonance peak intensity by more than one order of magnitude compared to those on Si substrates[34].

3.1.4 Helical Resonance Modes

Nano needles of III-V material grown on heterogeneous substrates are optoelectronic devices which have shown interesting optical behavior, including lasing, at room temperature[2]. Figure 3 (A) shows SEM image of a nano-laser grown on silicon substrate that has subwavelength dimensions on all sides. Analysis of light propagation introduced by shows that unlike the traditional WG mode that lack vertical structure, there is net propagation in axial direction in these structures which leads to volumetric resonant modes which are termed helical mode resonances[2]. The schematic Fig. 3(B) suggests a helical ray path with nearly total internal reflection at the nanopillar-silicon interface due to the glancing angle of incidence from the hexagonal facets of the nano-laser shown in Fig. 3(A). As such, the faceted shape of the structure affects the optical cavity properties. FDTD-simulated field profile shows a hexagonal WG-like mode pattern in the transverseplane as in Fig. 3 (C), which arises from strong azimuthal components of helical modes. Figure 3 (D) shows first-order and higher-order standing waves axial variation. The radial mode number (first number, m) describes the transverse field pattern for WG modes, and the axial mode number (second number, n) describes the axial standing wave as is the case for Fabry-Perot resonances. It is seen that light or optical field can be well confined in the nanostructure even with low index contrast at the dielectric interface thus producing the nano-resonators needed for lasing. Although the quality (Q) factors of such nanostructure are usually not large, these helically propagating cavity modes, provide an optical feedback mechanism without the sophisticated mirror structures of the vertical cavity surface emitting lasers (VCSELs). Additionally, since the nanowires are heteroepitaxially grown on different substrates, they enable heterogeneous integration of photonic emitters and silicon based computational circuitry. Whereas traditional FP modes are inhibited by the interface between semiconductor nanostructure and the silicon substrate, such unique optical structures have been proposed as an avenue for engineering and integrating on-chip nanophotonic devices.

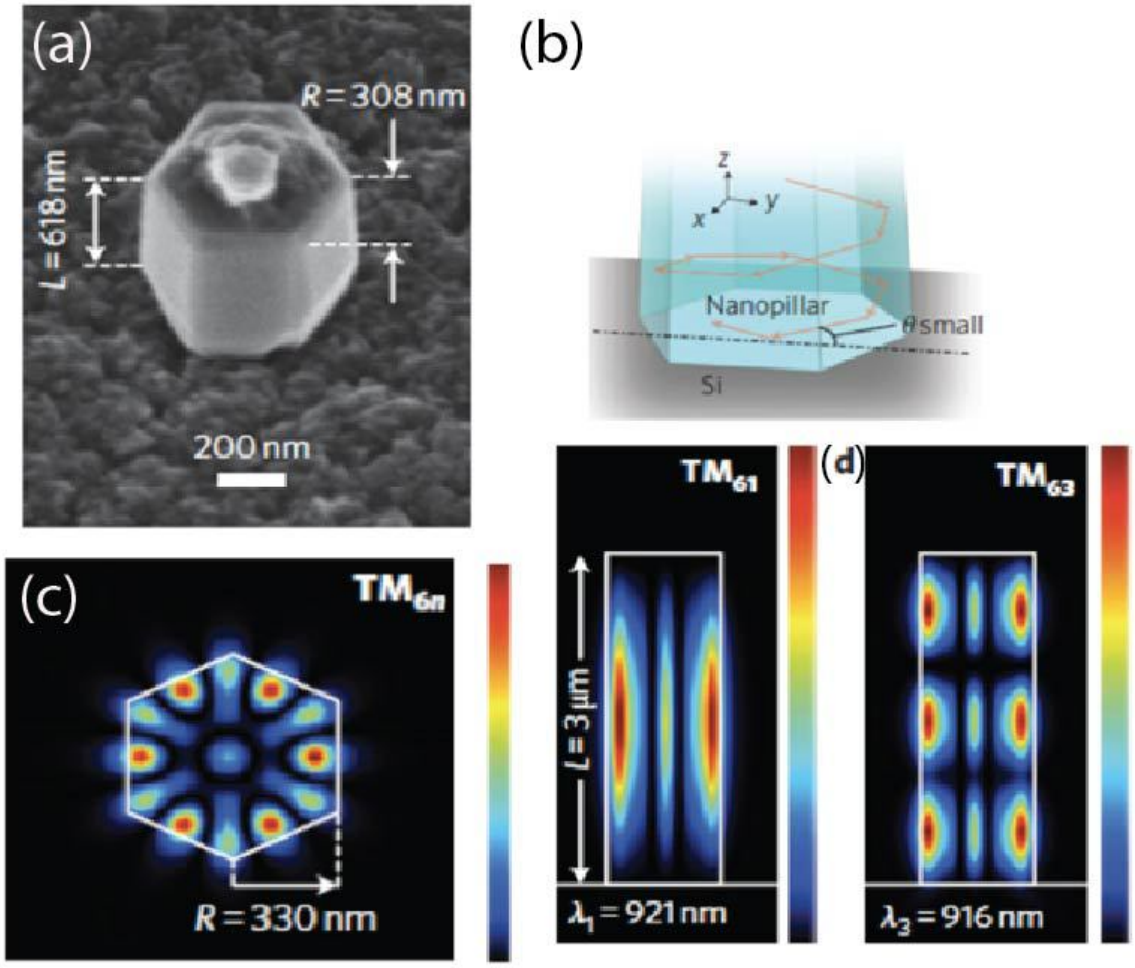

Figure 3.2 Helically propagating modes for optical feedback. (a) SEM image of the nanolaser grown on silicon substrate. (b) Schematic depicting a helical ray path because of glancing angle of incidence from the hexagonal facetes of the nanolaser shown in (a). (c) FDTD-simulated field profile shows a hexagonal WG-like mode pattern in the transverse plane, which arises from strong azimuthal components of helical resonance modes. (d) First-order and higher-order standing waves' axial variation. (Reprinted with permission from Macmillan Publishers Ltd: Nature Photonics [2], ©2011)

3.2 Volumetric Modes

The diameter of the nanostructures which can support the helical resonance modes is near the Rayleigh limit, around the boundary of the validity of ray-optics. FDTD analysis can be applied to deeper subwavelength structure in order to identify the cavity modes which are by nature volumetric, i.e., axially dependent. Figure 4 shows simulation results for various diameters of hexagonal structure of 1 m length. Incident radiation with 532 nm wavelength is nearly parallel to the wire axis and different modes are displayed for different radii. Top row shows radial spatial dependence at the middle of the wire axis, and the bottom row shows the axial dependence. Top row results are similar to Figures 1-2, and the bottom row shows that the light can be confined in volumetric resonance mode in both transverse plane and longitudinal plane even with sub-wavelength diameter of these hexagonal NWs. Unlike helical modes, the explanation of resonance need not rely on an intuitive ray-optics description based on the grazing angle of incident light, but shows similar results in how the deep subwavelength structures can confine the light and produce a resonant cavity without having sophisticated mirrors at the end facets. In this respect nano-cavities of as-grown nanowires outperform microcavities of VCSELs.

has been[35]

3.2.1 Nanocavity Geometry Dependence

3.2.2 Light Engineering of sub-wavelength Nano-structure

Dependence of the resonant modes on the cavity geometry offers an important degree of freedom to engineer a cavity for particular optical properties. Figure 6 shows the dependence of three volumetric TM resonant modes excitation wavelengths with radius. In this spectral range, only lower TM modes can be excited with smaller radii, e.g., r = 40 nm and 60 nm, however, as the radius increases, higher order modes can be excited, and the optical power corresponding to the lower order modes will be reduced. We observe redshift of these volumetric TM modes with increasing NW radius. Also, the wavelength variation of TM1n mode is much larger compared to TM2n and TM3n modes. These

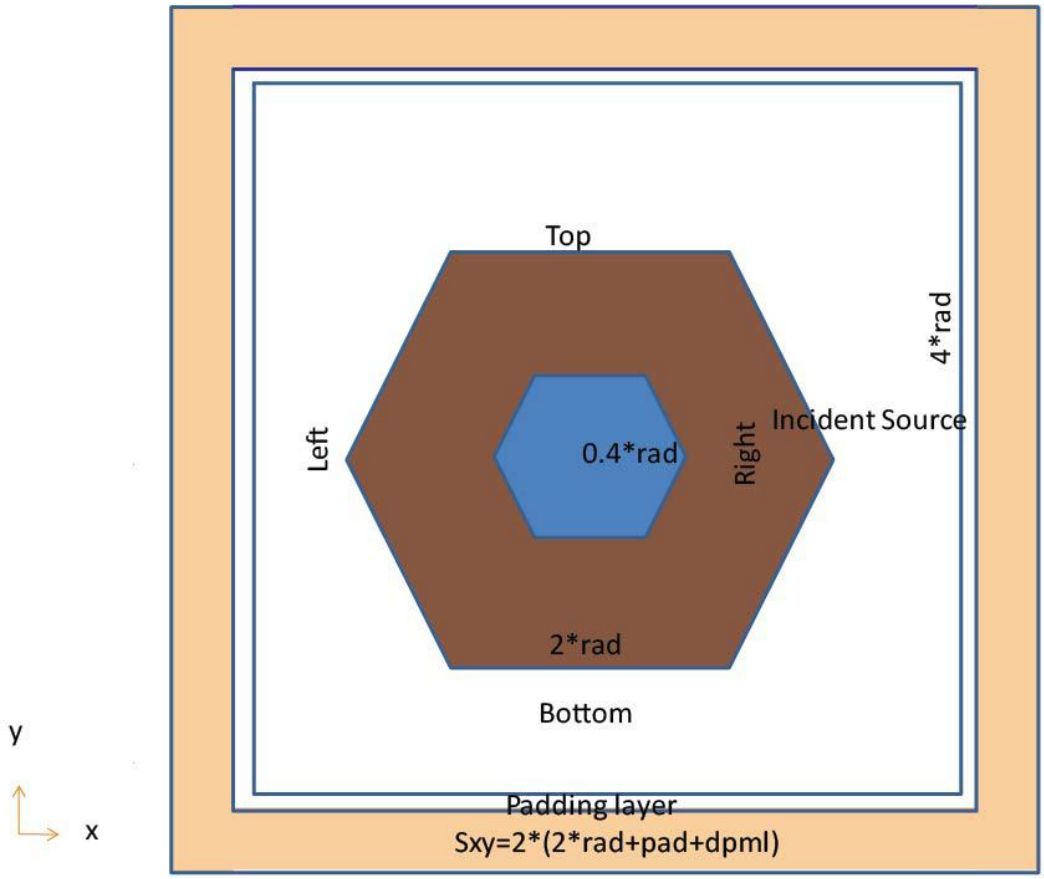

Figure 3.3 A schematic illustration of Finite-Difference-Time-Domain (FDTD) Simulation Set Up

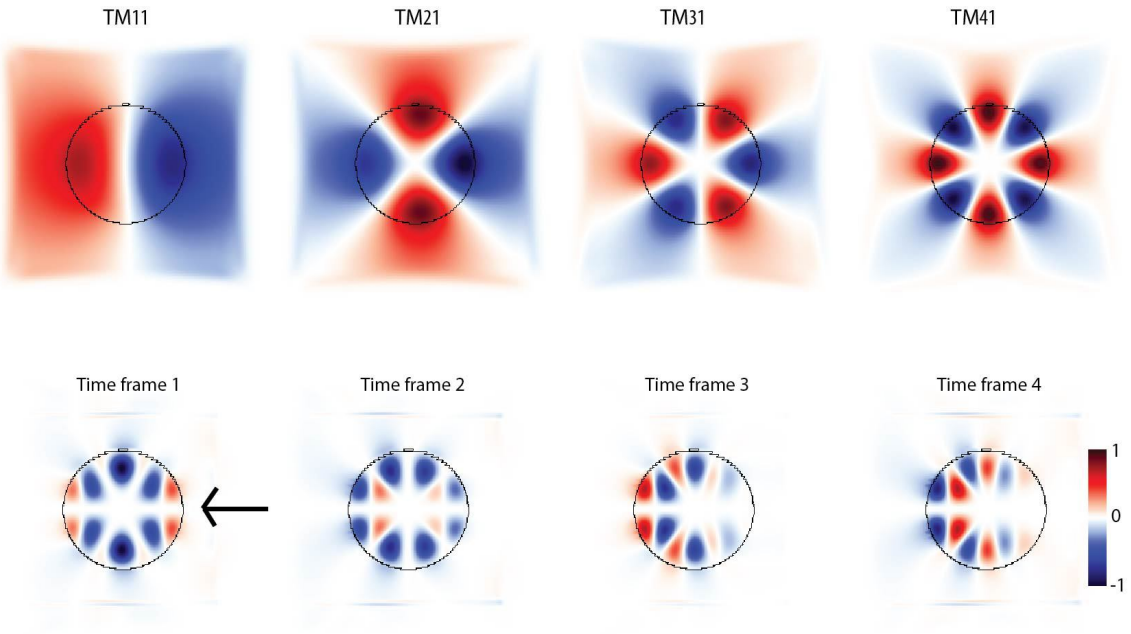

Figure 3.4 (Top) Resonant modes in an infinitely long cylinder of GaAs with diameter of 220 nm with light incident parallel to NW axis. (Bottom) The Poynting vector at different time frames with light incident perpendicular to the NW axis from the right.

observations demonstrate the feasibility to engineer the volumetric mode at certain wavelength, i.e., allow us to optimize absorption or emission at a desired frequency or certain incident optical power by controlling the radius and/or length of a NW thus providing the ability to engineer the absorption spectrum in order to match desired properties.

iThe dependence of the resonant modes on NW radius also suggests the interesting possibility of having tapered structures which can support more than one resonant mode, thus be able to optimize the spectrum of interest. The metalorganic vapor phase epitaxy (MOVPE) or vapor liquid solid (VLS) growth methods are readily capable of forming nanowires with tapered sidewalls. The resultant cavity, however, does not support the superposition of the modes present in cylindrical structures of the same diameter; in fact tapered sidewalls have been identified as the primary loss mechanism for these sub-wavelength cavities. The effect of tapering has been studied for nanopillars that were grown on a silicon substrate with average 5 angles between opposite sidewalls; vertical field profiles for , and modes are shown in Fig. 7 [2]. The modes are primarily confined at the base, and

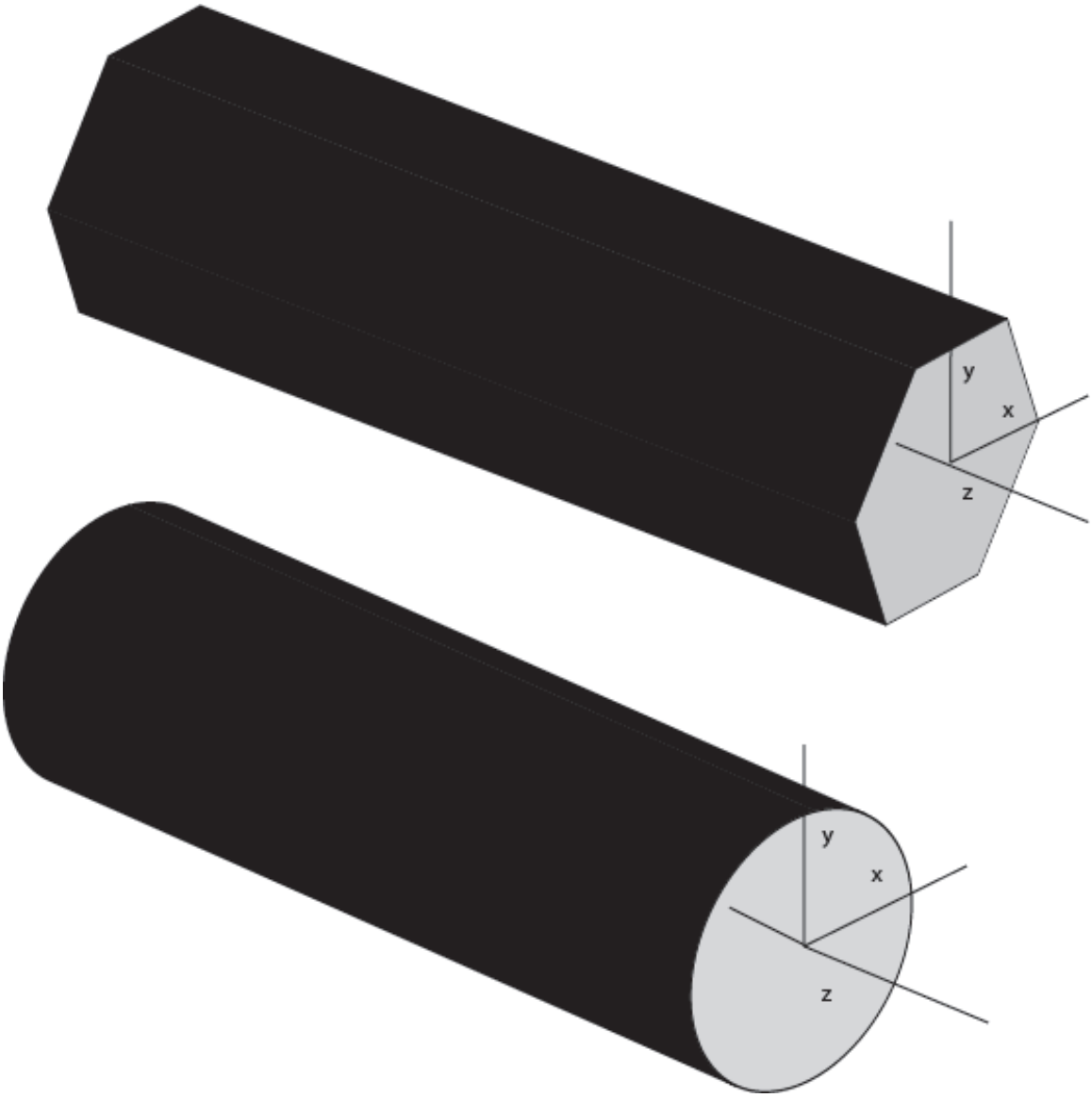

Figure 3.5 Simulation Schematic for Cylindrical and Hexagonal Nanowires

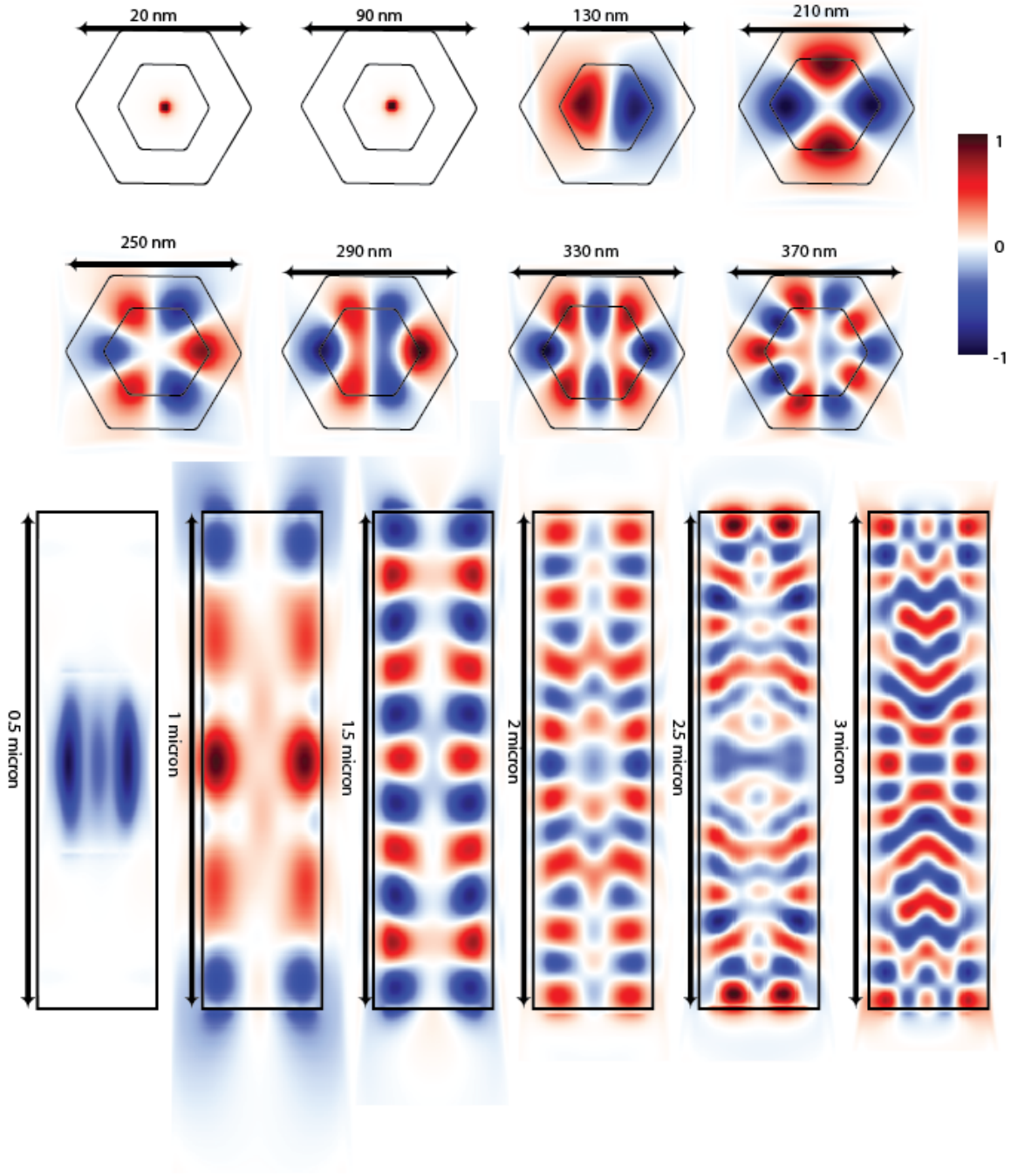

Figure 3.6 Geometric Dependence TM radius variation for different Radius and Diameters

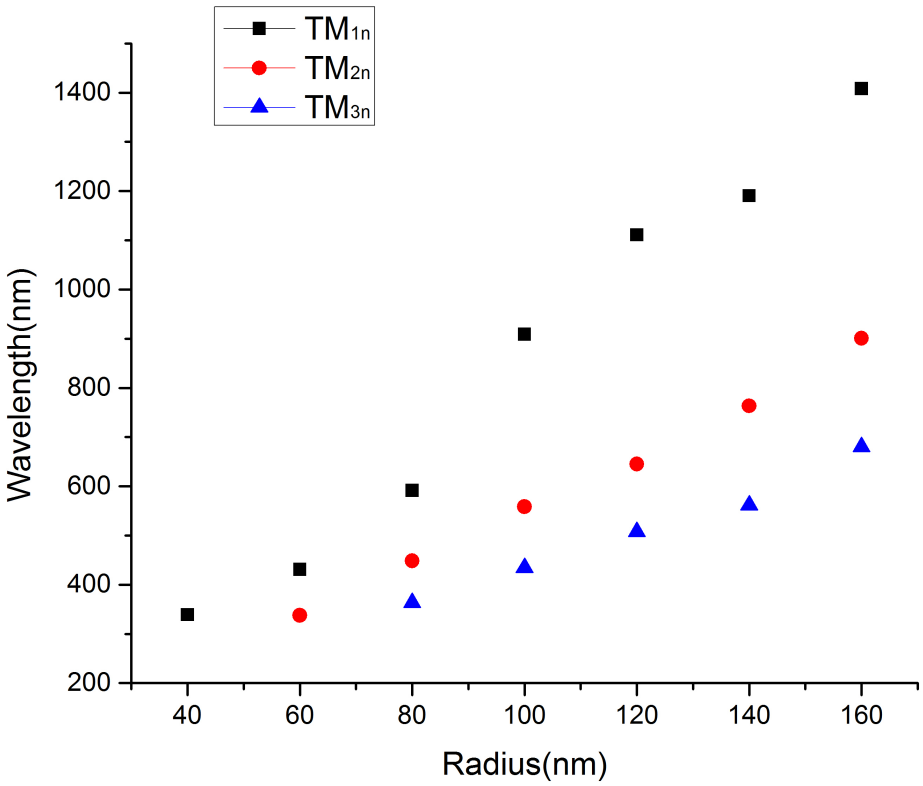

Figure 3.7 Geometric Dependence and Engineering Light with Radius

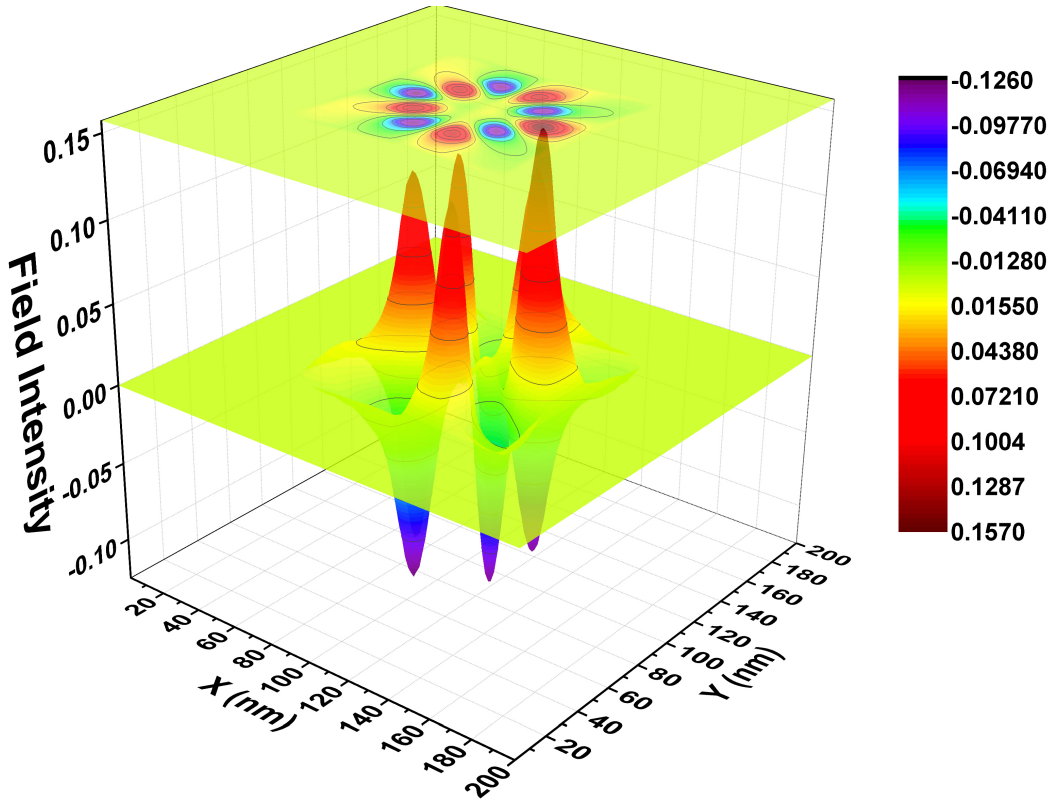

Figure 3.8 3D view of Photon Distribution

become less resonant as they propagate upwards with decreasing of the radius at top. Higher-order axial modes generally have lower quality factor. Physically, the stronger Fabry-Perot characteristic of higher-order axial modes means that their effective longitudinal wave-vector components become stronger, causing larger penetration and loss into the substrate. Nevertheless, from a different perspective, multi-mode resonances can be achieved within certain wavelength range by controlling the tapering angle in order to form small varying radius along the nanostructure axial direction. One can also red- or blue-shift the resonance peaks, since these volumetric resonance modes are dependent on transverse dimensions. Thus, intentioned tapering offers an alternative way to engineering the multi-mode resonances and finer tunability of these resonance peaks.

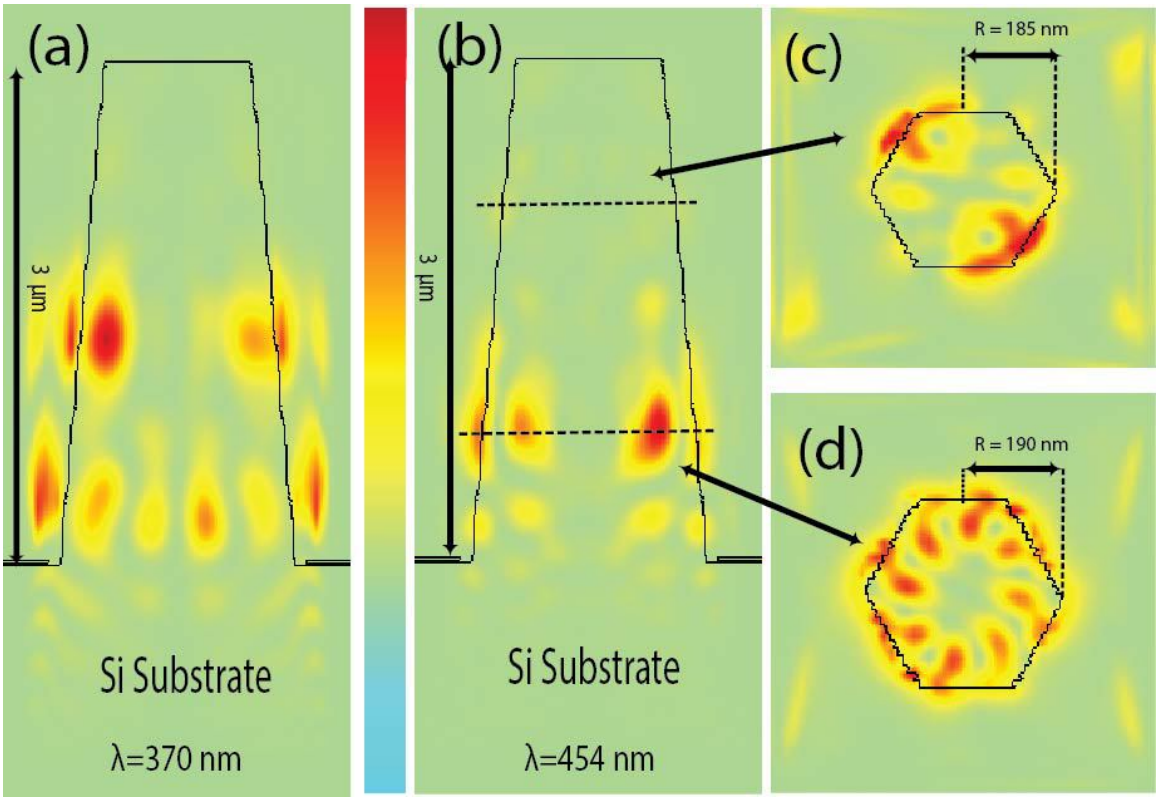

Figure 3.9 Tapering effect of nanowire

CHAPTER 4

REDUCED ELECTRONIC DENSITY DISTRIBUTION

A heterojuntion is basically a p-n junction in a semiconductor between materials of different composition. Normal junctions are between p and n type versions of the same material. But in this case we refer to a juntion formed betewen two group III-arsenide usually a GaAs/AlAs interface or a GaAs/AlGaAs interface. Since they are two differnt materials, the band structure is discontinuous from one material to the other and the band alignment across the interface is typically of type I, i.e. the band gap of the lower bandgap material is positioned energetically within the bandgap of the wider bandgap semiconductor.

Polarization fields The usual growth direction for hexagonal III-V materials is along the polar [0001] axis, for which the crystal lacks inversion symeetry. This will result in the formation of polarization fields. There are two kinds of polarization fields. They are spontaneous polarization (SP) and Piezoelectric polarization (PZ). The spontaneous polarization exists in polar semiconductors with a Wurzite or lower symmetry crystal structure and is related to the deviation of the crystal lattice parameters from the ideal values for the structure, thereby creating molecular dipoles in the material building a polarization field just like that formed in ferroelectrics. This field has a fixed direction along the [0001] c-axis in the Wurtzite lattice. Therefore the field resulting from spontaneous polarization will point along the growth direction and this maximizes pontaneous polarization effect in these systems and renders the problem effectively one-dimensional.

The other type of polarization field, the piezoelectric polarization occurs due to the presence of strain in the system. When two layers are joined together to form a heterojunction, the difference in

the lattice constant between the two materials will lead to a strain . This strain also occurs due tot he difference in the thermal expansion coefficients in the the layers during cool down after growth. This leads to elastic strain in the layers.

4.1 Self-consistent Schrödinger-Poisson Solver

4.1.1 Finite Element Method

The study of energy band structures of heterostructures needs a detailed knowledge of optical and transport properties of the heterostructures. These properties can be found by solving self-consistently Poisson's and Schrödinger's equations for the electron wave functions.

The finite element method (FEM) is a simple and efficient method for solving ordinary differential equations (ODEs) or partial differential equations (PDSs) in problem regions with simple boundaries[36]. FEM can be used to solve for the Schrödinger and Poisson equation self-consistently. A generic formulation for a PDE with the following form:

$$|D|u(x) = f(x) \in \Omega \tag{4.1}$$

where D is an arbitrary operator, and Ω defines the geometry. In order to solve this PDE using FEM, eq. 4.1 has to be rewritten in weak variational form with the boudary conditions:

$$\begin{cases} u(x) = u_0(x) & on \quad \Gamma_D \\ \frac{\partial u}{\partial n} = g_0(x) & on \quad \Gamma_N \end{cases} \tag{4.2}$$

where Γ_D and Γ_N signifies Dirichlet and Neumann boundary condition. By introducing an arbitrary function v and multiplying the PDF with v, then integrating over all the domain Γ and separating every second-order derivative using integration by parts, the original PDE can be carried out in the

weak form as:

$$\int_{\Omega} |D'|(u \cdot v)\ d\Omega + \int_{\Gamma_N} gv\ \partial\Omega = \int_{\Omega} fv\ d\Omega \quad \forall v \in \hat{V} \tag{4.3}$$

where D' is the reduced operator after performing integration by part to the second-order derivatives, and $\hat{V}$ is the function space where an arbitrary function v belongs to. The function u lies in V, which could be different than $\hat{V}$. This continuous variational problem need to be reformulated to discrete problem with discrete space $\hat{V}_d \subset \hat{V}$ and $V \subset V$ so that the boundary conditions can be restated as:

$$\int_{\Omega} |D'|(u_d \cdot v)\ d\Omega + \int_{\Gamma_N} gv\ \partial\Omega = \int_{\Omega} fv\ d\Omega \quad \forall v \in \hat{V}_d \subset \hat{V} \tag{4.4}$$

It is more convenient to use unified notation for linear weak forms $a(u, v) = L(v)$ with $a(u, v) = \int_{\Omega} |D'|(u_d \cdot v)\ d\Omega$ and $L(v) = \int_{\Omega} fv\ d\Omega - \int_{\Gamma_N} gv\partial\Omega$.

4.1.2 Variational form of Schrödinger and Poisson equations

A general Poisson equation for electrostatics is giving by[37]:

$$\frac{d}{dx}(\epsilon_s(x)\frac{d}{dx})\Phi(x) = \frac{-q[N_D(x) - n(x)]}{\epsilon_0} \tag{4.5}$$

where ϵ_s is the dielectric constant of the material, N_D is the ionized donor concentration, Φ is electrostatic potential, and n is the electron density. Since Eq. 4.5 only has a piecewise dielectric constant, the domain can be divided into subdomains by different dielectric constants. The Poisson equation can be rewritten as:

$$\epsilon_s \nabla^2 \Phi(x) = \frac{-q[N_D(x) - n(x)]}{\epsilon_0} \tag{4.6}$$

Note that the operator $|D|$ is replaced by ∇^2, and the source term $f(x)$ is replaced with the scaled difference of the ionized donor concentration and the electron density. Then the Poisson equation can be reformulate to the weak variational form following the previous procedures.

$$\int_\Omega \epsilon_s \epsilon_0 \nabla\Phi\nabla v \; d\Omega = \int_\Omega [-q[N_D(x) - n(x)]]v(x) \; d\Omega \tag{4.7}$$

The weak variational form of Schrödinger's equation can be derived from the general differential form following by the similar manner:

$$-\frac{\hbar^2}{2}\frac{d}{dx}(\frac{1}{m^*(x)}\frac{d}{dx})\psi(x) + V(x)\psi(x) = E\psi(x) \tag{4.8}$$

where $m^*(x)$ is the effective mass. Equation 4.8 can rewritten after taking the effective mass out, as it will remain constant in a single region.

$$\frac{\hbar^2}{2m^*}\nabla^2\psi(x) + [E - V(x)]\psi(x) = 0 \tag{4.9}$$

Multiply both sides by a test function v, which is arbitrary with the condition that it vanishes on the boundaries of the system.

$$\int_\Omega \frac{\hbar^2}{2m^*}\frac{\psi}{x}\frac{v}{x} \; d\Omega + \int_\Omega V(x)\psi(x)v(x) = \int_\Omega E\psi(x)v(x) \; d\Omega \tag{4.10}$$

4.1.3 Numerical Implementation

To obtain the electronic properties, the electrostatic potential $V(x = -q\phi(x) + \triangle E_c(x)$ first sets to zero. Then the envelope functions and the eigen energies are calculated according to the Schrödinger equation 4.8. A Poisson equation 4.5 is solved after the determination of the quasi Fermi level E_F

by solving charge neutrality equation. The electron concentration can now be calculated based on:

$$n(x) = \sum_{k=1}^{m} {\psi^*}_k(x)\psi_k(x)n_k \tag{4.11}$$

$$n_k = \frac{m^*}{\pi\hbar^2}\int_{E_k}^{\infty} \frac{1}{1+e^{(E-E_F)/KT}}dE \tag{4.12}$$

where $\triangle E_c(x)$ is the pseudopotential energy due to the band offset at the heterointerface, n_k is the electron occupation number which can be calculated by Fermi-Dirac distribution function with Fermi level E_F, ψ_k is the wavefunction in the k^{th} state, and E_k is the eigen energy in state k. Finally, a check of the electrostatic potential update decides whether the iteration terminates. The procedure of this Schrödinger-Poisson solver has been demonstrated in the flow chart diagram as in Fig. 4.1.

Implementing the FEM method when solving the Schrödinger and Poisson equations requires the construction of a mesh defining local coordinate surfaces. For each node of this mesh, the unknown eigen functions and eigen values are found, replacing the original differential equations by variational forms. In order to make the FEM method more effective, implementing a small mesh when the wavefunction is changing rapidly and a large mesh during a slow change in the wavefunction is necessary.

4.2 Electronic Distribution in Nanowires

The electronic band structure and the electronic density of cylindrical and hexagonal GaAs/AlGaAs core-shell nanowire are calculated self-consistently by solving Poisson and Schrödinger equations [? ?] using **nextnano³** simulation packages[38], which is a commercial computer aid software with better physical method for the calculation of the quantum mechanical properties of an arbitrary combination of geometries and materials.

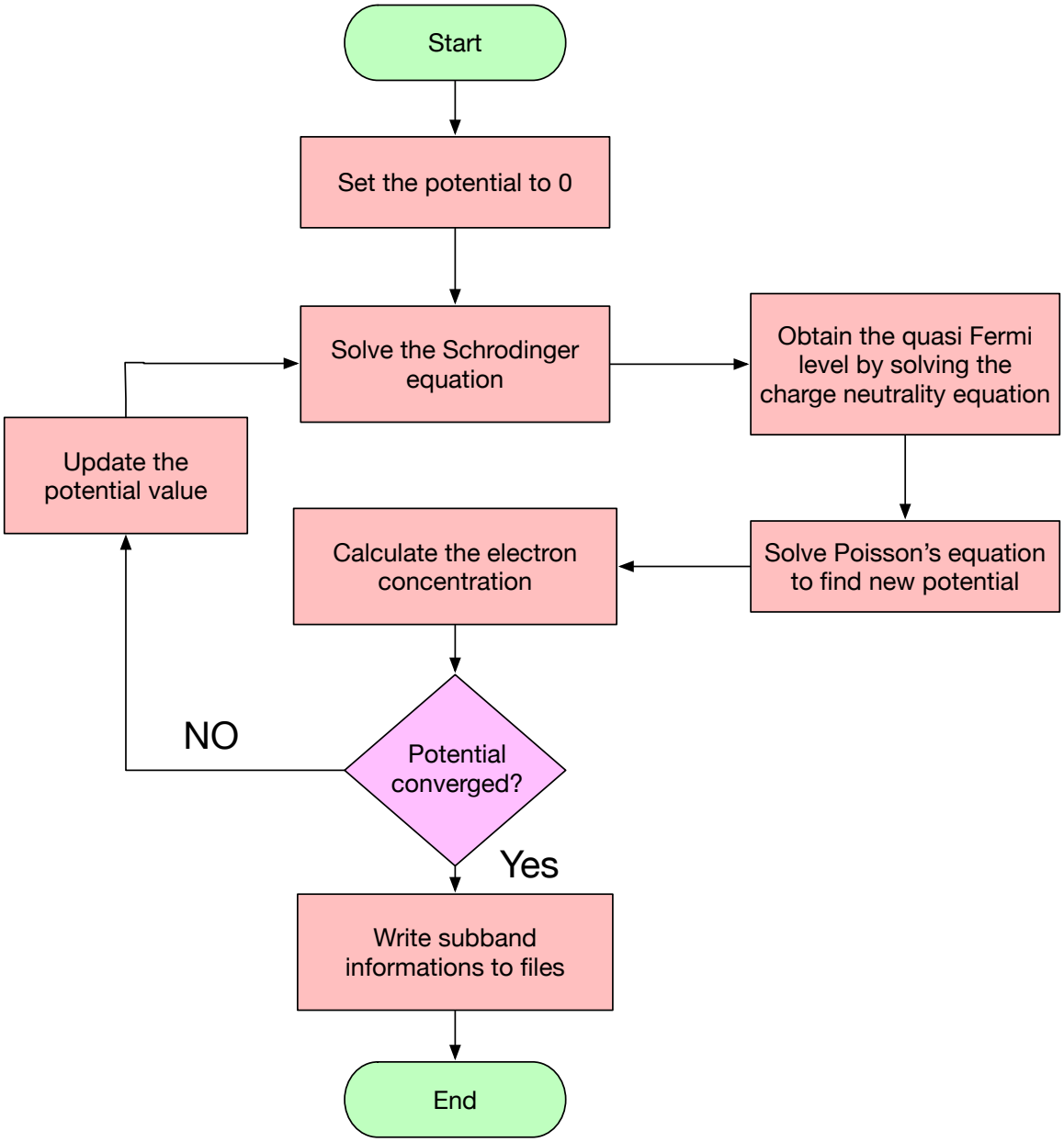

Figure 4.1 A flow chart diagram of the Schrödinger-Poisson solver. The procedure is only discussed for electrons in the conduction band for simplicity but it also hold true for holes in the valence band using analogous formulas.

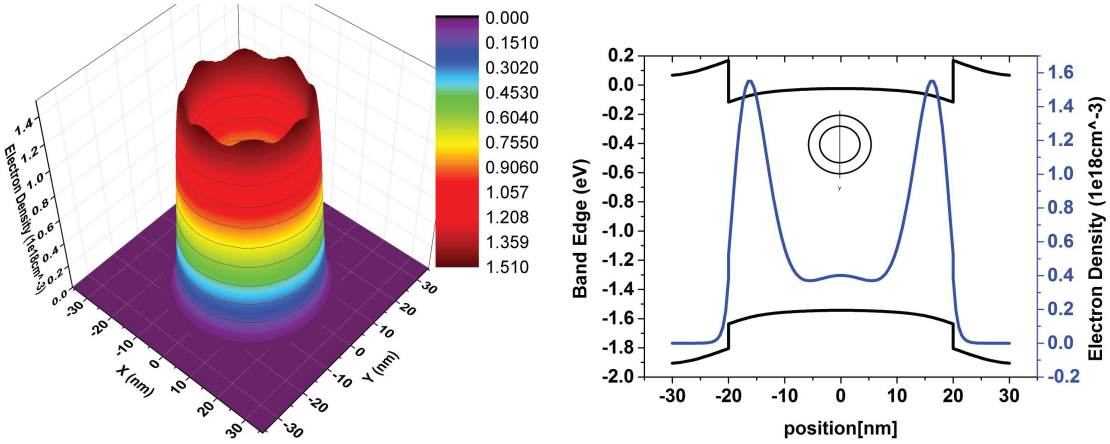

Figure 4.2 (left) Electron charge distribution in 3D illustration. (right) Conduction and valence band bending (black lines) and electron density distribution (blue line) for cylindrical core-shell nanowire. The inset shows the data captured from a vertical slice of the simulated structure.

4.2.1 Cylindrical Core-Shell Nanowire

The cylindrical core-shell nanowire has been investigated with a radius of 20nm GaAs core and 15nm AlGaAs shell. An additional Si-doped AlGaAs layer with a 0.33 mole fraction is placed between the core and shell. The thickness of this layers is 5 nm. The left part of Fig. 4.2 shows the electron density distribution in 3D view. A free-electron gas is formed in the GaAs core and at the inner heterointerface with a small fluctuation of density along the interface. There is a very small amount of electron gas distributed at the center of the core. Further simulation with different doping density ρ_D shows similar distribution of the electron gas but very small variation of the magnitude of the intensity. On the right part of Fig. 4.2, the black line represents the conduction and valence band bending and the blue line shows the electron density along the vertical cut of this cylindrical CSNW.

4.2.2 Hexagonal Core-shell Nanowire

Due to the hetero-interface between the core and shell and the piezoelectric force at the corners, the electronic states distribution inside of the hexagonal core-shell nanowire is not always three-dimensional case or two-dimensional like in cylindrical NWs. Lower-dimensional electron gas arises with increased doping density. A delta-doped hexagonal CSNW heterostructure has been simulated.

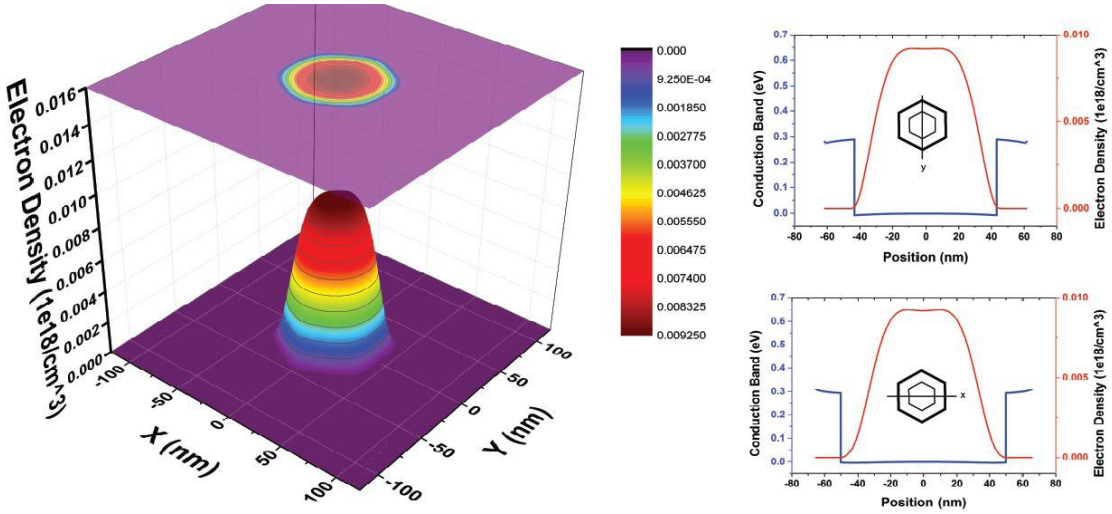

Figure 4.3 (left) Three dimensional electron charge distribution in 3D illustration. (right) Conduction and valence band bending (blue lines) and electron density distribution (red line) for hexagonal core-shell nanowire with a low doping density. The inset shows the data captured from a (top) vertical or (bottom) horizontal slice of the simulated structure.

The radius of GaAs core and AlGaAs shell is 43.3 nm and 45 nm, respectively, with a 17.3 nm AlGaAs spacer in between. The thickness of Si-doped AlGaAs is 1.6 nm with a 0.33 mole fraction of AlGaAs. This Si-doped AlGaAs layer is used to populate a (triangular) quantum well at the heterointerfaces. Such a well can also be produced by sandwiching a GaAs layer radially between two wider bandgap materials.

The left part of Fig. 4.3, 4.4 and 4.5 shows the spatial distribution of the free-electron gas for the three values of the doping density indicated as (Fig. 4.3) $\rho_D = 9.2 \times 10^{18} cm^{-3}$, (Fig. 4.4) $\rho_D = 9.6 \times 10^{18} cm^{-3}$, (Fig. 4.3) $\rho_D = 1.5 \times 10^{19} cm^{-3}$. On the right part, the electronic band structure (blue line) and the electronic density (red line) of hexagonal GaAs/AlGaAs core-shell nanowire are depicted for vertical slice (top, right) or horizontal slice (bottom, right).

At the lowest doping, shown in Fig. 4.3, the charge is distributed deep into the core. The distribution is only slightly modulated (right panels) crossing the core along either the y cross section or x cross section, and slightly depleted in the center of the core.

As the doping is increased in Fig. 4.4, the charge depletion in the center is more pronounced, and the

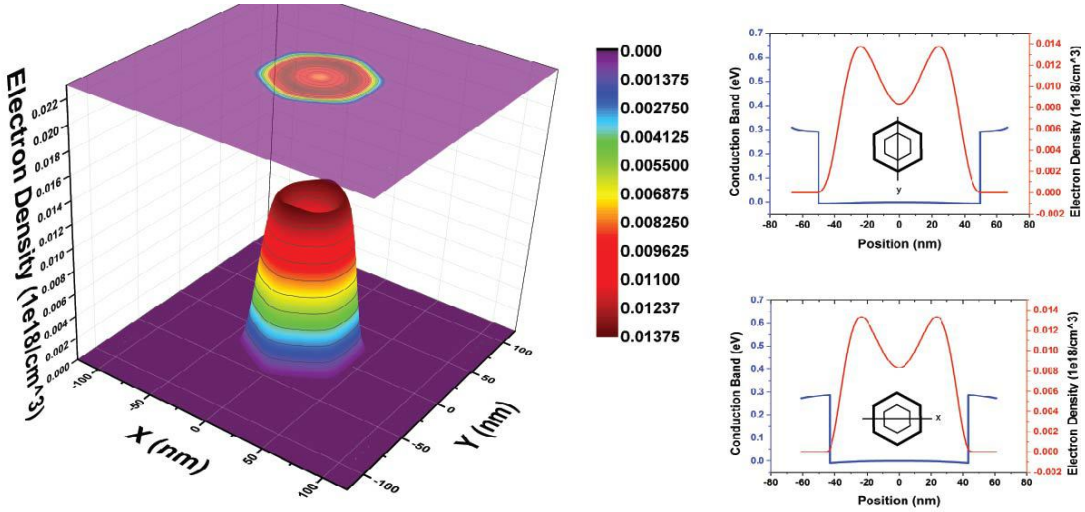

Figure 4.4 (left) Two dimensional electron charge distribution in 3D illustration. (right) Conduction and valence band bending (blue lines) and electron density distribution (red line) for hexagonal core-shell nanowire with a moderate doping density. The inset shows the data captured from a (top) vertical or (bottom) horizontal slice of the simulated structure.

charge moves toward the heterojunction interface, leaving this "volcano" like charge distribution in the left part of Fig. 4.4. The two-dimensional electron gases (2DEG) are formed at the heterointerface of GaAs core and AlGaAs shell.

As the doping is further increased in Fig. 4.5, the shell 2DEG form at the six (6) core-shell hetero-interface facets, with six (6) pillars of one-dimensional electron gas (1DEG) forming at the 6 vortices. In addition, as shown in the right part of the Fig. 4.3, 4.4 and 4.5, the electronic density of Fig. 4.5 is around two orders of magnitude higher than 2DEG and bulk counterparts. The results also matched the other groups' simulation results very well[39,40].

4.3 Conclusions

In this chapter, the finite-element-method implemented self-consistent Shrödinger-Poisson solver has been discussed. In addition, a cylindrical and hexagonal core-shell nanowire structure has been simulated and compared with different doping density. The simulated results show unique electron density distribution in hexagonal CSNW with large doping density. This unique distribution of

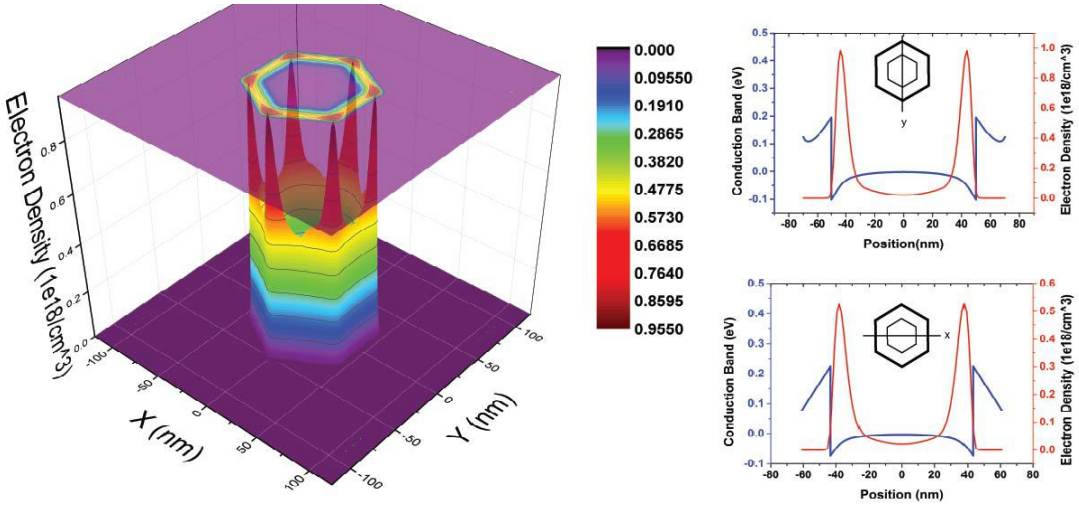

Figure 4.5 (left) One dimensional electron charge distribution in 3D illustration. (right) Conduction and valence band bending (blue lines) and electron density distribution (red line) for hexagonal core-shell nanowire with a high doping density. The inset shows the data captured from a (top) vertical or (bottom) horizontal slice of the simulated structure.

electrons has also been verified experimentally by electron holographic tomography [41]

CHAPTER 5

DIMENSIONAL DEPENDENCE OF OPTICAL TRANSITION RATES

5.1 Time-dependent Perturbation Theory

5.1.1 Fermi's Golden Rule

When the semiconductor illuminated by light, the interaction between the photons and the electrons in the semiconductor can be described by the Hamiltonian:

$$\mathcal{H} = \frac{1}{2m_0}(\boldsymbol{p} - e\boldsymbol{A})^2 + V(\boldsymbol{r}) \tag{5.1}$$

where m_0 is the free electron mass, $e = -|e|$ for electrons, $\boldsymbol{A}$ is the vector potential accounting for the presence of the electromagnetic field, and $V(\boldsymbol{r})$ is the periodic crystal potential.

The Hamiltonian can be expanded into

$$\mathcal{H} = \tfrac{1}{2m_0}(\boldsymbol{p} - e\boldsymbol{A})^2 + V(\boldsymbol{r}) \quad \approx \mathcal{H}_0 + \mathcal{H}' \tag{5.2}$$

where $\mathcal{H}_0$ is the unperturbed Hamiltonian and $\mathcal{H}'$ is considered as a perturbation due to light

$$\mathcal{H}_0 = \frac{\boldsymbol{p}^2}{2m_0} + V(\boldsymbol{r}) \tag{5.3}$$

$$\mathcal{H}' = -\frac{e}{m_0}\boldsymbol{A}\boldsymbol{p} \tag{5.4}$$

and consider the coulomb gauge has been used.

$$\nabla \cdot \boldsymbol{A} = 0 \tag{5.5}$$

noting that $\boldsymbol{p} = (\hbar/i)\nabla$, so $\boldsymbol{p}\cdot\boldsymbol{A} = (\frac{\hbar}{i})\nabla\cdot\boldsymbol{A} = \boldsymbol{A}\cdot\boldsymbol{p}$. And since we know $\boldsymbol{p} \approx \hbar k \approx \hbar\frac{\pi}{a}$, and a is the lattice constant, usually have a value of $5\mathring{A}$, so $|e\boldsymbol{A}| \ll |\boldsymbol{p}|$, then we can drop the last term $\frac{e^2\boldsymbol{A}^2}{2m_0}$, because it is much smaller than the terms linear in $\boldsymbol{A}$.

Assume the vector potential for the optical electric field of the form

$$\boldsymbol{A} = \hat{e}\boldsymbol{A}_0 \cos k_{op}\cdot\boldsymbol{r} - \omega t \quad = \hat{e}\frac{A_0}{2}e^{ik_{op}\cdot\boldsymbol{r}}e^{-i\omega t} + \hat{e}\frac{A_0}{2}e^{-ik_{op}\cdot\boldsymbol{r}}e^{i\omega t} \tag{5.6}$$

where $\boldsymbol{k_{op}}$ is the wave vector, ω is the optical angular frequency, and $\hat{e}$ is a unit vector in the direction of the optical electric field, we have

$$\boldsymbol{E}(\boldsymbol{r},t) = -\frac{\partial\boldsymbol{A}}{\partial t} = -\hat{e}\omega_{A0}\sin\boldsymbol{k_{op}}\cdot\boldsymbol{r} - \omega t \tag{5.7}$$

$$\boldsymbol{H}(\boldsymbol{r},t) = \frac{1}{\mu}\nabla\times\boldsymbol{A} = -\frac{1}{\mu}\boldsymbol{k}_{\mathrm{op}}\times\hat{e}A_0\sin(\boldsymbol{k}_{\mathrm{op}}\cdot\boldsymbol{r} - \omega t) \tag{5.8}$$

where we have used the fact that the scalar potential φ vanishes ($\rho = 0$) for the optical field, and $\mu = \mu_0$, the permeability of the free space. The Poynting vector for the power intensity (W/cm^2) is

given by

$$\boldsymbol{P}(\boldsymbol{r},t)=\boldsymbol{E}(\boldsymbol{r},t)\times\boldsymbol{H}(\boldsymbol{r},t)=\hat{k}\boldsymbol{k}_{\mathrm{op}}\frac{\omega {A_0}^2}{\mu}\ (\boldsymbol{k}_{\mathrm{op}}\cdot\boldsymbol{r}-\omega t) \tag{5.9}$$

which is pointing along the direction of wave propagation $\boldsymbol{k}_{\mathrm{op}}$. The time average of the Poynting flux is simply

$$\begin{aligned}\boldsymbol{P}=|\boldsymbol{P}(\boldsymbol{r},t)| &= \tfrac{\omega {A_0}^2}{2\mu}\boldsymbol{k}_{\mathrm{op}}\\ &= \tfrac{\omega^2 {A_0}^2 n_r}{2\mu c}\\ &= \tfrac{\omega^2 {A_0}^2 n_r\sqrt{\mu_0\varepsilon_0}}{2\mu_0}\\ &= \tfrac{\omega^2 {A_0}^2 n_r\sqrt{\varepsilon_0}}{2\sqrt{\mu_0}}\\ &= \tfrac{\omega^2 {A_0}^2 n_r\sqrt{\varepsilon_0}\sqrt{\varepsilon_0}}{2\sqrt{\mu_0}\sqrt{\varepsilon_0}}\\ &= \tfrac{\omega^2 {A_0}^2 n_r\varepsilon_0 c}{2}\end{aligned} \tag{5.10}$$

Noting the time average of the $\sin^2()$ function is $\frac{1}{2}$ and $\boldsymbol{k}_{\mathrm{op}}=\omega\sqrt{\mu\varepsilon_0}=\frac{\omega}{\nu}=\frac{\omega}{\frac{c}{n_r}}$, $c=\frac{1}{\sqrt{\mu_0\varepsilon_0}}$

The interaction Hamiltonian

$$\begin{aligned}\mathcal{H}'(\boldsymbol{r},t) &= -\tfrac{e}{m_0}\ \boldsymbol{A}(\boldsymbol{r},t)\cdot\boldsymbol{p}\\ &= \mathcal{H}'(\boldsymbol{r})\,\boldsymbol{e}^{-\boldsymbol{i\omega t}}+\mathcal{H}'^{+}(\boldsymbol{r})\,\boldsymbol{e}^{+\boldsymbol{i\omega t}}\end{aligned} \tag{5.11}$$

where

$$\mathcal{H}'(\boldsymbol{r})=-\frac{eA_0\boldsymbol{e}^{\boldsymbol{ik}_{\mathrm{op}}\cdot\boldsymbol{r}}}{2m_0}\ \cdot\hat{e}\cdot\boldsymbol{p} \tag{5.12}$$

The superscript "+" means the Hermitian adjoint operator.

The transition rate for the absorption of a photon:

If the electron is at state a initially. And assume $E_b > E_a$

$$W_{\text{abs}} = \frac{2\pi}{\hbar} \left| \left\langle b \middle| \mathcal{H}' \left(\boldsymbol{r} \right) \middle| a \right\rangle \right|^2 \delta(E_b - E_a - \hbar\omega) \tag{5.13}$$

The total upward transition rate per unit volume ($s^{-1}\text{cm}^{-3}$) in the crystal taking into account the probability that state a is occupied and state b is empty:

$$R_{a\to b} = \frac{2}{V} \sum_{\boldsymbol{k}_a} \sum_{\boldsymbol{k}_b} \frac{2\pi}{\hbar} \left| \mathcal{H}'_{\text{ba}} \right|^2 \delta(E_b - E_a - \hbar\omega) f_a (1 - f_b) \tag{5.14}$$

where we sum over the initial and final states and assume that the Fermi-Dirac distribution f_a is the probability that the state a is occupied. A similar expression holds for f_b with E_a replaced by E_b, and $(1 - f_b)$ is the probability that the state b is empty. The prefactor 2 takes into account the sum over spins, and the matrix element $\mathcal{H}'_{\text{ba}}$ is given by **Fermi's Golden Rule**

$$\mathcal{H}'_{\text{ba}} \equiv \left| \left\langle b \middle| \mathcal{H}' \left(\boldsymbol{r} \right) \middle| a \right\rangle \right| = \int \Psi_b^* \left(\boldsymbol{r} \right) H' \left(\boldsymbol{r}, t \right) \Psi_a \left(\boldsymbol{r} \right) d^3 \boldsymbol{r} \tag{5.15}$$

Similarly, the transition rate for the emission of a photon if an electron is initially at state b is

$$W_{\text{ems}} = \frac{2\pi}{\hbar} \left| \left\langle a \middle| \mathcal{H}' \left(\boldsymbol{r} \right) \middle| b \right\rangle \right|^2 \delta(E_a - E_b + \hbar\omega) \tag{5.16}$$

The downward transition rate per unit volume ($s^{-1}\text{cm}^{-3}$) is

$$R_{b\to a} = \frac{2}{V} \sum_{\boldsymbol{k}_a} \sum_{\boldsymbol{k}_b} \frac{2\pi}{\hbar} \left| \mathcal{H}'^{+}_{\text{ab}} \right|^2 \delta(E_a - E_b + \hbar\omega) f_b (1 - f_a) \tag{5.17}$$

Using the even property of the delta function, $\delta(-x) = \delta(x)$, and $\mathcal{H}'_{\text{ba}} = \mathcal{H}'^{+}_{\text{ab}}$, the net upward

transition rate per unit volume can be written as

$$R = R_{a\to b} - R_{b\to a} = \frac{2}{V}\sum_{\boldsymbol{k}_a}\sum_{\boldsymbol{k}_b}\frac{2\pi}{\hbar}\left|\mathcal{H}^{'}{}_{\mathrm{ba}}\right|^2\delta(E_b - E_a - \hbar\omega)(f_a - f_b) \tag{5.18}$$

The absorption coefficient $\alpha(1/cm)$ in the crystal is the fraction of photons absorbed per unit distance:

$$\alpha = \frac{\text{Number of photons absorbed per second per unit volume}}{\text{Number of injected photons per second per unit area}} \tag{5.19}$$

The injected number of photons per second per unit area is the optical intensity $P(W/\mathrm{cm}^2)$ divided by the energy of a photon $\hbar\omega$:

$$\alpha\left(\hbar\omega\right) = \frac{R}{\frac{P}{\hbar\omega}} = \frac{\hbar\omega}{(\frac{n_r c\epsilon_0\omega^2 A_0^2}{2})}R \tag{5.20}$$

Using the long wavelength approximation that $\boldsymbol{A}\left(\boldsymbol{r}\right) = \boldsymbol{A}e^{i\boldsymbol{k}_{\mathrm{op}}\cdot r} \approx \boldsymbol{A}$, we find that the matrix element can be written in terms of the momentum matrix element

$$\mathcal{H}^{'}{}_{\mathrm{ba}} = -\frac{e}{m_0}\ \boldsymbol{A}\cdot\langle b|\boldsymbol{p}|a\rangle = \frac{eA_0}{2m_0}\ \cdot\hat{e}\cdot\boldsymbol{p}_{\mathrm{ba}} \tag{5.21}$$

The absorption coefficient becomes

$$\alpha\left(\hbar\omega\right) = C_0\tfrac{2}{V}\textstyle\sum_{\boldsymbol{k}_a}\sum_{\boldsymbol{k}_b}\left|\hat{e}\cdot\boldsymbol{p}_{\mathrm{ba}}\right|^2\delta(E_b - E_a - \hbar\omega)(f_a - f_b)$$

$$C_0 = \tfrac{\pi e^2}{n_r\varepsilon_0 c m_0^2\omega} \tag{5.22}$$

5.2 Interband Absorption for a Bulk Semiconductor

Evaluate the optical matrix element:

$$\mathcal{H}'_{\text{ba}} = \left\langle b \middle| -\frac{e\boldsymbol{A}(\boldsymbol{r})}{m_0} \cdot \boldsymbol{p} \middle| a \right\rangle \tag{5.23}$$

The vector potential for the optical field is

$$\boldsymbol{A}(\boldsymbol{r}) = \boldsymbol{A} \cdot e^{i\boldsymbol{k}_{\text{op}} \cdot r} = \frac{\hat{e}A_0}{2} e^{i\boldsymbol{k}_{\text{op}} \cdot r} \tag{5.24}$$

The Bloch functions for electrons in the valence band E_a and the conduction band E_b are:

$$\Psi_a(\boldsymbol{r}) = u_v(\boldsymbol{r}) \frac{e^{i\boldsymbol{k_v} \cdot r}}{\sqrt{V}} \tag{5.25}$$

$$\Psi_b(\boldsymbol{r}) = u_c(\boldsymbol{r}) \frac{e^{i\boldsymbol{k_c} \cdot r}}{\sqrt{V}} \tag{5.26}$$

where $u_v(\boldsymbol{r})$ and $u_c(\boldsymbol{r})$ are the periodic parts of the Bloch functions, and the remainders are the envelope functions (plane waves) for a free electron. The momentum matrix element is derived from

$$\begin{aligned}
\mathcal{H}'_{\text{ba}} &= -\tfrac{eA_0}{2m_0}\ \hat{e} \cdot \int \Psi_b^* e^{i\boldsymbol{k}_{\text{op}} \cdot r} \boldsymbol{p} \Psi_a d^3\boldsymbol{r} \\
&= -\tfrac{eA_0}{2m_0}\ \hat{e} \cdot \int u_c(\boldsymbol{r}) e^{i\boldsymbol{k_c} \cdot r} e^{i\boldsymbol{k}_{\text{op}} \cdot r} \left[\left(\tfrac{\hbar}{i} \nabla u_v(\boldsymbol{r}) \right) e^{i\boldsymbol{k_v} \cdot r} + \hbar \boldsymbol{k_v} u_v(\boldsymbol{r}) e^{i\boldsymbol{k_v} \cdot r} \right] \tfrac{d^3\boldsymbol{r}}{V} \\
&\approx -\tfrac{eA_0}{2m_0}\ \hat{e} \cdot \int_\Omega {u_c}^*(\boldsymbol{r}) \tfrac{\hbar}{i} \nabla {u_v}(\boldsymbol{r}) \tfrac{d^3\boldsymbol{r}}{\Omega} \int_V e^{i(-\boldsymbol{k_c} + \boldsymbol{k}_{\text{op}} + \boldsymbol{k_v}) \cdot r} \tfrac{d^3\boldsymbol{r}}{V} \\
&= -\tfrac{eA_0}{2m_0}\ \hat{e} \cdot \boldsymbol{p}_{\text{cv}} \delta_{\boldsymbol{k_c}, \boldsymbol{k}_{\text{op}} + \boldsymbol{k_v}}
\end{aligned} \tag{5.27}$$

$$\boldsymbol{p}_{\mathrm{cv}} = \int_{\Omega} {u_c}^*(\boldsymbol{r}) \frac{\hbar}{i} \nabla u_{\ v}(\boldsymbol{r}) \frac{d^3\boldsymbol{r}}{\Omega} \tag{5.28}$$

where we noted that $\left[{u_c}^*(\boldsymbol{r}) \frac{\hbar}{i} \nabla u_v(\boldsymbol{r})\right]$ and $[{u_c}^*(\boldsymbol{r}) u_v(\boldsymbol{r})]$ are periodic functions with the period of a unit cell, whereas the envelope functions are slowly varying functions over a unit cell. Therefore, the integral over $d^3\boldsymbol{r}$ can be separated into the product of two integrals, one over the unit cell Ω for the periodic part, and the other over the slowly varying part. In another word, we use the approximation:

$$\int_V \left[{u_c}^*(\boldsymbol{r}) \frac{\hbar}{i} \nabla u_{\ v}(\boldsymbol{r}) \right] F(\boldsymbol{r}) d^3\boldsymbol{r} \approx \int_V F(\boldsymbol{r}) d^3\boldsymbol{r} \int_{\Omega} {u_c}^*(\boldsymbol{r}) \frac{\hbar}{i} \nabla u_{\ v}(\boldsymbol{r}) \frac{d^3\boldsymbol{r}}{\Omega} \tag{5.29}$$

where $F(\boldsymbol{r})$ is slowly varying over a unit cell, and we have used the periodic property of the Bloch periodic functions

$${u_c}^*(\boldsymbol{r}) \frac{\hbar}{i} \nabla u_{\ v}(\boldsymbol{r}) = \sum_{\boldsymbol{G}} \boldsymbol{C}_{\boldsymbol{G}} e^{i\boldsymbol{G}\cdot r} \tag{5.30}$$

where the vectors $\boldsymbol{G}'s$ are the reciprocal lattice vectors. Because $F(\boldsymbol{r})$ is slowly varying over a unit cell, we may approximate $F(\boldsymbol{r}+\boldsymbol{R}) = F(\boldsymbol{R})$ and put it outside of the integral over a unit cell. Here the $\boldsymbol{R}$s are the lattice vectors, and $e^{i\boldsymbol{G}\cdot\boldsymbol{R}} = 1.\omega$ is the volume of a unit cell. Note that the orthogonal property

$$\begin{gathered} \textstyle\int_{\Omega} {u_c}^* u_v d^3\boldsymbol{r} = 0, \\ \textstyle\frac{1}{\Omega} \int_{\Omega} {u_c}^* u_c d^3\boldsymbol{r} = \frac{1}{\Omega} \int_{\Omega} {u_v}^* u_v d^3\boldsymbol{r} = 1 \end{gathered} \tag{5.31}$$

From the matrix element, we see the momentum conservation

$$\hbar \boldsymbol{k}_c = \hbar \boldsymbol{k}_v + \hbar \boldsymbol{k}_{\mathrm{op}} \tag{5.32}$$

is obeyed. The electron at the final state has its crystal momentum $\hbar \boldsymbol{k}_{\mathrm{c}}$ equal to its initial momentum$\hbar \boldsymbol{k}_v$ plus the photon momentum$\hbar \boldsymbol{k}_{\mathrm{op}}$. Because $\boldsymbol{k}_{\mathrm{op}} \sim \frac{2\pi}{\lambda_0}$, and the magnitudes $\boldsymbol{k}_{\mathrm{c}}$, $\boldsymbol{k}_{\mathrm{v}}$ are of the order $\frac{2\pi}{a_0}$, where a_0 is the lattice constant of the semiconductors, which is typically of the order $5.5\mathring{A}$ and is much smaller than we may ignore $\boldsymbol{k}_{\mathrm{op}}$ and obtain

$$\mathcal{H}^{'}{}_{\mathrm{ba}} \approx -\frac{eA_0}{2m_0}\ \hat{e} \cdot \boldsymbol{p}_{\mathrm{cv}} \delta_{\boldsymbol{k_c}, \boldsymbol{k_v}} \tag{5.33}$$

which is the **K**-selection Rule.

1) Interband momentum matrix element $\boldsymbol{p}_{\mathrm{cv}}$ depend only on the periodic parts of the Bloch functions (u_c and u_v),

2) The original optical momentum matrix element $\boldsymbol{p}_{\mathrm{ab}}$, depends on the full wave functions (i.e. including the envelope function).

Using the **K**-selection rule in the matrix element, we find that the absorption coefficient for a bulk semiconductor is

$$\alpha\left(\hbar\omega\right) = C_0 \tfrac{2}{V} \textstyle\sum_{\boldsymbol{k}_a} \sum_{\boldsymbol{k}_b} |\hat{e} \cdot \boldsymbol{p}_{\mathrm{cv}}|^2 \delta(E_c - E_v - \hbar\omega)(f_v - f_c)$$

$$C_0 = \tfrac{\pi e^2}{n_r \varepsilon_0 c m_0^2 \omega} \tag{5.34}$$

where the Fermi-Dirac distributions for the electrons in the valence bend and in the conduction band

are, respectively.

$$f_v(k) = \frac{1}{1+e^{\frac{(E_v(k)-F_v)}{\mathrm{KT}}}}, f_c(k) = \frac{1}{1+e^{\frac{(E_c(k)-F_c)}{\mathrm{KT}}}} \tag{5.35}$$

Assume:

1) $\boldsymbol{k}_{\mathrm{c}} = \boldsymbol{k}_{\mathrm{v}} = \boldsymbol{k}$, $F_v = F_c = E_F$ (thermal equilibrium)

2) $f_v = 1$ *and* $f_c = 0$

3) $|\hat{e} \cdot \boldsymbol{p}_{\mathrm{cv}}|^2$ is independent of $\boldsymbol{k}$ and denote the absorption spectrum at thermal equilibrium.

$$\alpha(\hbar\omega) = C_0 |\hat{e} \cdot \boldsymbol{p}_{\mathrm{cv}}|^2 \int \frac{2d^3\boldsymbol{k}}{(2\pi)^3} \delta(E_g + \frac{\hbar^2\boldsymbol{k}^2}{2m_r^*} - \hbar\omega) \tag{5.36}$$

where used the reduced effective mass m_r^*

$$E_c = E_g + \frac{\hbar^2\boldsymbol{k}^2}{2m_r^*} \quad E_v = -\frac{\hbar^2\boldsymbol{k}^2}{2m_r^*}$$
$$\frac{1}{m_r^*} = \frac{1}{m_e^*} + \frac{1}{m_h^*}$$

Here all energies are measured from the top of the valence band. Therefore, both E_c and F_c contain the band-gap energy E_g. Let

$$X = E_g + E - \hbar\omega \quad E = \frac{\hbar^2\boldsymbol{k}^2}{2m_r^*} \tag{5.37}$$

we find, by a change of variables, the integration can be carried out with the contribution at $X = 0$, *and* $E = \hbar\omega - E_g$

$$\alpha\left(\hbar\omega\right) = C_0 \left|\hat{e}\cdot\boldsymbol{p}_{\mathrm{cv}}\right|^2 \rho_r\left(\hbar\omega - E_g\right) \tag{5.38}$$

$$\rho_r\left(\hbar\omega - E_g\right) = \tfrac{1}{2\pi^2}\left(\tfrac{2m_r^*}{\hbar^2}\right)^{\frac{3}{2}}\left(\hbar\omega - E_g\right)^{\frac{1}{2}} \tag{5.39}$$

Therefore, the absorption coefficient depends on the momentum matrix element and the joint optical density of states. Below the band-gap energy E_g, the absorption does not occur because the photons see a forbidden band gap.

5.3 Interband Absorption and Gain in A Quantum Well

The central cell functions in the quantum wells are relatively unaffected by the presence of the confining potential. There are only two changes compared to bulk semiconductor, first, the nature of wavefunction for the low lying states are confined to the well region, second, the density of the state have the usual step-like form for parabolic 2-dimensional bends.

Ignore the excitonic effects due to the Coulomb interaction between electrons and holes.

Within a two-band model, the Bloch wave functions can be described by

$$\Psi_a\left(\boldsymbol{r}\right) = u_v(\boldsymbol{r})\frac{e^{i\boldsymbol{k_t}\cdot\rho}}{\sqrt{A}}g_m(z) \tag{5.40}$$

for a hole wave function in the heavy-hole or a light-hole subband m. and

$$\Psi_b\left(\boldsymbol{r}\right) = u_c(\boldsymbol{r})\frac{e^{i\boldsymbol{k_t}\cdot\rho}}{\sqrt{A}}\Phi_n(z) \tag{5.41}$$

for an electron in the conduction subband n. The momentum matrix element $\boldsymbol{p}_{\mathrm{ba}}$ is given by

$$\boldsymbol{p}_{\mathrm{ba}} = \langle\Psi_b|\boldsymbol{p}|\Psi_a\rangle \approx \langle u_c|\boldsymbol{p}|u_v\rangle\,\delta_{k_t,k_t'}\; I_{\mathrm{hm}}^{\mathrm{en}} \tag{5.42}$$

where

$$I_{\mathrm{hm}}^{\mathrm{en}} = \int_{-\infty}^{+\infty} \mathrm{dz}\Phi_n^*(z) g_m(z) \tag{5.43}$$

- This is the overlap integral of the conduction and valence band envelope functions
- **K**-Selection rule applied
- Take into account the quantization of the electron and hole energies E_a and E_b

$$E_a = E_{\mathrm{hm}} - \frac{\hbar^2 \boldsymbol{k_t}^2}{2m_h^*} \tag{5.44}$$

$$E_b = E_g + E_{\mathrm{en}} + \frac{\hbar^2 \boldsymbol{k_t}^2}{2m_e^*} \tag{5.45}$$

And $E_{\mathrm{hm}} < 0$,

$$E_b - E_a = E_{\mathrm{hm}}^{\mathrm{en}} + E_t, E_t = \frac{\hbar^2 \boldsymbol{k_t}^2}{2m_e^*} \tag{5.46}$$

where

$$E_{\mathrm{hm}}^{\mathrm{en}} = E_g + E_{\mathrm{en}} - E_{\mathrm{hm}} \tag{5.47}$$

is the band edge transition energy ($\boldsymbol{k_t} = 0$). The summations over the quantum numbers $\boldsymbol{k}_a$ and $\boldsymbol{k}_b$become summations over $(\boldsymbol{k_t'}, m)$ and $(\boldsymbol{k_t}, n)$. Noting in the matrix element $\boldsymbol{k_t} = \boldsymbol{k_t'}$

$$\alpha\left(\hbar\omega\right) = C_0 \sum_{n,m} \left|I_{\mathrm{hm}}^{\mathrm{en}}\right|^2 \frac{2}{V} \sum_{\boldsymbol{k}_t} \left|\hat{e} \cdot \boldsymbol{p}_{\mathrm{cv}}\right|^2 \delta(E_{\mathrm{hm}}^{\mathrm{en}} + E_t - \hbar\omega)(f_v^m - f_c^n) \tag{5.48}$$

Use the two-dimensional joint density of states

$$\frac{2}{V}\sum_{\boldsymbol{k}_t}=\frac{2A}{V}\int\frac{d^2\boldsymbol{k_t}}{(2\pi)^2}=\frac{1}{\pi L_z}\int_0^\infty \boldsymbol{k_t}d\boldsymbol{k_t}=\int_0^\infty d\frac{\hbar^2\boldsymbol{k_t}^2}{2m_r^*}\cdot\frac{m_r^*}{\pi\hbar^2L_z}=\int_0^\infty dE_t\rho_r^{2D} \tag{5.49}$$

$$\rho_r^{2D}=\frac{m_r^*}{\pi\hbar^2L_z} \tag{5.50}$$

where A is the area of the cross section, $\mathrm{A}L_z=V$, L_z is an effective period of the quantum wells, and V is a volume of a period. The delta function gives the contribution at $E_{\mathrm{hm}}^{\mathrm{en}}+E_t=\hbar\omega$, and the absorption edges occur at $\hbar\omega=E_{\mathrm{hm}}^{\mathrm{en}}$. For an unpumped semiconductor, $f_v^m=1\ and\ f_c^n=0$, we have the absorption spectrum at thermal equilibrium $\alpha_0(\hbar\omega)$

$$\alpha_0(\hbar\omega)=C_0\sum_{n,m}\left|I_{\mathrm{hm}}^{\mathrm{en}}\right|^2\left|\hat{e}\cdot\boldsymbol{p}_{\mathrm{cv}}\right|^2\rho_r^{2D}H(\hbar\omega-E_{\mathrm{hm}}^{\mathrm{en}}) \tag{5.51}$$

Because the integration of the delta function gives the step function, shown as H or the Heaviside step function, $H(x)=1\ for\ x>0,\ and\ 0\ for\ x<0$. For a symmetric quantum well, we find $I_{\mathrm{hm}}^{\mathrm{en}}=\delta_{\mathrm{nm}}$ using an infinite well model, and the absorption spectrum is

$$\begin{aligned}\alpha_0(\hbar\omega)&=C_0\left|\hat{e}\cdot\boldsymbol{p}_{\mathrm{cv}}\right|^2\frac{m_r^*}{\pi\hbar^2L_z}\\ C_0&=\frac{\pi e^2}{n_r\varepsilon_0cm_0^2\omega}\end{aligned} \tag{5.52}$$

5.4 Interband Absorption and Gain in A Quantum Wire

For quantum wire structure, the confining potential also only changes the nature of wavefuction and the density of the state as in the 2-dimensional case. Also ignore the excitonic effects due to the Coulomb interaction between electrons and holes, then follow the similar procedure in 2-dimensional.

We consider a quantum wire with cross section $a\times b$, and the length of wire is $L_z\gg a,b$.

Within a semiconductor model, the valence band Bloch wave functions can be described by

$$\Psi_v(\boldsymbol{r}) = u_v(\boldsymbol{r})\frac{e^{i\boldsymbol{k_t}\cdot\rho}}{\sqrt{L_z}}g_m(x,y) \tag{5.53}$$

$$g_m(x,y) = \frac{2}{\sqrt{\mathrm{ab}}}\sin(\frac{\mathrm{m}}{a}x)\sin(\frac{\mathrm{n}}{b}y) \tag{5.54}$$

and the conduction band Block wave function as,

$$\Psi_c(\boldsymbol{r}) = u_c(\boldsymbol{r})\frac{e^{i\boldsymbol{k_t}\cdot\rho}}{\sqrt{L_z}}\Phi_n(x,y) \tag{5.55}$$

$$\Phi_n(x,y) = \frac{2}{\sqrt{\mathrm{ab}}}\sin(\frac{m^{'}\pi}{a}x)\sin(\frac{n^{'}\pi}{b}y) \tag{5.56}$$

where

$$E_v^{m^{'}n^{'}} = E_{v0} - \frac{\hbar^2}{2m_h^*}[\left(\frac{m^{'}\pi}{a}\right)^2 + \left(\frac{n^{'}\pi}{b}\right)^2 + \boldsymbol{k_t^2}] \tag{5.57}$$

$$E_c^{\mathrm{mn}}(k_t) = E_{c0} + \frac{\hbar^2}{2m_e^*}[\left(\frac{\mathrm{m}}{a}\right)^2 + \left(\frac{\mathrm{n}}{b}\right)^2 + \boldsymbol{k_t^2}] \tag{5.58}$$

The momentum matrix element $\boldsymbol{p}_{\mathrm{ba}}$ is given by

$$\boldsymbol{p}_{\mathrm{ba}} = \langle\Psi_b|\boldsymbol{p}|\Psi_a\rangle \approx \langle u_c|\boldsymbol{p}|u_v\rangle\,\delta_{k_t,k_t^{'}}\,I_{\mathrm{hm}}^{\mathrm{en}} \tag{5.59}$$

where

$$I_{\mathrm{hm}}^{\mathrm{en}} = \int_{-\infty}^{+\infty}\mathrm{dxdy}\Phi_n^*(x,y)g_m(x,y) \tag{5.60}$$

- This is the overlap integral of the conduction and valence band envelope functions
- **K**-Selection rule applied

Use the one-dimensional joint density of states,

$$\frac{2}{V}\sum_{\boldsymbol{k}_t} = \frac{2L_z}{V}\int\frac{d\boldsymbol{k_t}}{2\pi} = \frac{1}{\pi L_x L_y}\int_0^\infty \frac{\mathbf{1}}{\boldsymbol{k_t}} d\boldsymbol{k_t} = \int_0^\infty dE_t \rho_r^{1D} \tag{5.61}$$

$$\rho_r^{1D} = \sum_{m,n}\frac{(2m_r^*)^{\frac{1}{2}}}{\pi\hbar}\frac{\mathbf{1}}{\sqrt{(\hbar\omega - E_c^{\mathrm{mn}})}} \quad for E > E_c^{\mathrm{mn}} \tag{5.62}$$

$$\rho_r^{1D} = \frac{(m_r^*)^{\frac{3}{2}}}{\pi\hbar m_e^* L_x L_y}\frac{\mathbf{1}}{\sqrt{(\hbar\omega - E_g)}} \tag{5.63}$$

The electron density is given by the occupation of the wire states, and at zero temperature it can be integrated analytically,

$$n = \sum_{m,n}\frac{(2m_r^*)^{\frac{1}{2}}}{\pi\hbar} L_x L_y \sqrt{(F_c - E_c^{\mathrm{mn}})} \tag{5.64}$$

where $L_z L_x L_y = V$, L_x, L_y, L_z are effective period of the quantum wire along different directions, L_z along the axial of the quantum wire, and V is a volume of a period. The delta function gives the contribution at $E_{\mathrm{hm}}^{\mathrm{en}} + E_t = \hbar\omega$, and the absorption edges occur at $\hbar\omega = E_{\mathrm{hm}}^{\mathrm{en}}$. For an unpumped semiconductor, $f_v^m = 1\ and\ f_c^n = 0$, we have the absorption spectrum at thermal equilibrium $\alpha_0(\hbar\omega)$

$$\alpha_0(\hbar\omega) = C_0 \sum_{n,m} |I_{\mathrm{hm}}^{\mathrm{en}}|^2 |\hat{e}\cdot\boldsymbol{p}_{\mathrm{cv}}|^2 \rho_r^{1D} H(\hbar\omega - E_{\mathrm{hm}}^{\mathrm{en}}) \tag{5.65}$$

Because the integration of the delta function gives the step function, shown as H or the Heaviside step function, $H(x) = 1\ for\ x > 0,\ and\ 0\ for\ x < 0$. For a symmetric quantum wire, we find $I_{\mathrm{hm}}^{\mathrm{en}} = \delta_{\mathrm{nm}}$ using an infinite wire model, and the absorption spectrum is

$$\alpha_0(\hbar\omega) = C_0 \left|\hat{e}\cdot\boldsymbol{p}_{\rm cv}\right|^2 \frac{(2m_r^*)^{\frac{1}{2}}}{\pi\omega} L_x L_y \frac{\mathbf{1}}{\sqrt{(\hbar\omega - E_{\rm cv}^{\rm mn})}}$$

$$E_{\rm cv}^{\rm mn} = E_g + \frac{\hbar^2}{2m_r^*}\left[\left(\frac{\rm m}{a}\right)^2 + \left(\frac{\rm n}{b}\right)^2\right]$$

$$C_0 = \frac{\pi e^2}{n_r \varepsilon_0 c m_0^2 \omega} \tag{5.66}$$

5.5 Partial Confinement on the Electron in Conduction Band

If the one-dimensional confinement only apply to the electrons in the conduction band, i.e., the holes in the valance band are free to move as in the bulk semiconductor, the wavefunction in the conduction band and valance band will change accordingly. The overlap of the conduction and valance band envelope function will no longer exist.

Within a two-band model, the Bloch wave functions can be described by

$$\Psi_a(\boldsymbol{r}) = u_v(\boldsymbol{r}) \frac{e^{i\boldsymbol{k_t}\cdot\rho}}{\sqrt{L_z}} \tag{5.67}$$

for a hole wave function in the heavy-hole or a light-hole subband m. and

$$\Psi_b(\boldsymbol{r}) = u_c(\boldsymbol{r}) \frac{e^{i\boldsymbol{k_t}\cdot\rho}}{\sqrt{L_z}} \Phi_n(x,y) \tag{5.68}$$

for an electron in the conduction subband n. The momentum matrix element $\boldsymbol{p}_{\rm ba}$ is given by

$$\boldsymbol{p}_{\rm ba} = \langle\Psi_b|\boldsymbol{p}|\Psi_a\rangle \approx \langle u_c|\boldsymbol{p}|u_v\rangle\, \delta_{k_t,k_t'}\, I_{\rm en} \tag{5.69}$$

where

$$I_{\text{en}} = \int_{-\infty}^{+\infty} \text{dxdy}\Phi_n^*(x,y)$$

$$= \int_{-\infty}^{+\infty} dxdy \cdot const \times e^{-\alpha^2 y^2} \mathcal{H}_{n_1}(\alpha y) sin\frac{\text{x}n_2}{L_x} \tag{5.70}$$

Here introduce the notations

$$\alpha = \frac{m_e^* \omega}{\hbar}\ , \quad \mathcal{H}_n(y) = (-1)^n e^{y^2} \frac{d^n}{dy^n} e^{-y^2} \tag{5.71}$$

where $\mathcal{H}_n$ are the Hermite polynomials[3], n_1 and n_2 are two quantum numbers.

There is no overlap of the conduction and valence band envelope functions and the **K**-Selection rule also applied. The energy levels, which arise in quantum wires, are strongly dependent on the form of the confining potentials. And the additional confinement of electrons leads to an increase of the lowest energy level.

Take into account the quantization of the electron and hole energies E_a and E_b

$$E_a = E_{\text{hm}} - \frac{\hbar^2 \boldsymbol{k_t}^2}{2m_h^*} \tag{5.72}$$

$$E_b = E_g + E_{\text{en}} + \frac{\hbar^2 \boldsymbol{k_t}^2}{2m_e^*} \tag{5.73}$$

And $E_{\text{hm}} < 0$,

$$E_b - E_a = E_{\text{hm}}^{\text{en}} + E_t, E_t = \frac{\hbar^2 \boldsymbol{k_t}^2}{2m_e^*} \tag{5.74}$$

where

$$E_{\mathrm{hm}}^{\mathrm{en}} = E_g + E_{\mathrm{en}} - E_{\mathrm{hm}} \tag{5.75}$$

is the band edge transition energy ($\boldsymbol{k_t} = 0$). The summations over the quantum numbers $\boldsymbol{k}_a$ and $\boldsymbol{k}_b$become summations over $(\boldsymbol{k_t'}, m)$ and $(\boldsymbol{k_t}, n)$. Noting in the matrix element $\boldsymbol{k_t} = \boldsymbol{k_t'}$

$$\alpha\left(\hbar\omega\right) = C_0 \sum_n \left|I_{\mathrm{en}}\right|^2 \frac{2}{V} \sum_{\boldsymbol{k}_t} \left|\hat{e} \cdot \boldsymbol{p}_{\mathrm{cv}}\right|^2 \delta(E_{\mathrm{hm}}^{\mathrm{en}} + E_t - \hbar\omega)(f_v^m - f_c^n) \tag{5.76}$$

Similarly, for this quasi-one dimensional case, assume the one-dimensional joint density of states also apply

$$\frac{2}{V}\sum_{\boldsymbol{k}_t} = \frac{2L_z}{V}\int \frac{d\boldsymbol{k_t}}{2\pi} = \frac{1}{\pi L_x L_y}\int_0^\infty \frac{\mathbf{1}}{\boldsymbol{k_t}} d\boldsymbol{k_t} = \int_0^\infty dE_t \rho_r^{1D} \tag{5.77}$$

$$\rho_r^{1D} = \frac{\left(m_r^*\right)^{\frac{3}{2}}}{m_e^* L_x L_y} \frac{\mathbf{1}}{\sqrt{(\hbar\omega - E_g)}} \tag{5.78}$$

where $L_z L_x L_y = V$, L_x, L_y, L_z are effective period of the quantum wire along different directions, L_z along the axial of the quantum wire, and V is a volume of a period. The delta function gives the contribution at $E_{\mathrm{hm}}^{\mathrm{en}} + E_t = \hbar\omega$, and the absorption edges occur at $\hbar\omega = E_{\mathrm{hm}}^{\mathrm{en}}$. For an unpumped semiconductor, $f_v^m = 1 \; and \; f_c^n = 0$, we have the absorption spectrum at thermal equilibrium $\alpha_0\left(\hbar\omega\right)$

$$\alpha_0\left(\hbar\omega\right) = C_0 \sum_n \left|I_{\mathrm{en}}\right|^2 \left|\hat{e} \cdot \boldsymbol{p}_{\mathrm{cv}}\right|^2 \rho_r^{1D} H(\hbar\omega - E_{\mathrm{hm}}^{\mathrm{en}}) \tag{5.79}$$

Because the integration of the delta function gives the step function, shown as H or the Heaviside step function, $H\left(x\right) = 1 \; for \; x > 0, \; and \; 0 \; for \; x < 0$. The summation of I_{en}becomes the integral of conduction band electron envelope function, using an infinite wire model, and the absorption

spectrum is

$$\alpha_0(\hbar\omega) = C_0 \sum_n |I_{\mathrm{en}}|^2 \left|\hat{e}\cdot\boldsymbol{p}_{\mathrm{cv}}\right|^2 \frac{(m_r^*)^{\frac{3}{2}}}{\pi\hbar} m_e^* L_x L_y \frac{\mathbf{1}}{\sqrt{(\hbar\omega - E_g)}} \tag{5.80}$$

$C_0 = \frac{\pi e^2}{n_r \varepsilon_0 c m_0^2 \omega}$ We can see that the factors containing A_0^2 are canceled because the linear optical absorption coefficient is independent of the optical intensity.

5.6 Upward and Downward Transition Rates

5.7 Contributing Factors

The derived absorption and spontaneous emission rate are both strong function of dimensionality. Carrier confinement in core-shells, and the effect of local forces shown by band bending affects transition rates due to the following factors:

5.7.1 Overlap Integral

Between initial and final wave function, the confined structure altered the envelope functions and furthermore changed the overlap integral as in equation. This overlap of the conduction and velence band will have an effect on the electron transitions under electric field or external perturbation.

Where and are electron envelope function in the conduction subband n and hole envelope function in the heavy-hole or light-hole subband m correspondingly.

5.7.2 Oscillator Strength

The optical matrix element for the electron-to-heavy hole transition induced oscillator strength per unit length can be expressed as;

where is the three-dimensional exciton envelope function. And is the exciton wave function, where and are the ground state wave functions for electrons and heavy holes in the absence of their interaction.

Generally, different dimensionality only alters the envelope function, so if this function is included in the calculation of the oscillator strength, we should expect the oscillator strength is dependent of the dimensionality. To be more specific, the decreasing of dimensionality will raise the oscillator strength. Esaki in paper has mentioned that the exciton oscillator strength per unit volume in the GaAs quantum well nanowire structure is about an order of maginitude larger than in bulk GaAs.

5.7.3 Joint Optical Density of States

As shown in the above derivation, joint optical density of state is a strong function of dimensionality which comes from the summation over wave numbers k, as showin int eh. And as derived in former chapters, the three-dimensional joint optical density of states expresses as and the two-dimensional case and the one-dimensional shown as:

The extremely reduced effective hole mass which mentioned in Coldren's paper, from 0.118 reduced to as in quantum wire structure, may cause by the hole band separation due to the local force or string inside the semiconductor.

As the reduced effective mass plays an important role in joint optical density of states and obtained from electron and hole effective mass is much larger than electron effective mass, the reduced effective mass will have a strong correlation with the hole effective mass as it decreased with the dimensionality decreasing. Thus, the reduced effective mass as it decreased with the dimensionality decreasing. Thus, the reduced effective mass will alter the joint optical density of state in the case of dimensionality changing.

The preceding theory of gain involving Fermi's Golden Rule considers each electron in isolation as it interacts with the electromagnetic field. In other words, we have used a single-particle theory to obtain the gain spectrum. In reality, there is a large density of both electrons and holes present in the system. The mutual interactions between these particles are generally referred to as many-body effects. These effects included lineshape broadening, which is related to collisions between particles and/or phonons in the crystal. In addition to this important effect, there are two other significant consequences of many-body effects: exciton states and bandgap shrinkage. Exciton states

exsit primarily at low carrier densityies and low temperatures, where bandgap shrinkage becomes noticeable at high carrier densities.

Under conditions of low carrier density and low temperature, it is possible for an electron and hole to orbit each othere for an extended period of time, forming what is referred to as an exciton pair. Such exciton pairs have a binding energy associated with them that is euqal to the energy required to separate the electron and hole. As a rsult, electrons that are elevated from the valence band to one of these exciton states will absorb radiation at energies equal to the bandgap less the binding energy (the bandgap will appear to be red-shifted). More significatnly however, the overlap integral (and hence the matrix element) of these two-particle states can be quite large. As a result, band-to-exciton transitions tend to dominate the absorption spectrum. However, exciton states are limited to states near $k = 0$, and hence band-to-exciton transitions are clustered at the band edge (or subbabdn edge). The overall effect is the qppearance of very strong absorption peaks near the subband edges in quantum-well materials, and near the band edge in bulk material.

Exciton absorption peaks are clearly visible in quantum wells at room temperature for a typical GaAs QW. The first two steps in the "staircase" absorption spectrum predicted from the density of states. However, the exciton peaks riding on top of the steps, particularly the n = 1 peaks, dominate the absorption spectrum. Each observed exciton peak corresponds to one of the subband transitions.

The second many-body effect occurs at high carrier densities, where the charges actually screen out the atomic attactive forces. With a weaker effective atomic potential, the single-atom electron wavefunctions of interest become less localized and the nearest-neighbor electron everlap becomes higher. The large overlap increases the width of the energy bands (δE is larger), reducing the gap between bands. Although this description is only qualitative, it does reveal that the bandgap should shrink with increasing carrier density.

It can also be argued theoretically that the badgap shrinkage is inversely related to the average spacing between carriers, or (the closer the carriers are, the more their own Coulomb potentials screen out the atomic potential). In bulk material, the average volume occupied by one carrier is

inversely related to the carrier density.

The net effect of bandgap shrinkage is that as carrier density increases, the entire gain spectrum redshifts by a noticeable amount. In principle, the shift is accompanied by a slight distortion. (i.e, reshaping and enhancement) of the spectrum.

With decreasing dimensionality of the active region of an injection laser, the density of states and gain spectra become narrower, which leads to a decrease in the number of states to be filled to make the active region transparent (zero population inversion and zero gain) and to achive lasing (gain equal to loss) Consequently, the transparency current (or inversion current) at which the gain is equal to the loss and lasing begins decrease and their temperature dependences become weaker [42].

Figure 8 (C) shows the FDTD-simulated electric field density of a hexagonal nanowire at y cross section (top) and x cross section (bottom). The photon energy of this mode shown as the insets of Fig. 8(C) is concentrated primarily along the 6 corners and secondarily along the facets with little light in the 3D core of GaAs. Hence, we suggest that the fortuitous spatial overlap of the resonant optical modes on reduced dimensional electronic wavefunctions plays a significant role in the remarkable optoelectronic properties of core-shell nanowires. Restated, the superposition of the photon modes on reduced electronic states that form on the facets and vortices of the hexagonal CSNWs strongly enhances both upward and downward transition rates. Thus, the reduced dimensionality transition rate distinguishes the core-shell nanostructure from the optically equivalent structures of Fig. 6 due to its significantly modified rate management. These nanostructures are not only excellent optical cavities, but despite their large size also provide the right reduced dimensional electronic structures which enhance optoelectronic interactions. It should be noted the present analysis is for direct optical transitions; although it can be extended to incorporate k-vector changes as in phonon scattering, other important factors such as many-body interactions need to be included in a

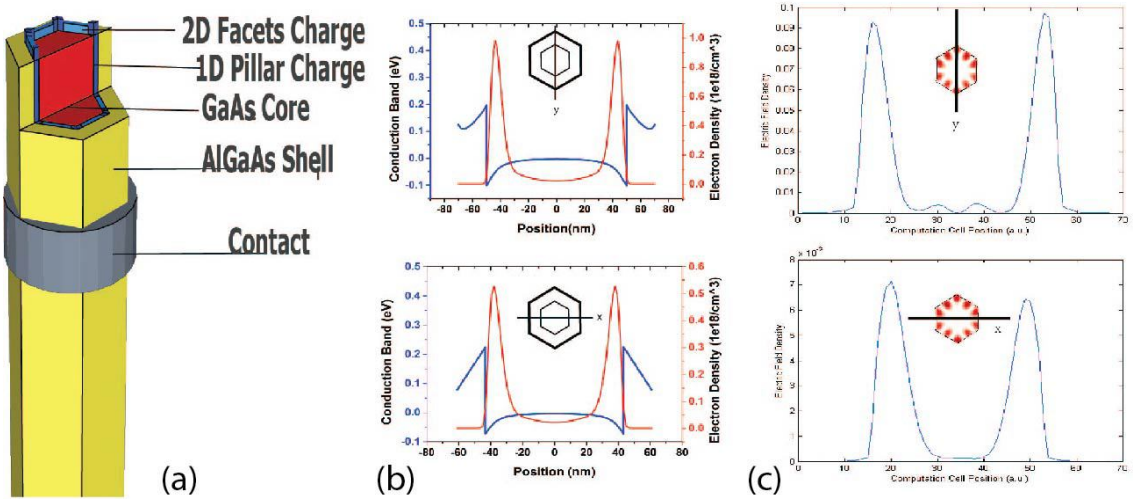

Figure 5.1 Photon Charge Distribution

CHAPTER 6

MODELING LASING THRESHOLD

6.1 History of Semiconductor Lasers

As we know, semiconductor lasers are important optoelectric devices ofr optical communication systems. They are essential components for building optical communication systems. There are intensive research results and achievements from beginning. In 1917, Einstein predicted the existence of spontaneous and stimulated emission by which an atom can emit radiation. The first semiconductor lasers were fabricated in 1962 using homojuncations. These lasers had high threshold current density (19000/A/cm2) and operated at cryogenic temperatures. The concept of heterojuntion semiconductor lasers was realized in 1969 1970 with a low threshold current density (1600 A/cm2) operating at room temperature. These double-heterostructure diode lasers provide both carrier and optical confinements, which imporve the efficiency for stimulated emission. The concept of quantum well structures for semicondcutor lasers was proposed and realized experimentally in the late 1970s. The threshold current density was reduced to about 500 A/cm, which improved the laser performance significantly.

6.2 Principle of Semiconductor Lasers

As we know, the semiconductor laser (or laser diode) in its simplest form is a p-n junction of a single crystal of semiconductor material arranged in a cavity, as shown in . The type and configuration of the material used to determine the optical characteristics of the laser diode emission. Like others in various oscillators or wave sources, the fundamental elements in the semiconductor lasers are

the following three elements: semiconductor band structure (population inversion to provide gain mechanism), current injection and P-N junction (external pumping to make gain sustainable) and reflector of cavity (feedback to provide coherence). The most common semiconductor lasers are including Fabry-Perot(FP) or distributed feedback (DFB)/distributed Bragg reflector (DBR)

6.2.1 Absorption of Light

The light and matter interaction includes absorption, spontaneous emission and stimulated emission, we first discuss the absorption of light by introducing the absorption coeffiecient. This is the absorption rate without considering the occupation factors.

Based on the following equations for different dimensionality.

$$\begin{aligned} \alpha_{3D}(\hbar\omega) =& C_0|\hat{e}\cdot\mathbf{p_{cv}}|^{\mathbf{2}}(f_v - f_c) \\ & \frac{1}{2\pi^2}(\frac{2m_r^*}{\hbar^2})^{3/2}(\hbar\omega - E_g)^{1/2}, \\ & C_0 = \frac{\pi e^2}{n_r\epsilon_0 c m_0^2\omega}, \end{aligned} \tag{6.1}$$

$$\begin{aligned} \alpha_{2D}(\hbar\omega) &= C_0|\hat{e}\cdot\mathbf{p_{cv}}|^{\mathbf{2}}\frac{m_r^*}{\pi\hbar^2 L_z}, \\ \alpha_{1D}(\hbar\omega) &= C_0|\hat{e}\cdot\mathbf{p_{cv}}|^{\mathbf{2}}\frac{(m_r^*)^{3/2}}{\pi\hbar m_e^* L_x L_y}\frac{1}{\sqrt{(\hbar\omega - E_g)}}, \end{aligned} \tag{6.2}$$

The split plots of absorption coefficient for different dimensionality as in Fig. 6.1. Noted the unique shapes of density of states.

Then the overlay plot with multiple y axis as in Fig. 6.2 and the different scales indicating the enhancement factor for 1D is 35(need to be verified) compared to 3D.

6.2.2 Optical Gain

Following the treatments of Appendix 3, we can derive the gain spectrum for 3D, 2D and 1D with consideration of occupation factor by calculating the Fermi levels.

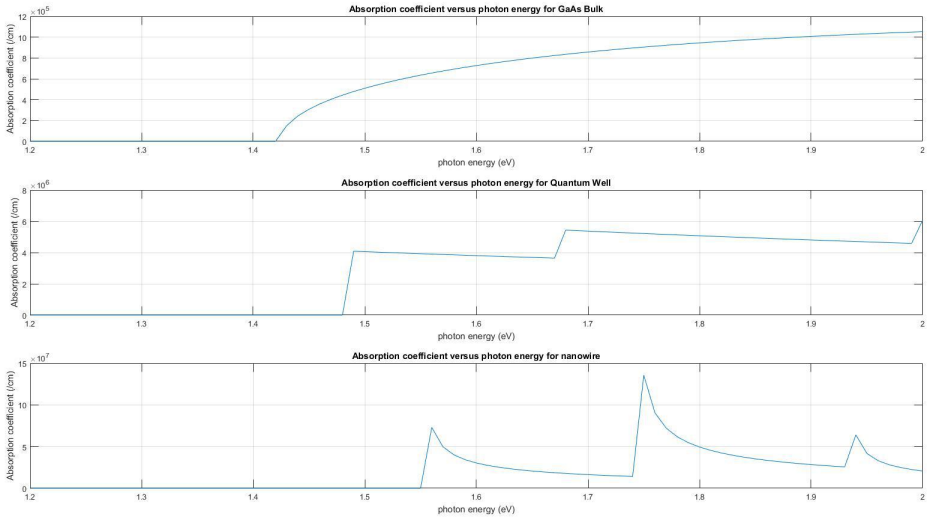

Figure 6.1 Absorption Coefficient versus Photon Energy for 1D 2D and 3D with split plot

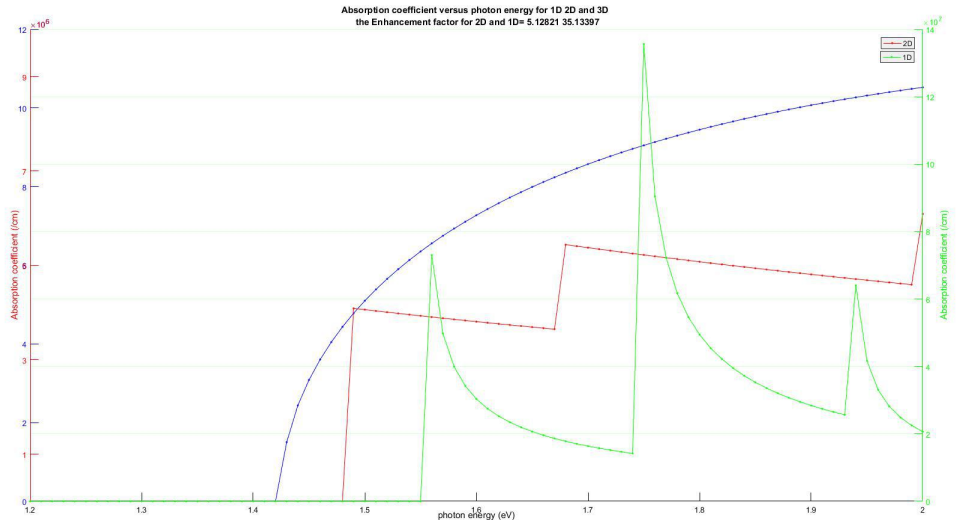

Figure 6.2 Absorption Coefficient versus Photon Energy for 1D 2D and 3D

Table 6.1. Parameters for rate euqation analysis.

Parameters	Values and Units
A	$1.43 \times 10^{8}\ s^{-1}$
τ_{sp}	4 ns
C	$3.5 \times 10^{-30}\ cm^{6} - s$
n_g	4.2
Γ	1

Note. — This table is available in its entirety in a machine-readable form in the journal publication **?**. A portion is shown here for guidance regarding its form and content.

With decreasing dimensionality of the active region of an injection laser, the density of states and gain spectra become narrower, which leads to a decrease in the number of states to be filled to make the active region transparent (zero population inversion and zero gain) and to achieve lasing (gain equal to loss). Consequently, the transparency current (or inversion current, i.e., the injection current at which the population inversion is zero) and the threshold current (injection current at which the gain is equal to the loss and lasing begins) decrease and their temperature dependences become weaker. The decrease in the threshold current and increase in its temperature stability reflect one fo the main areas of development and improvement of injection lasers. Owing to the continuous nature of the carrier spectrum within the allowed subbands, the use of QWs or QURs as active medium for optical transitions can only quantitatively improve the parameters of devices based on them compared with devices with a bulk active region.

Among the advantages of QD lasers over the presently used QW lasers are their narrower gain spectra, much lower threshold currents, and ultrahigh temperature stability, as well as the wider possibilities for controlling their lasing wavelength.

All the parameters for rate quations analysis in table 6.1.

$$
\begin{aligned}
g_{3D}(\xi) &= \frac{\sqrt{2}e^2 {m_r^*}^{3/2} p_{cv}^2}{3\pi n_r \epsilon_0 {m_0}^2 C\hbar^2 \xi}\sqrt{(\xi-\xi_g)}(f_n(\xi_2)-f_p(\xi_1)),\\
g_{2D}(\xi) &= \frac{e^2 m_r^* p_{cv}^2}{3n_r \epsilon_0 {m_0}^2 C\hbar L_z \xi}(f_n(\xi_2)-f_p(\xi_1)),\\
g_{1D}(\xi) &= \frac{e^2 {m_r^*}^{3/2} p_{cv}^2}{3n_r \epsilon_0 {m_0}^2 C\xi L_x L_y}\frac{1}{\sqrt{(\xi-\xi_g)}}(f_n(\xi_2)-f_p(\xi_1)),
\end{aligned}
\tag{6.3}
$$

Now we can plot the gain spectrum respect to photon energy for 3D, 2D and 1D in the figure below. As we can see, the gain spectrums follow the unique shapes of density of states. The fourth figure is the maximum gain versus electron carrier concentration varing from $3\times10^{18}(cm^{-3})$ to $3\times10^{19}(cm^{-3})$. Using parameters $N_{tr} = 2\times10^{18}cm^{-3}$, $N_s = 4\times10^{18}cm^{-3}$, and $g_0 = 6.11\times10^5 cm^{-1}$, we fit the curve in Fig. 6.3 to build a logarithmic gain model of the form for 3D case:

$$
g(N) = g_0 \ln\left(\frac{N+N_s}{N_{tr}+N_s}\right) \tag{6.4}
$$

where N_s is a shift to force the natural logrithm to be finite at $N=0$ such that the gain equals the umpumped absorption due to the band-to-band transitions, N_{tr} is the transparency carrier density, and g_0 is the gain coefficient. N_{tr} and g_0 will be different for different dimensionality.

After fitting the curve in Fig. 6.4, we can calculate the threshold carrier density is $N_{th} = 4.533\times10^{18}cm^{-3}$. Then plotting the spontaneous emission rate with respect to the threshold carrier density N_{th} for 3D, 2D and 1D as following:

$$
\begin{aligned}
r_{3D}^{\text{spon}}(\xi) &= \frac{n_r e^2 \xi p_{cv}^2}{\pi\epsilon_0 {m_0}^2 C^3\hbar^2}\frac{{m_r^*}^{3/2}}{2\pi^2\hbar^3}\sqrt{(\xi-\xi_g)}f_n(\xi_2)(1-f_p(\xi_1)),\\
r_{2D}^{\text{spon}}(\xi) &= \frac{n_r e^2 \xi p_{cv}^2}{\pi\epsilon_0 {m_0}^2 C^3\hbar^2}\frac{m_r^*}{\pi\hbar^2 L_z}f_n(\xi_2)(1-f_p(\xi_1)),\\
r_{1D}^{\text{spon}}(\xi) &= \frac{n_r e^2 \xi p_{cv}^2}{\pi\epsilon_0 {m_0}^2 C^3\hbar^2}\frac{{m_r^*}^{3/2}}{\pi\hbar m_e^* L_x L_y}\frac{1}{\sqrt{(\xi-\xi_g)}}f_n(\xi_2)(1-f_p(\xi_1)),
\end{aligned}
\tag{6.5}
$$

Integraing over all the photn energy spectrum, we have $R_{sp} = \int_\xi r_{sp} d\xi$ for different dimensionality,

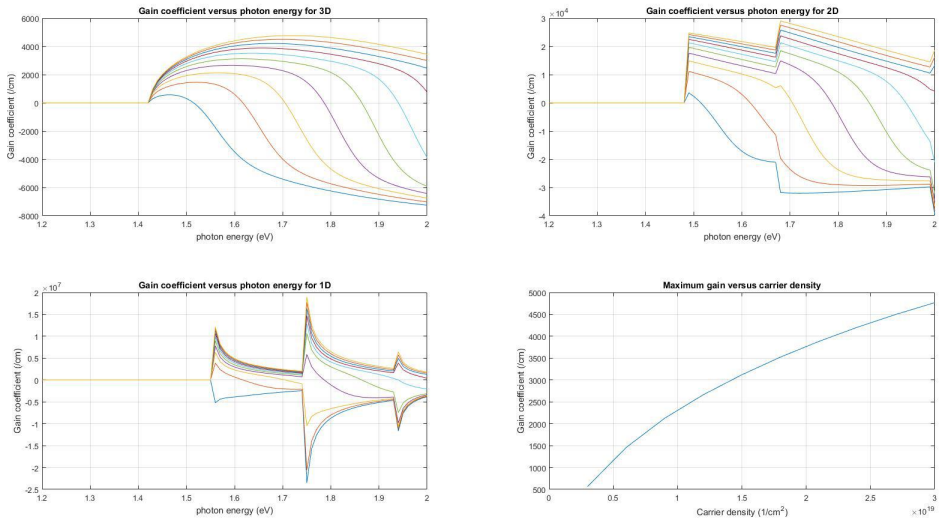

Figure 6.3 Gain Coefficient versus Photon Energy for 1D 2D and 3D

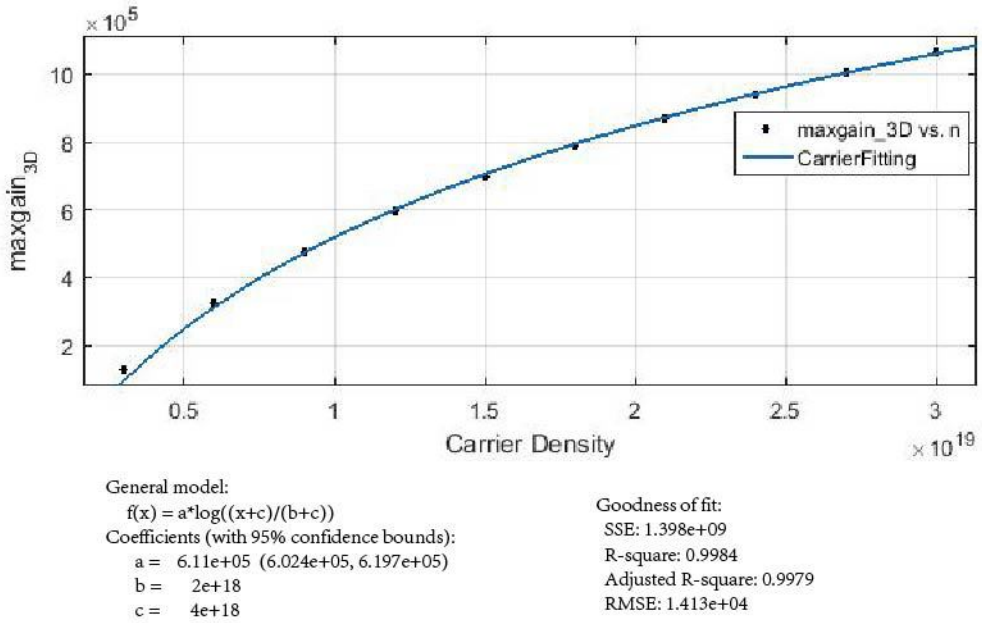

Figure 6.4 Gain Model Fitting

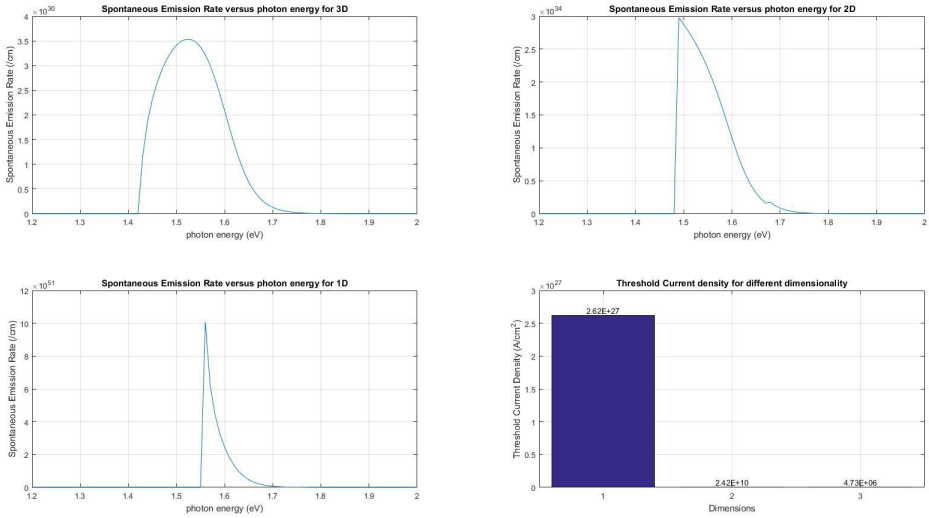

Figure 6.5 Spontaneous Emission Rate versus Photon Energy for 1D 2D and 3D

then the threshold current density can be simply caluclated as: $J_{th} = qdR_{sp}|_{N_{th}}$ and plotted in the fourth part of Fig. 6.5. The threshold current for 3D is $2.62\times10^{27}(A/cm^2)$, 2D is $2.42\times10^{10}(A/cm^2)$, and 1D case is $4.73 \times 10^6(A/cm^2)$. The threshold current density needed for lower-dimensional structure is greatly reduced.

Next, we can do dynamic analysis of laser modal and replace the threshold current density to threshold pumping power. And verify the result with the experimental data.

6.2.3 Feedback and Laser Threshold

6.3 Types of semiconductor Lasers

6.3.1 Fabry-Perot Semiconductor Lasers

The Fabry-Perot(FP) laser is conceptually just an LED with a pair of end mirrors or facets. The mirrors are needed to create the right conditions for lasing to occur. The lasing medium can only amplify (undergo stimulated emission) over a fairly narrow range because of the characteristics of the material it is made from . A typical gain curve is illustrated on the left-hand.

6.3.2 Grating-Based semiconductor Lasers

6.3.3 Vertical-Cavity Surface-Emitting Lasers

As seen, light in the VCSEL propagates vertically with DBR mirrors as the nature of the manufacturing process, the entire round-trip of the VCSEL is much shorter than that of with the edge-emitting lasers. It leads to high reflectivity (around 99.9%) of DBR mirrors, in which the large number of layers are required.

One of features related to the VCSELs is the longitudianl modal stability due to its short cavity length (around order of the wavelength). A

6.3.4 Grating Surface-Emitting Lasers

6.4 Characteristics of Semiconductor Lasers

In order to understand their operation, it is necessary to know some basic performance parameters or important features of semiconductor lasers.

6.5 Basic Requrement for Design of Semiconductor Lasers

6.5.1 Spectral width and Linewidth

FP semiconductor lasers produce a range of wavelengths. This range of wavelengths is called the "spectral width" of the laser. Typically there will be around 8 "modes" and the spectral width. In order to determin exactly the spectral shape, spectral width is usually quoted as the FWHM (Full Width Half Maximun) Instead of producing a continuous range of wavelengths over their spectral width. Semiconductor lasers produce a series of "lines" at a number of discrete wavelengths. Lines themselves vary in width (in different types of lasers) very significantly. The linewidth is inversely proportional to the coherence length of the laser.

6.5.2 Operating Wavelength, Switching Time, and Modulation

6.6 Modeling of Semiconductor Lasers

From the general formulations through the rate equations ans wave equations based on the

As we know, from different aspects of the same physics of the energy conservation, there are two basic classical methods to model the operation of semiconductor lasers. The first method, which will be summarized , applies the concept of photo/electron particle exchange with the abtract optical parameters and is suitable for the FP lasers. For the DBR/DFB lasers, due to strong non-uniformities of index distribution. The interaction between electromagnetic fields and electric particles has been considered, which . Indeed, those two methods are wholly compatible with one anohter. In this project, because we focus on the FP lasers as , we employ the first method: the standard rate equation approach.

Three fundamental elements in the semiconductor lasers: semiconductor band structure, current injection, and cavity. The former two are related to the material and junction structure and the later is related to the laser structure. For semiconductor lasers, the key in the modeling is to deal with the interaction between electromagnetic fields and gain medium. The basic procedure of modeling of semiconductor lasers: Due to the complexity of the rate equation and coupling between carrier and photon density, the coupling rate equations are further solved by numerical methods such as the standing-wave approach (in frequency domain) and the traveling-wave approach (in time domain). The stading-wave approach is based on the assumption that the temporal and the spatial dependence of field distributions of the cavity odes are separable. As such, the dynamics is considered in the modal amplitudes. Consequently, the standing-wave apporach is valid only when the photon lifetime is much shorter than the characteristic time of the laser dynamics. The traveling-wave approach, on the other hand, makes no assumptions about the cavity modes. Rather, it solves the time-dependent coupled=wave equations for the forward and the backward traveling waves directly and tehrefore is valid even the laser cavity has relatively small Q-factor and/or the characteristic time of the laser dynamics is very short. Another advantage of the traveling-wave model is that it can be readily

applied to laser diodes operated with multiple cavity modes, for which the stading-wave model may have difficulty in finding the complex roots corresponding to each mode.

6.7 Laser Rate Equations

We start with the governing equations of carrier density and photon density in the active region which is governed by a dynamic process.

$$\begin{aligned} \frac{dN}{dt} &= \frac{\eta_i I}{qV} - \frac{N}{\tau} - R_{st}, \\ \frac{dN_p}{dt} &= \Gamma v_g g N_p + \Gamma \beta_{sp} R_{sp} - \frac{N_p}{\tau_p}, \end{aligned} \tag{6.6}$$

where β_{sp} is the spontaneous emission factor, defined as the percentage of the total spontaneous emission coupled into the lasing mode. And it is just the reciprocal of the number of available optical modes in the bandwidth of the spontaneous emission for uniform coupling to all modes. The g is Incremental gain per unit length.

The first term of equation 1 is the rate of injected electrons $G_{gen} = \Gamma_i I/qV$, $\Gamma_i I/q$ is the number of electrons per second being injected into the active region, where V is the volume of the active region. The rest terms are the rate of recombining of electrons per unit volume in the active region. There are several mechanisms should be considered, including a spontaneous recombination rate, R_{sp}, a nonradiative recombination rate, R_{nr}, a carrier leakage rate, R_l and a net stimulated recombination, R_{st}, including both stimulated absorption and emission. Which looks like:

$$R_{rec} = R_{sp} + R_{nr} + R_l + R_{st} \tag{6.7}$$

The above equation used input current intensity, I, for electrically injected lasing situation, however, if optical pump used as the lasing source, then we need to rewrite the governing equations.

$$\begin{aligned}\frac{dN}{dt} &= \frac{\eta_i P}{qV} - \frac{N}{\tau} - R_{st}, \\ \frac{dN_p}{dt} &= \Gamma v_g g N_p + \Gamma \beta_{sp} R_{sp} - \frac{N_p}{\tau_p},\end{aligned} \tag{6.8}$$

P is the optical pump used for exciting nano-cavity laser emission and is time-dependent of the form $P_p sech^2(\frac{1.76t}{\delta t})$, where P_p is the peak power amplitude, and δt is the time pulse width.

The cavity loss can be characterized by a photon decay constant or lifetime, τ_p, and the gain necessary to overcome losses, and thus reach threshold. By assuming steady-state conditions (i.e. $dN_p/dt = 0$), and solving for this steady-state or threshold gain, g_{th}, where the generation term equals the recombination term for photons. We assume only a small fraction of the spontaneous emission is coupled into the mode (i.e. β_{sp} is quite small), then the second term can be neglected, and we have the solution:

$$\Gamma g_{th} = \frac{1}{v_g \tau_p} = < \alpha_i > + \alpha_m \tag{6.9}$$

The product, Γg_{th}, is referred to as the threshold modal gain because it now represents the net gain required for the mode as a whole, and it is the mode as a whole that experiences the cavity loss. $< \alpha_i >$ is the average internal loss, and α_m is the mirror loss if we considered an in-plane wave laser.

$$R_{rec} = R_{sp} + R_{nr} + R_l + R_{st} \tag{6.10}$$

The first three terms on the right refer to the natural or unstimulated carrier decay processes. The fourth one, R_{st}, require the presence of photon.

Then, recognizing that $(R_{sp} + R_{nr} + R_l) = AN + BN^2 + CN^3$ depends monotonically on N, we observe from eq 2.34 that above threshold $(R_{sp} + R_{nr} + R_l)$ will also clamp at its threshold value, given by Eq 2.35. Thus, we can substitute Eq 2.35 into the carrier rate equation, eq 2.16 to obtain

a new above threshold carrier rate equations,

$$\frac{dN}{dt} = \eta_i \frac{(I - I_{th})}{qV} - v_g g N_p, \quad (I > I_{th}) \tag{6.11}$$

We also calculate a steady-state photon density above threshold where $g = g_{th}$,

$$N_p = \frac{\eta_i (I - I_{th})}{q v_g g th V} \quad (steady\ state) \tag{6.12}$$

To obtain the power out, we first construct the stored optical energy in the cavity, E_{os}, by multiplying the photon density, N_p, by the energy per photon, hv, and the cavity volume, V_p. That is $E_{os} = N_p hv V_p$. Then, we multiply this by the erngy loss rate through the mirrors, $v_g \alpha_m = \frac{1}{\tau_m}$, to get the optical power output from the mirrors,

$$P_0 = v_g \alpha_m N_p hv V_p \tag{6.13}$$

Substituting from , and using $\Gamma = V/V_p$,

$$P_0 = \eta_i (\frac{\alpha_m}{< \alpha_i > + \alpha_m}) \frac{hv}{q} (I - Ith), \quad (I > I_{th}) \tag{6.14}$$

We can get the threshold carrier density

$$N_{th} = N_{tr} e^{g_{th}/g_0 N} = N_{tr} e^{(<\alpha_i> + \alpha_m)/\Gamma g_0 N} \tag{6.15}$$

Using the polynomial fit for the recombination rates, and recognizing that for the best laser material the recombination at threshold is dominated by spontaneous recombination, we have, $I_{th} \cong$

$BN_{th}{}^2 qV/\eta_i$, Thus

$$I_{th} \cong \frac{qVBN_{tr}{}^2}{\eta_i} e^{(<\alpha_i>+\alpha_m)/\Gamma g_0 N} \tag{6.16}$$

where for most $III-V$ materials the bimolecular recombination coefficient, $B \sim 10^{-10} cm^3/s$.

Reduce the transparency value and increase the differential gain of the active materials.

It is desirable to reduce the cavity loss ($< \alpha_i > + \alpha_m$) and volume, V, in order to retaining a reasonably large confinement factor, Γ.

6.8 Wave Model of Semiconductor Lasers

6.9 Linewidth Enhancement Factor

Electrons and holes frequently interact with other carriers and with phonons, thereby changing their energy within the sub-band. Such intra-band scatter events happen about every 0.1 ps, much more often than band-to-band recombination events. Thus, scattering leads to an uncertainty of the electron energy, which can be accounted for by introducing a symmetrical linewidth broadening funtion L into the gain formula. This convolution integral means that gain at the photon energy can now receive contributions from electron transitions with, weighted by

In fact, positive gain is now possible even for photon energies slightly below the bandgap. Cauchy himself exploited such a density function in 1827, with infinitesimal scale parameter, in defining a Dirac delta function, while among physicists, it is known as the Lorentzian line shape functionL with the half-width. This function is based on the assumption that the occupation probability of an electron state decays proportionally to exp(-t/). The Fourier transformation of this exponential function into the nergy domain leads to . Gamma is the average of the broadening in the conduction and inthe valence band. The full linewidth 2gamma is related to the average intra-band scattering time

Which includes scattering events in the conduction band and valence band. For each band, linewidth

contributions from different scattering processes are adding up.

6.10 Implementations

6.10.1 Optical Modes

6.10.2 Steady State Analysis

6.10.3 Dynamic State Analysis

6.11 Simulation Results

6.11.1 Input Parameters

6.11.2 Optical Modes

6.11.3 Steady State Analysis

6.11.4 Dynamic State Analysis

CHAPTER 7

CONCLUSIONS AND FUTURE RESEARCH

As mentioned previously, communication of information, together with storage and computation form a grand challenge of the information age [2, 7]. Recently, the analysis of big data has become the engine for societal, financial, scientific, and technological endeavors. This demands an infrastructure that is capable of fast and reliable high volume data processing. Traditionally, this requirement was fulfilled by silicon technology. However, silicon-based technology has its own limitations, such as speed limit and heat dissipation problem. In order to process high volume data, we need data computation, storage and communication work as three fundamental functions of a computation cell. A monolithic nano-system may be envisioned which incorporates NWs as waveguides, detectors, photovoltaic cells, antennas, modulators, (photo)capacitors, LEDs, and lasers, .These components may be incorporated in circuit layers, such as network on chip. Different layers can communicate using NW through-silicon vias (TSVs). Similar low-power/high-performance advantages can be realized through achievement of high interconnect densities on the 2.5D Though-Si-Interposer (TSI) as reported in [114].

In conclusion, optical properties of nano-cavities were reviewed here emphasizing the analysis of resonant optical modes which depend both radially and axially on the geometries of the nanowires. This shows how such sub-wavelength structures can form optical cavities as-grown, without needing sophisticated facet mirrors. In addition, we show how the fortuitous overlap of the reduced dimensional electronic wave functions and the photonic modes is responsible for the extraordinary optoelectronic properties of core-shell nanowires. Such nano-structures have been developed on het-

erogeneous substrates, particularly silicon, and as such becoming an important component in the next generation of photonic integrated circuits which are particularly useful in meeting the grand challenge of low energy and fast speed computation.

7.1 Contributions of this dissertation

In this dissertation, we simulated the two-dimensional-electron-gas based heterostructure . and compared it with undoped structure. The static behavior simulations, including 2-D potential profile, electric field distributions, and carrier concentration, were performed with commercially availabe software. The carrier transient behaviro in the absorption region was investigated by . The simulation revealed the vertical field in the absortpion region enhanced the elctron transport.

We showed that two-dimenisonal gas can work as an extended contact to collect photogenerated carriers by means of carrier-carrier scattering which results in a fast energy relaxation time.

In addition, we designed a 2DEG/@DHg structure based high-speed photodetector on GaAs substrate for optical communication applictions. It takes the advantages of both vertical field and confined 2D gas, and transforms a lateral MSM structure.

The major contributions of this thesis are (1) simulation and analysis the 2DEG device, revealing a vertical field in the absorption region which facilitates electron transportl; (2) design, simulation and analysis of 2DEG based MSM phototedtector.

7.2 Outline of the future work

Low dimensional electron gases exsit at the heterointerfaces of core-shell nanowires (CSNWs). For example, the GaAs/AlGaAs CSNWs typically form a hexagonal structure in which six (6) pillars of 1D charge at the vortices, and six (6) sheets of 2D charge at facets are formed [43]. At the same time, nanowires (NW) have also been shown to be capable of confining light in their sub-wavelength nanostructure, supporting photonic modes, and producing resonant cavities without the need for polished end facets. We have previously shown how the electronic wave functions that are thus formed affect

the optical transition rates, resulting in orders of magnitude enhancement in absorption and emission of light. Here we report on the plasmonic effects of the confined charge on the optical properties of CSNWs We report on finite difference time domain (FDTD) simulations with the aim of identifying the surface plasmon resonance modes which affect light confinement in hexagonal CSNWs, and help form a high quality factor resonant cavity. This is done by comparing regular CSNW, with a) wires covered with metal which produces surface plasmon-polaritons (SPP); b) NWs covered with metal that is sandwiched between the core and the outer, shell; and c) two-dimensional electron gas (2DEG) which embedded at the heterointerace of CSNWs. Results show that the 2DEG behaves similarly to an embedded metallic surface, allowing for highly localized light confinement in these wires without the need for vertical structures such as Bragg mirrors commonly used in vertical cavity surface emitting lasers (VCSELs). Besides affecting the cavity, the 2DEG enhances the transition rates due to the plasmon-electron interaction, facilitating not only photonic stimulated emission and lasing, but also surface plasmon amplification by stimulated emission of radiation[44].

We model the dielectric function of the two dimensional electron gas using the Drude model for dispersive media, and extract its relevant parameters from[44]. The complex conductivity of the 2DEG is derived using the relaxation time approximation, effective reduced mass of electrons, and the density of the carriers in the gas. By substitution the complex conductivity in Drude model, we can model the 2DEG, with given plasma frequency, damping coefficient, and the oscillator strength using FDTD simulator.

The two dimensional plasma frequency is calculated as[44]: in which, is the background dielectric constant and m* is the effective mass of the electron. It is important to note that, as shown in (1), the plasma frequency of the 2DEG can be tuned with changing the carrier concentration. This tubnability distinguishes the 2DEG from other plasmonic material such as metals. The complex conductivity of the electron gas is derived as[44]:

The electromagnetic wave traveling of the Surface Plamon Polariton (SPP) involves both charge motion in electron reservoir (e.g., metal, graphene and 2DEG) and waves in the dielectric or air.

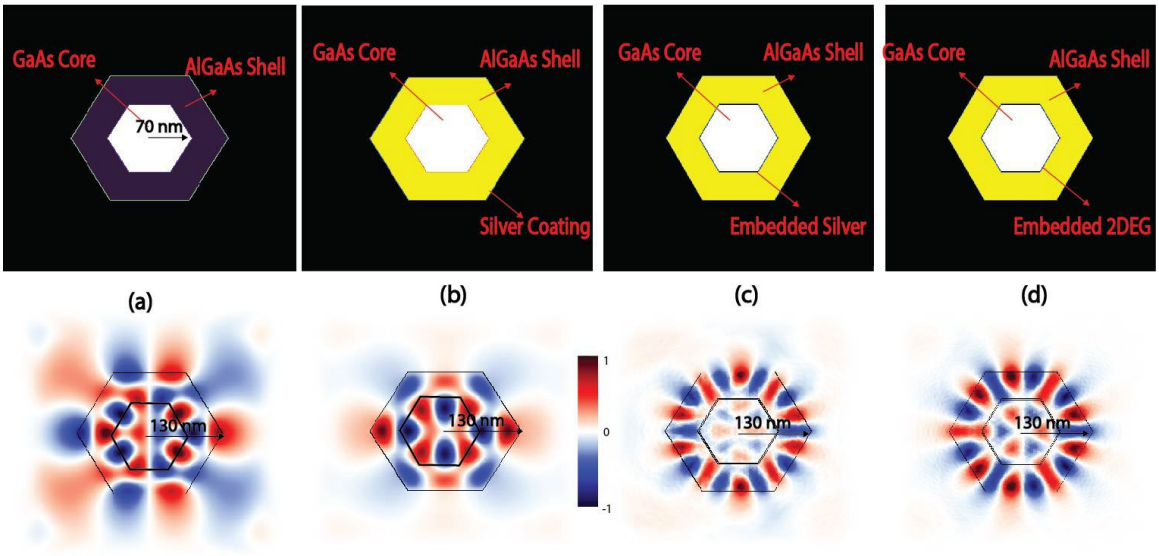

Figure 7.1 An FDTD-simulated electric field profile (linear scale) of (a) a hexagonal core-shell nanowire (CSNW), (b) photonic modes are affected by plamonic modes in a CSNW covered with silver coating, (c) CSNW with embedded silver layer between the core and the shell; (d) plasmonic and photonic modes of CSNW with embedded 2DEG show similar effects compared to embedded metal. The black boundaries represent the interface betweeen layers of the structure.

Instead of using any metallic materials, Core-Shell nanowires (CSNWs) can naturally form two-dimensional electron gas (2DEG) at the heterojunction interface and even large one-dimensional pillar of charge at the corners of thier hexagonal facets.

Surface plasmon polaritons are density oscillations of electrons at the surface of a dielectric. Noble metals such as Au and Ag are considereed as the best plasmonic material candidates because of their high conductivity and low loss. The important parameters fro choosing the metals in plasmonic nanowire are the relaxation time and the plasma frequency of the metallic layer. Since silver has the smallest relaxation time, we coat a CSNW with it in order to study its effect on the NW cavity. we futhre embed Ag between the GaAs core and AlGaAs shell and compare its affect on the field profile and mode generation. Finally, we compare this configuration with a relatively dense 2DEG which is formed at the heterointerface of CSNWs. Simulation is performed using MIT's MEEP open source finite-differnce time-domain (FDTD) simulation software. For modeling the 2DEG we use data in , and for metallic layers, we used Lorentz-Drude model based on experimental data extracted from.

Figure 7.1 shows the FDTD-simulated electric field profile (linear scale) in the transverse plane of (a) CSNW; (b) CSNW with silver coating; (c) CSNW with and embedded silver layer between the core and the shell; (d) CSNW with 2DEG at the hetero-interface. As shown in Fig, coating the wire with metal introduces plasmonic modes in the structure that enhance light confinement. Metal embedded betweeen the core and the shell has similar effect. Importantly, we observe that similar plasmonic features can be obtained due to the 2DEG that is embedded in CSNW[45].

Recently, the analysis of big data has become the engine for societal, financial, scientific, and technological endeavors. This demands an infrastructure that is capable of fast and reliable high volume data processing. Traditionally, this requirement was fulfilled by silicon technology. However, silicon-based technology has its own limitations, such as speed limit and heat dissipation problem. In order to process high volume data, we need data computation, storage, and communication to work in concert as the three fundamental functions of a computation cell. As schematically shown in Fig. 7.2, a monolithic nanosystem may be envisioned, which incorporates NWs as waveguides, detectors, photovoltaic cells, antennas, modulators, (photo)capacitors, LEDs and lasers. These components may be incorporated in circuit layers, such as network-on-chip. Different layers can communicate using NW through-silicon vias (TSVs). Similar low-power/high-performance advantags can be realized through achievement of high interconnect densities on the 2.5D through-Si-interposer (TSI) as reported in reference[46]

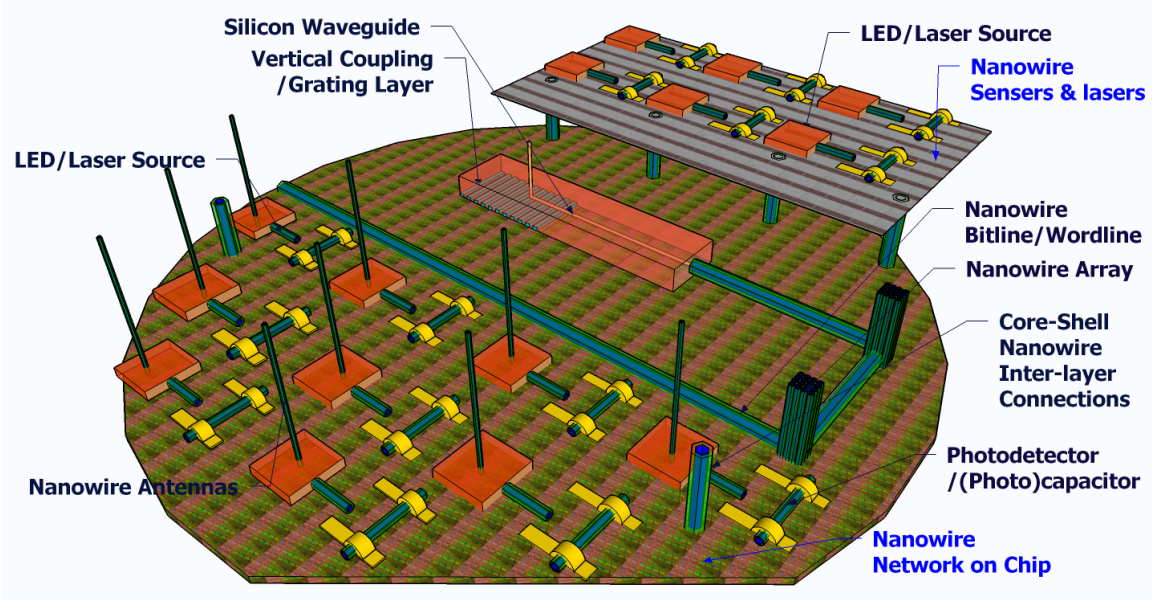

Figure 7.2 Schematic depiction of an optoelectronic nanosystem may include key components such as NW LED/laser source, photodetector/photocapacitor, NW antennas, and NW-enabled network-on-chip integrated on silicon.

BIBLIOGRAPHY

[1] T. Nobis and M. Grundmann, "Low-order optical whispering-gallery modes in hexagonal nanocavities," *Physical Review A*, vol. 72, no. 6, p. 063806, 2005.

[2] R. Chen, T. T. D. Tran, K. W. Ng, W. S. Ko, L. C. Chuang, F. G. Sedgwick, and C. Chang-Hasnain, "Nanolasers grown on silicon," *Nature Photonics*, vol. 5, no. 3, pp. 170–175, 2011.

[3] S. Sun, Z. Fan, Y. Wang, and J. Haliburton, "Organic solar cell optimizations," *Journal of materials science*, vol. 40, no. 6, pp. 1429–1443, 2005.

[4] J. Perlin, *From space to earth: the story of solar electricity.* Earthscan, 1999.

[5] M. Razeghi and A. Rogalski, "Semiconductor ultraviolet detectors," *Journal of Applied Physics*, vol. 79, no. 10, pp. 7433–7473, 1996.

[6] A. Rogalski, "Infrared detectors: an overview," *Infrared Physics & Technology*, vol. 43, no. 3, pp. 187–210, 2002.

[7] E. Chen and A. Murphy, *Broadband optical modulators: science, technology, and applications.* CRC press, 2011.

[8] J. A. Schuller, E. S. Barnard, W. Cai, Y. C. Jun, J. S. White, and M. L. Brongersma, "Plasmonics for extreme light concentration and manipulation," *Nature materials*, vol. 9, no. 3, pp. 193–204, 2010.

[9] H. Spanggaard and F. C. Krebs, "A brief history of the development of organic and polymeric photovoltaics," *Solar Energy Materials and Solar Cells*, vol. 83, no. 2, pp. 125–146, 2004.

[10] E. F. Schubert and J. K. Kim, "Solid-state light sources getting smart," *Science*, vol. 308, no. 5726, pp. 1274–1278, 2005.

[11] E. F. Schubert, T. Gessmann, and J. K. Kim, *Light emitting diodes.* Wiley Online Library, 2005.

[12] W. W. Chow, S. W. Koch, and M. I. Sargent, *Semiconductor-laser physics.* Springer Science & Business Media, 2012.

[13] E. Yablonovitch, "Inhibited spontaneous emission in solid-state physics and electronics," *Physical review letters*, vol. 58, no. 20, p. 2059, 1987.

[14] Z. Alferov, "Double heterostructure lasers: early days and future perspectives," *IEEE Journal of Selected Topics in Quantum Electronics*, vol. 6, no. 6, pp. 832–840, 2000.

[15] Y. Xia, P. Yang, Y. Sun, Y. Wu, B. Mayers, B. Gates, Y. Yin, F. Kim, and H. Yan, "One-dimensional nanostructures: synthesis, characterization, and applications," *Advanced materials*, vol. 15, no. 5, pp. 353–389, 2003.

[16] R. Yan, D. Gargas, and P. Yang, "Nanowire photonics," *Nature Photonics*, vol. 3, no. 10, pp. 569–576, 2009.

[17] R. G. Hobbs, N. Petkov, and J. D. Holmes, "Semiconductor nanowire fabrication by bottom-up and top-down paradigms," *Chemistry of Materials*, vol. 24, no. 11, pp. 1975–1991, 2012.

[18] Y. Wu and P. Yang, "Direct observation of vapor- liquid- solid nanowire growth," *Journal of the American Chemical Society*, vol. 123, no. 13, pp. 3165–3166, 2001.

[19] W. Lu and C. M. Lieber, "Nanoelectronics from the bottom up," *Nature materials*, vol. 6, no. 11, pp. 841–850, 2007.

[20] M. H. Huang, S. Mao, H. Feick, H. Yan, Y. Wu, H. Kind, E. Weber, R. Russo, and P. Yang, "Room-Temperature Ultraviolet Nanowire Nanolasers," *Science*, vol. 292, no. 5523, pp. 1897–1899, 2001.

[21] I. Park, Z. Li, A. P. Pisano, and R. S. Williams, "Top-down fabricated silicon nanowire sensors for real-time chemical detection," *Nanotechnology*, vol. 21, no. 1, p. 015501, 2009.

[22] P. Yang, H. Yan, S. Mao, R. Russo, J. Johnson, R. Saykally, N. Morris, J. Pham, R. He, and H.-J. Choi, "Controlled growth of ZnO nanowires and their optical properties," *Advanced Functional Materials*, vol. 12, no. 5, p. 323, 2002.

[23] A. I. Persson, M. W. Larsson, S. Stenström, B. J. Ohlsson, L. Samuelson, and L. R. Wallenberg, "Solid-phase diffusion mechanism for gaas nanowire growth," *Nature materials*, vol. 3, no. 10, pp. 677–681, 2004.

[24] A. I. Hochbaum, R. Fan, R. He, and P. Yang, "Controlled growth of si nanowire arrays for device integration," *Nano letters*, vol. 5, no. 3, pp. 457–460, 2005.

[25] Y. Wu and P. Yang, "Germanium nanowire growth via simple vapor transport," *Chemistry of Materials*, vol. 12, no. 3, pp. 605–607, 2000.

[26] J. Motohisa, J. Noborisaka, J. Takeda, M. Inari, and T. Fukui, "Catalyst-free selective-area movpe of semiconductor nanowires on (111) b oriented substrates," *Journal of Crystal Growth*, vol. 272, no. 1, pp. 180–185, 2004.

[27] R. Wagner and W. Ellis, "Vapor-liquid-solid mechanism of single crystal growth," *Applied Physics Letters*, vol. 4, no. 5, pp. 89–90, 1964.

[28] E. Givargizov, "Fundamental aspects of vls growth," *Journal of Crystal Growth*, vol. 31, pp. 20–30, 1975.

[29] A. V. Maslov and C. Z. Ning, "Reflection of guided modes in a semiconductor nanowire laser," *Applied Physics Letters*, vol. 83, no. 6, pp. 1237–1239, 2003.

[30] J. C. Johnson, H.-J. Choi, K. P. Knutsen, R. D. Schaller, P. Yang, and R. J. Saykally, "Single gallium nitride nanowire lasers," *Nat Mater*, vol. 1, no. 2, pp. 106–110, 2002.

[31] B. Hua, J. Motohisa, Y. Ding, S. Hara, and T. Fukui, "Characterization of Fabry-Pérot microcavity modes in GaAs nanowires fabricated by selective-area metal organic vapor phase epitaxy," *Applied Physics Letters*, vol. 91, no. 13, pp. –, 2007.

[32] X. Duan, Y. Huang, R. Agarwal, and C. M. Lieber, "Single-nanowire electrically driven lasers," *Nature*, vol. 421, no. 6920, pp. 241–245, 2003.

[33] D. Saxena, F. Wang, Q. Gao, S. Mokkapati, H. H. Tan, and C. Jagadish, "Mode Profiling of Semiconductor Nanowire Lasers," *Nano Letters*, 2015.

[34] S. Arab, P. D. Anderson, M. Yao, C. Zhou, P. D. Dapkus, M. L. Povinelli, and S. B. Cronin, "Enhanced Fabry-Perot resonance in GaAs nanowires through local field enhancement and surface passivation," *Nano Research*, vol. 7, no. 8, pp. 1146–1153, 2014.

[35] A. F. Oskooi, D. Roundy, M. Ibanescu, P. Bermel, J. D. Joannopoulos, and S. G. Johnson, "Meep: A flexible free-software package for electromagnetic simulations by the FDTD method," *Computer Physics Communications*, vol. 181, no. 3, pp. 687–702, 2010.

[36] K.-J. Bathe, *Finite element procedures*. Klaus-Jurgen Bathe, 2006.

[37] I.-H. Tan, G. Snider, L. Chang, and E. Hu, "A self-consistent solution of schrödinger–poisson equations using a nonuniform mesh," *Journal of applied physics*, vol. 68, no. 8, pp. 4071–4076, 1990.

[38] S. Birner, T. Zibold, T. Andlauer, T. Kubis, M. Sabathil, A. Trellakis, and P. Vogl, "Nextnano: general purpose 3-d simulations," *IEEE Transactions on Electron Devices*, vol. 54, no. 9, pp. 2137–2142, 2007.

[39] B. M. Wong, F. Léonard, Q. Li, and G. T. Wang, "Nanoscale effects on heterojunction electron gases in GaN/AlGaN core/shell nanowires," *Nano Letters*, vol. 11, no. 8, pp. 3074–3079, 2011.

[40] A. Bertoni, M. Royo, F. Mahawish, and G. Goldoni, "Electron and hole gas in modulation-doped $GaAs/Al_{1-x}Ga_xAs$ radial heterojunctions," *Physical Review B*, vol. 84, no. 20, 2011.

[41] D. Wolf, H. Lichte, G. Pozzi, P. Prete, and N. Lovergine, "Electron holographic tomography for mapping the three-dimensional distribution of electrostatic potential in III-V semiconductor nanowires," *Applied Physics Letters*, vol. 98, no. 26, pp. 264103–264103–3, 2011.

[42] L. Asryan and R. Suris, "Theory of threshold characteristics of semiconductor quantum dot lasers," *Semiconductors*, vol. 38, no. 1, pp. 1–22, 2004.

[43] Z. Wang and B. Nabet, "Nanowire Optoelectronics," *Nanophotonics*, vol. 4, no. 1, 2015.

[44] D. J. Bergman and M. I. Stockman, "Surface Plasmon Amplification by Stimulated Emission of Radiation: Quantum Generation of Coherent Surface Plasmons in Nanosystems," *Physical Review Letters*, vol. 90, no. 2, p. 027402, 2003.

[45] K. Montazeri, Z. Wang, and B. Nabet, "Plasmonic effect of low-dimensional electron gas in core-shell nanowires," in *Frontiers in Optics*, pp. JTh2A–6, Optical Society of America, 2016.

[46] X. Zhang, J. K. Lin, S. Wickramanayaka, S. Zhang, R. Weerasekera, R. Dutta, K. F. Chang, K.-J. Chui, H. Y. Li, D. S. Wee Ho, L. Ding, G. Katti, S. Bhattacharya, and D.-L. Kwong, "Heterogeneous 2.5D integration on through silicon interposer," *Applied Physics Reviews*, vol. 2, no. 2, p. 021308, 2015.

APPENDIX A

TRANSITION RATES

This research project focuses on the dimensional dependence of the absorption behavior in semiconductor when interacting with light. Through time-dependent perturbation theory, we find out the transition rate and Fermis Golden Rule, then based on the light interaction Hamiltonian, time average Poynting vector and matrix element, derive the absorption coefficient for bulk semiconductor (3-dimension), quantum well (2-dimension) and quantum wire (1-dimension) structure. Finally, this report will discuss the partial confinement on the electron in the conduction band without the hole confined in the valence band situation.

The Schrödinger equation:

$$\mathcal{H}\Psi(r,t) = -\frac{\hbar}{i}\frac{\partial}{\partial t}\Psi(r,t) \tag{A.1}$$

The Hamiltonian $\mathcal{H}$ can be expressed as:

$$\mathcal{H} = \mathcal{H}_0 + \mathcal{H}'(r,t) \tag{A.2}$$

where $\mathcal{H}_0$ is the unperturbed part Hamiltonian and is time-independent, $\mathcal{H}'(r,t)$ is the small perturbation.

The solution to the unperturbed part is assumed known:

$$\begin{aligned}\mathcal{H}_0\Psi_n(r,t) &= -\frac{\hbar}{i}\frac{\partial}{\partial t}\Psi_n(r,t),\\ \frac{dN_p}{dt} &= \Gamma v_g g N_p + \Gamma\beta_{sp}R_{sp} - \frac{N_p}{\tau_p},\end{aligned} \tag{A.3}$$

The time-dependent perturbation is assumed to have the form

$$\mathcal{H} = \begin{cases}\mathcal{H}'(r)e^{-i\omega t} + \mathcal{H}'^{+}(r)e^{+\omega t}, & t \geq 0\\ 0, & t < 0\end{cases} \tag{A.4}$$

Expand the wave function in terms of the unperturbed solution, we find out $\Psi(r,t)$:

$$\Psi(r,t) = \sum_n a_n(t)\Phi_n(r)e^{(-iE_nt/\hbar)} \tag{A.5}$$

$|a_n(t)|^2$ gives the probability that the electron is in the state n at time t.

Substituting the expansion for Ψ into Schrödinger equation and using A.3, we have

$$\sum_n \frac{da_n(t)}{dt}\Psi_n(r)e^{-iE_nt/\hbar} = -\frac{\hbar}{i}\sum_n \mathcal{H}'(r,t)a_n(t)\Phi_n(r)e^{(-iE_nt/\hbar)} \tag{A.6}$$

Taking the inner product with the wave function ${\Phi_m}^{\star}(r)$, and using the orthonormal property,

$$\int d^3\boldsymbol{r}{\Phi^*}_m(\boldsymbol{r})\Phi_n(\boldsymbol{r}) = \delta_{mn} \tag{A.7}$$

We find:

$$\frac{da_n(t)}{dt} = -\frac{i}{\hbar}\sum_n a_n(t){\mathcal{H}'}_{mn}(t)e^{i\omega_{mn}t} \tag{A.8}$$

where

$$\begin{aligned}\mathcal{H}'_{mn}(t) &= \langle m|\mathcal{H}'(\boldsymbol{r},t)|n\rangle \\ &= \int \Phi^*{}_m(\boldsymbol{r})\mathcal{H}'(\boldsymbol{r},t)\Psi_n(\boldsymbol{r})d^3\boldsymbol{r} \\ &= \mathcal{H}'_{mn}e^{-i\omega t} + \mathcal{H}'_{mn}e^{+i\omega t}\end{aligned} \tag{A.9}$$

$$\omega_{mn} = (E_m - E_n)/\hbar \tag{A.10}$$

and the matrix element is:

$$\mathcal{H}'_{mn}(t) = \int \Phi^*{}_m(\boldsymbol{r})\mathcal{H}'(\boldsymbol{r},t)\Psi_n(\boldsymbol{r})d^3\boldsymbol{r} \tag{A.11}$$

Introducing the perturbation parameter λ

$$\mathcal{H} = \mathcal{H}_0 + \lambda\mathcal{H}'(\boldsymbol{r},t) \tag{A.12}$$

and letting

$$a_n(t) = a^{(0)}{}_n + \lambda a^{(1)}{}_n(t) + \lambda^2 a^{(2)}{}_n(t) + \cdots \tag{A.13}$$

we can take the derivative and set $\lambda = 1$

$$\begin{aligned}
\frac{da^{(0)}{}_n(t)}{dt} &= 0 \\
\frac{da^{(1)}{}_n(t)}{dt} &= -\frac{i}{\hbar}\sum_n a_n^{(0)}(t)\mathcal{H}'{}_{mn}(t)e^{i\omega_{mn}t} \\
\frac{da^{(2)}{}_n(t)}{dt} &= -\frac{i}{\hbar}\sum_n a_n^{(1)}(t)\mathcal{H}'{}_{mn}(t)e^{i\omega_{mn}t}
\end{aligned} \tag{A.14}$$

Thus, the zeroth-order solutions for equation A.14 are constant. Let the electron be at the state i initially

$$a^{(0)}{}_i(t=0) = 1; \quad a^{(0)}{}_m(t) = 0, \quad m \neq i \tag{A.15}$$

We have the zeroth-order solution

$$a^{(0)}{}_i(t=0) = 1; \quad a^{(0)}{}_m(t) = 0, \quad m \neq i \tag{A.16}$$

Therefore, the electron stays at the state i in the absence of any perturbation. The first order solution is

$$\begin{aligned}
\frac{da_n^{(1)}}{dt} &= -\frac{i}{\hbar}\mathcal{H}'{}_{mn}(t)e^{i\omega_{mn}t} \\
&= -\frac{i}{\hbar}[\mathcal{H}'{}_{mi}e^{-i(\omega_{mi}-\omega)t} + \mathcal{H}'{}_{mi}e^{+i(\omega_{mi}-\omega)t}]
\end{aligned} \tag{A.17}$$

If for final state $m = f$; then integrate above equation, we have

$$a_f^{(1)}(t) = -\frac{i}{\hbar}[\mathcal{H}'{}_{fi}\frac{e^{-i(\omega_{mi}-\omega)t}}{\omega_{fi}-\omega} + \mathcal{H}'^{+}{}_{fi}\frac{e^{+i(\omega_{mi}-\omega)t}}{\omega_{fi}+\omega}] \tag{A.18}$$

If we consider the photon energy to be near resonance, either $\omega \sim \omega_{fi}$ or $\omega \sim -\omega fi$, we find the dominant terms:

$$a_f^{(1)}(t) = \frac{4|\mathcal{H}'_{fi}|^2}{\hbar^2}\frac{sin^2\frac{t}{2}(\omega_{fi}-\omega)}{(\omega_{fi}-\omega)^2} + \frac{4|\mathcal{H}'_{fi}|^2}{\hbar^2}\frac{sin^2\frac{t}{2}(\omega_{fi}+\omega)}{(\omega_{fi}+\omega)^2} \tag{A.19}$$

where the cross-term has been dropped because it is small compared with either of the above two terms.

When the interaction time is long enough, using approcimation

$$\frac{sin^2(\frac{xt}{2})}{x^2} \to \frac{\pi t}{2}\delta(x) \tag{A.20}$$

Then

$$|a_f^{(1)}(t)|^2 = \frac{2\pi t}{\hbar^2}|\mathcal{H}'_(fi)|^2\delta(\omega_{fi}-\omega) + \frac{2\pi t}{\hbar^2}|\mathcal{H}'_(fi)|^2\delta(\omega_{fi}+\omega) \tag{A.21}$$

The transition rate should be, after using the property of

$$\delta(\hbar\omega) = \frac{\delta(w)}{\hbar} \tag{A.22}$$

$$\begin{aligned} W_{if} &= \frac{d|a_f^{(1)}(t)|^2}{dt} \\ &\frac{2\pi}{\hbar}|\mathcal{H}'_(fi)|^2\delta(E_f-E_i-\hbar\omega) + \frac{2\pi}{\hbar}|\mathcal{H}'_(fi)|^2\delta(E_f-E_i+\hbar\omega) \end{aligned} \tag{A.23}$$

where $E_f = E_i + \hbar\omega$ represents the absorption of a photon by an electron, and $E_f = E_i - \hbar\omega$

corresponds with the emission of a photon.

$$I_{hm}^{en} = \int_{-\infty}^{\infty} \Phi_n^*(z) g_m(z)\,\mathrm{d}z, \tag{A.24}$$

$$I_{hm}^{en} = \int_{-\infty}^{\infty} \Phi_n^*(z) g_m(z)\,\mathrm{d}z, \tag{A.25}$$

Therefore, the electron stays at the state i in the absence of any perturbation. The first order solution is

If we consider the photon energy to be near resonance, either or, we find the dominant terms: The absorption coefficient is a strong function of dimensionality. The confining situation of the quantum structure will considerably affect the energy levels, the overlap function of the conduction and valance band envelope function and also the joint optical density of state. Through the derivation of the absorption coefficient, we can observe the interaction between the light and semiconductor. The next questions should address: 1. The simulation data for single nanowire abs

APPENDIX B

SEMICONDUCTOR LASER MODELING

In this section, we are trying to delve into the mechanics of how an injected current actually results in an optical output in a semiconductor heterojunction laser by providing a systematic derivation of the dc light-current characteristics. First, the rate equation for photon generation and loss in a laser cavity is developed. This shows that only a small portion of the spontaneously generated light contributes to the lasing mode. Most of it comes from the stimulated recombination of carriers. All of the carriers that are stimulated to recombine by light in a certain mode contribute more photons to that same mode. Thus, the stimulated carrier recombination/photon generation process is a gain process. We find the threshold gain for lasing which is the gain necessary to compensate for cavity losses. The threshold current is the current required to reach this gain

For electrons and holes in the active region of a diode laser, only a fraction, η_i, of injected current will contribute to the generation of carriers.We assumed the active regions that are undoped or lightly doped, so that under high injection levels, charge neutrality applies and the electron density equals the hole density (i.e., $N = P$ in the active region). Thus, we can greatly simplify our analysis by specifically tracking only the electron density, N.

We start with the governing equations of carrier density and photon density in the active region which is governed by a dynamic process.

$$\begin{aligned}\frac{dN}{dt} &= \frac{\eta_i I}{qV} - \frac{N}{\tau} - R_{st}, \\ \frac{dN_p}{dt} &= \Gamma v_g g N_p + \Gamma \beta_{sp} R_{sp} - \frac{N_p}{\tau_p},\end{aligned} \tag{B.1}$$

where β_{sp} is the spontaneous emission factor, defined as the percentage of the total spontaneous emission coupled into the lasing mode. And it is just the reciprocal of the number of available optical modes in the bandwidth of the spontaneous emission for uniform coupling to all modes. The g is Incremental gain per unit length.

The first term of equation 1 is the rate of injected electrons $G_{gen} = \Gamma_i I/qV$, $\Gamma_i I/q$ is the number of electrons per second being injected into the active region, where V is the volume of the active region. The rest terms are the rate of recombining of electrons per unit volume in the active region. There are several mechanisms should be considered, including a spontaneous recombination rate, R_{sp}, a nonradiative recombination rate, R_{nr}, a carrier leakage rate, R_l and a net stimulated recombination, R_{st}, including both stimulated absorption and emission. Which looks like:

$$R_{rec} = R_{sp} + R_{nr} + R_l + R_{st} \tag{B.2}$$

The first three terms on the right refer to the natural or unstimulated carrier decay processes. The fourth one, R_{st}, require the presence of photon.

The natural decay process can be described by a carrier lifetime, τ. In the absence of photon or a generation term, the rate equation for carrier decay is $dN/dt = -N/\tau$, where $N/\tau = R_{sp} + R_{nr} + R_l$.

The natural decay rate can also be expressed in a power series of the carrier density, N. We can also rewrite $R_{rec} = BN^2 + (AN + CN^3) + R_{st}$. Where R_{sp} BN^2 and $R_{nr} + R_l$ $(AN + cN^3)$. The coefficient B is the bimolecular recombination coefficient, and it has a magnitude, $B \sim 10^{-10} cm^3/s$ for most AlGaAs and InGaAsP alloys of interest.

When a laser is below threshold, in which the gain is insufficient to compensate for cavity losses,

the generated photons do not receive net amplification. The spontaneous photon generation rate per unit volume is exactly equal to the spontaneous electron recombination rate, R_{sp}, because an electron-hole pair will emit a photon when they recombine radiatively. Under steady-state conditions ($dN/dt = 0$), the generation rate equals the recombination rate with $R_{st} = 0$.

$$\frac{\eta_i I}{qV} = R_{sp} + R_{nr} + R_l \tag{B.3}$$

The spontaneously generated optical power, P_{sp}, is obtained by multiplying the number of photons generated per unit time per unit volume, R_{sp}, by the energy per photon, $h\upsilon$, and the volume of the active region, V.

$$P_{sp} = h\upsilon V R_{sp} = \eta_i \eta_r \frac{h\upsilon}{q} I \tag{B.4}$$

The main photon generation term above threshold is R_{st}. Electron-hole pair is stimulated to recombine, another photon is generated. But since the cavity volume occupied by photons, V_p, is usually larger than the active region volume occupied by electrons, V, the photon density generation rate will be $[V/V_p]R_{st}$, not just R_{st}. The electron-photon overlap factor, $[V/V_p]$, is generally referred to as the confinement factor, Γ.

B.1 Threshold or Steady-State Gain in Lasers

The cavity loss can be characterized by a photon decay constant or lifetime, τ_p, and the gain necessary to overcome losses, and thus reach threshold. By assuming steady-state conditions (i.e. $dN_p/dt = 0$), and solving for this steady-state or threshold gain, g_{th}, where the generation term equals the recombination term for photons. We assume only a small fraction of the spontaneous emission is coupled into the mode (i.e. β_{sp} is quite small), then the second term can be neglected,

and we have the solution:

$$\Gamma g_{th} = \frac{1}{v_g \tau_p} =< \alpha_i > +\alpha_m \tag{B.5}$$

The product, Γg_{th}, is referred to as the threshold modal gain because it now represents the net gain required for the mode as a whole, and it is the mode as a whole that experiences the cavity loss. $< \alpha_i >$ is the average internal loss, and α_m is the mirror loss if we considered an in-plane wave laser.

The optical energy of a nano-cavity laser propagates in a dielectric waveguide mode, which is confined both transversely and laterally as defined by a normalized transverse electric field profile, $U(x, y)$. In the axial direction this mode propagates as $exp^{(-j\beta z)}$, where β is the complex propagation constant, which includes any loss or gain. Thus, the time- and space-varying electric field can be written as

$$\xi = \hat{e}_y E_0 U(x, y) e^{j(\omega t - \beta z)} \tag{B.6}$$

where $\hat{e}_y$ is the unit vector indicating TE polarization and E_0 is the magnitude of the field. The complex propagation constant, β, includes the incremental transverse modal gain, $< g >_{xy}$ and internal modal loss, $< \alpha_i >_{xy}$. If we consider a Fabry-Perot laser with the propagating mode is reflected by end mirrors, and the reflection coefficients are r_1 and r_2. respectively. In addition, the mean mirror intensity reflection coefficient, $R = r_1 r_2$.

Define the mirror lass as α_m

$$\alpha_m \equiv \frac{1}{L} \ln(\frac{1}{R}) \tag{B.7}$$

The photon decay lifetime is given by,

$$\frac{1}{\tau_p} = \frac{1}{\tau_i} + \frac{1}{\tau_m} = v_g(< \alpha_i > +\alpha_m) \tag{B.8}$$

Thus, we can also write

$$\Gamma g_{th} =< \alpha_i > +\alpha_m = \frac{1}{v_g \tau_p} \tag{B.9}$$

B.2 Threshold Current and Output Power

We construct together a below-threshold and an above-threshold characteristic to illustrate the output power versus input current for a normal diode laser. The first step is to use the below-threshold steady-state carrier rate equation,

$$\frac{\eta_i I_{th}}{qV} = (R_{sp} + R_{nr} + R_l)_{th} = \frac{N_{th}}{\tau} \tag{B.10}$$

Then, recognizing that $(R_{sp} + R_{nr} + R_l) = AN + BN^2 + CN^3$ depends monotonically on N, we observe from eq 2.34 that above threshold $(R_{sp} + R_{nr} + R_l)$ will also clamp at its threshold value, given by Eq 2.35. Thus, we can substitute Eq 2.35 into the carrier rate equation, eq 2.16 to obtain a new above threshold carrier rate equations,

$$\frac{dN}{dt} = \eta_i \frac{(I - I_{th})}{qV} - v_g g N_p, \quad (I > I_{th}) \tag{B.11}$$

We also calculate a steady-state photon density above threshold where $g = g_{th}$,

$$N_p = \frac{\eta_i (I - I_{th})}{q v_g g th V} \quad (steady\ state) \tag{B.12}$$

To obtain the power out, we first construct the stored optical energy in the cavity, E_{os}, by multiplying the photon density, N_p, by the energy per photon, hv, and the cavity volume, V_p. That is $E_{os} = N_p h v V_p$. Then, we multiply this by the erngy loss rate through the mirrors, $v_g \alpha_m = \frac{1}{\tau_m}$, to get the

optical power output from the mirrors,

$$P_0 = v_g \alpha_m N_p h v V_p \tag{B.13}$$

Substituting from , and using $\Gamma = V/V_p$,

$$P_0 = \eta_i (\frac{\alpha_m}{< \alpha_i > + \alpha_m}) \frac{hv}{q} (I - Ith), \quad (I > I_{th}) \tag{B.14}$$

For the output power below-threshold ($I < I_{th}$) can be approximated by neglecting the stimulated emission term and solving for N_p under steady-state conditions.

$$N_p = \Gamma \beta_{sp} R_{sp} \tau p \quad (I < I_{th}) \tag{B.15}$$

and

$$P_0(I < I_{th}) = \eta_r \eta_i \left(\frac{\alpha_m}{< \alpha_i > + \alpha_m} \right) \frac{hv}{q} \beta_{sp} I, \tag{B.16}$$

We can get the threshold carrier density

$$N_{th} = N_{tr} e^{g_{th}/g_0 N} = N_{tr} e^{(<\alpha_i> + \alpha_m)/\Gamma g_0 N} \tag{B.17}$$

Using the polynomial fit for the recombination rates, and recognizing that for the best laser material the recombination at threshold is dominated by spontaneous recombination, we have, $I_{th} \cong BN_{th}{}^2 qV/\eta_i$, Thus

$$I_{th} \cong \frac{qVBN_{tr}{}^2}{\eta_i} e^{(<\alpha_i> + \alpha_m)/\Gamma g_0 N} \tag{B.18}$$

where for most $III-V$ materials the bimolecular recombination coefficient, $B \sim 10^{-10} cm^3/s$.

For a multiple quantum-well (MQW) lasers, we have to multiply the single-well confinement factor, Γ_1, and volume, V_1, by the number of wells, N_w.

$$I_{thMQW} \cong \frac{qN_w V_1 B {N_{tr}}^2}{\eta_i} e^{2(<\alpha_i>+\alpha_m)/N_w \Gamma_1 g_0 N} \tag{B.19}$$

APPENDIX C

MEEP SIMULATION CODE

C.1 Cylindrical Core-Shell Nanowire

```
; By Zhihuan Wang, 06-27-2013
; Calculating 1D cylindrical GaAs/AlGaAs core-shell nanowire excitation
    mode using cylindrical coordinates.

;%%% length unit %%%
; fundamental length unit in meep is um
;(define nm 0.001)    ; nano-meter unit
;(define um 1)        ; micro-meter unit

;-------------------------Parameter Setup---------------------------------
(define-param nc 3.4) ; index of nanowire core
(define-param ns 3.1349) ; index of nanowire shell
(define-param w 0) ; width of nanowire

(define-param r 1.1) ; radius of core
(define-param rtotal 1.5) ; radius of total (core+shell)

(define-param pad 0.5) ; padding between waveguide and edge of PML
(define-param gap 0.4) ; padding between cylinder and cell edge in XY plane
(define-param dpml 1.5) ; thickness of PML
```

```
20
21 ;------------------Dimension and size of the computational cell-----------
22 (define sxy (* 2 (+ rtotal w pad dpml))) ; cell size in XY plane
23 (set! geometry-lattice (make lattice (size sxy sxy no-size)))
24
25 ;------------------------Geometric Setup---------------------------------
26 (set! geometry (list
27                 (make cylinder (center 0 0) (height infinity)
28                 (radius rtotal ) (material (make dielectric (index ns))))
29
30                 (make cylinder (center 0 0) (height infinity)
31                 (radius r) (material (make dielectric (index nc))))))
32
33 ;------------------------------PML layers set up--------------------------
34 (set! pml-layers (list (make pml (thickness dpml))))
35 (set-param! resolution 20)
36 ;-------------------------------Source set up-----------------------------
37 (define-param fcen 0.15) ; pulse center frequency
38 (define-param df 0.1)  ; pulse width (in frequency)
39 ;(define-param nfreq 500); number of frequencies at which to compute flux
40
41 (set! sources (list
42                 (make source
43                   (src (make gaussian-src (frequency fcen) (fwidth df)))
44                   (component Ez) (center (+ rtotal 0.5) 0))))
45 ; note that the r -> -r mirror symmetry is exploited automatically
46
47 ;---------------------------run meep----------------------------------------
48 (run-sources+ 300
```

```
49                (at-beginning output-epsilon)
50                (after-sources (harminv Ez (vector3 (+ rtotal 0.5)) fcen df)))
51 (run-until (/ 1 fcen) (at-every (/ 1 fcen 20) output-efield-z))
```

snippet/sourcecode/CylindCS.ctl

C.2 Hexagonal Core-Shell Nanowire

```
1  ; Calculating GaAs/AlGaAs single Hexagon core-shell nanowire excitation mode
2  ; By Zhihuan Wang 07-01-2013
3  ; Will examine the diameter varing from 20 50 90 130 170 210 250 290 330
4  ; Incident light source wavelength is 532 nm fcen=0.1879
5  ;------------------------Parameter Setup-----------------------------------
6  (reset-meep)
7  (define-param n 3.4) ; index of waveguide
8  (define-param ns 3.3) ; index of waveguide shell
9
10 (define-param w 0) ; width of waveguide
11 (define-param r 1.65) ; outer radius of ring
12 (define-param l 10)   ; length of the nanowire
13 (define-param rc (* 0.4 r)) ; inner radius of ring
14
15 (define-param pad 0.5) ; padding between waveguide and edge of PML
16 (define-param dpml 1) ; thickness of PML
17
18 ;-----------------Dimension and size of the computational cell-------------
19 (define C->L (compose cartesian->lattice vector3))
20 (define sxy (* 2 (+ r w pad dpml))) ; cell size y
21 (define sxz (* 2 (+ l w pad dpml))) ; cell size z
22
```

```
;----------------------Geometric Setup----------------------------------
(set! geometry-lattice (make lattice (size sxy sxy sxz)))
(set! geometry (append
    (list
     (make block (center 0 0) (size (* r (sqrt (/ 4 3))) (* 2 r) l)
     (e1  (C->L 1 0)) (e2  (C->L 0 1))
       (material (make dielectric (index ns))))
     (make block (center 0 0) (size (* r (sqrt (/ 4 3))) (* 2 r) l)
     (e2 ( C->L (/ (sqrt 3) 2) 0.5)) (e1  (C->L -0.5 (/ (sqrt 3) 2) ))
     (material (make dielectric (index ns))))

     (make block (center 0 0) (size (* r (sqrt (/ 4 3))) (* 2 r) l)
       (e2  ( C->L (/ (sqrt 3) 2) -0.5)) (e1  (C->L 0.5 (/ (sqrt 3) 2)) )
     (material (make dielectric (index ns))))
         (make block (center 0 0) (size (* rc (sqrt (/ 4 3))) (* 2 rc) l)
     (e1  (C->L 1 0)) (e2  (C->L 0 1))
     (material (make dielectric (index n))))
     (make block (center 0 0) (size (* rc (sqrt (/ 4 3))) (* 2 rc) l)
     (e2 ( C->L (/ (sqrt 3) 2) 0.5)) (e1  (C->L -0.5 (/ (sqrt 3) 2) ))
     (material (make dielectric (index n))))
     (make block (center 0 0) (size (* rc (sqrt (/ 4 3))) (* 2 rc) l)
     (e2  ( C->L (/ (sqrt 3) 2) -0.5)) (e1  (C->L 0.5 (/ (sqrt 3) 2)) )
     (material (make dielectric (index n)))))))

;----------------------------PML layers set up-----------------------------
(set! pml-layers (list (make pml (thickness dpml))))
(set-param! resolution 10)
;-----------------------------Source set up--------------------------------
(define-param fcen 0.1879) ; pulse center frequency
```

```
(define-param df 0.02)  ; pulse width (in frequency)
(set! sources (list
            (make source
              (src (make gaussian-src (frequency fcen) (fwidth df)))
              (component Ez) (center (+ r 0.1) 0))))

;---------------------------run meep---------------------------------------
(run-sources+ 300
               (at-beginning output-epsilon)
               (after-sources (harminv Ez (vector3 (+ r 0.1)) fcen df)))
(run-until (/ 1 fcen) (at-every (/ 1 fcen 20) output-efield-z
    output-tot-pwr))
```

snippet/sourcecode/HexCS3D.ctl

APPENDIX D

GAIN SPECTRUM AND THRESHOLD CALCULATION MATLAB CODE

```
%% gain (Gain Spectral Analysis Method to determin the enhancement factor for
    reduceced dimensionality
% with Approximations for simple geometry and variables)
% Modified for single band transitions and without scattering broadening effect

% Created on 8/25/2014 By Zhihuan Wang (GaAs/AlGaAs core-shell nanowire)
% Modified by 11/4/2016
clc; close all;

J_eV = 1.60217657e-19; %Joules per eV
eV_J = 6.24150934e18; % eV per Joule

%% Photon energy & system input (variables initiate)
E_ph = 1.2:0.01:2;
n = 6e18:3e18:3e19;
p = 6e18:3e18:3e19;  % Hole carrier concentration, Unit [cm^-3]

k = length(E_ph);
len_n = length(n);
abs_coef3D = size(k);
abs_coef2D = size(k);
abs_coef1D = size(k);
k0_3D = size(k);
gain_3D = size(k, len_n);
```

```
gain_2D = size(k, len_n);
gain_1D = size(k, len_n);
enhance_abs = size(k);
sp_rate3D = size(k);
sp_rate2D = size(k);
sp_rate1D = size(k);
enhance_sp = size(k);
st_rate3D = size(k);
st_rate2D = size(k);
st_rate1D = size(k);
enhance_st = size(k);

f_v = size(k, len_n);
f_c = size(k, len_n);
Fc = size(len_n);
Fv = size(len_n);

maxgain_3D = size(len_n);
maxgain_2D = size(len_n);
maxgain_1D = size(len_n);
%% Refractive index without material dispersion
% Uncommented if need dispersion
n_r = 3.312; % refractive index without material dispersion

%% Parameters in MKS units
H_j = 6.63e-34;%Plancks constant [J.s]
H = 4.14e-15;%Plancks constant [eV.s]
H_rj = 1.05e-34;% Reduced Plancks constant [J.s]
H_r = 6.58e-16;% Reduced Plancks constant [eV.s]
C = 3e10; %speed of light [cm/s]
e = 1.6e-19; %elementary charge [C]
kB = 1.38*10^-23; % Boltzmann's constant [J/K]
T = 300; % room temperature [K]
m0 = 9.11e-31; % Electron rest mass [kg]
```

```
58 Eg=1.424; %Energy bandgap for GaAs at 300K [eV]
59 m_e = 0.067*m0; %Electron Effective mass for GaAs[unitless /m0]
60 m_h = 0.47*m0; %Hole Effective mass for GaAs 3D[unitless /m0]
61 m_h2D = 0.118*m0; %Hole Effective mass for GaAs 2D[unitless /m0]
62 m_h1D = 0.027*m0; %Hole Effective mass for GaAs 1D[unitless /m0]
63 m_hh = 0.50*m0; %heavey hole Effective mass for GaAs[unitless /m0]
64 m_lh = 0.087*m0; %Light hole Effective mass for GaAs[unitless /m0]
65 m_r = m_e*m_h/(m_e+m_h); % Reduced effective mass
66 m_r2D = m_e*m_h/(m_e+m_h2D); % Reduced effective mass 2D
67 m_r1D = m_e*m_h/(m_e+m_h1D); % Reduced effective mass 1D
68
69 m0SI = 5.693e-16; %Electron rest mass [kg]
70 m_eSI = 0.067*m0SI; %Electron Effective mass for GaAs[unitless /m0]
71 m_hSI = 0.47*m0SI; %Hole Effective mass for GaAs 3D[unitless /m0]
72 m_rSI = m_eSI*m_hSI/(m_eSI+m_hSI); % Reduced effective mass
73
74 m00 = 9.11*10^-28; %Electron rest mass [kg]
75 m_ee = 0.067*m00; %Electron Effective mass for GaAs[unitless /m0]
76 m_hh = 0.47*m00; %Hole Effective mass for GaAs 3D[unitless /m0]
77 m_rr = m_ee*m_hh/(m_ee+m_hh); % Reduced effective mass
78 m_rr2D = m_e*m_h/(m_e+m_h2D); % Reduced effective mass 2D
79 m_rr1D = m_e*m_h/(m_e+m_h1D); % Reduced effective mass 1D
80
81 Lx = 50e-8; % 50 A for length [cm]
82 Ly = 50e-8;
83 Lz = 50e-8;
84 Lz3D = 50e-5; % 50000 A for length [cm]
85 Lz2D = 50e-10; % 5000 A for length [cm]
86 Lz1D = 50e-6; % 50 A for length [cm]
87 Lzm = 100e-10;
88 a = 100e-10; %nanowire crosssection [m]
89 b = 100e-10;
90 p_cv = 2.88*10^-18;
91 f_cv = 23; %oscillator strength 3D [eV]
```

```
f_cv1D = 230; %oscillator strength 1D [eV]
eps_0 = 8.85e-14; % Permittivity of vacuum [F/cm]
Nwr = 1/(Lx*Ly); %nanowire density [cm^-2]
Ep = 25.7; % Energy parameter [eV]
%% quantized energy state for 2D
E_e1 = H_rj^2*pi^2/(2*m_e*Lzm^2)*eV_J;
E_h1 = H_rj^2*pi^2/(2*m_h*Lzm^2)*eV_J;
E_e2 = H_rj^2*pi^2*4/(2*m_e*Lzm^2)*eV_J;
E_h2 = H_rj^2*pi^2*4/(2*m_h*Lzm^2)*eV_J;
E_e3 = H_rj^2*pi^2*9/(2*m_e*Lzm^2)*eV_J;
E_h3 = H_rj^2*pi^2*9/(2*m_h*Lzm^2)*eV_J;

E_e1h1 = Eg+E_e1+E_h1; %E_h should be negative value.
E_e2h2 = Eg+E_e2+E_h2;
E_e3h3 = Eg+E_e3+E_h3;

%% quantized energy state for 1D
E_11 = Eg+H_rj^2/(2*m_r)*((pi/a)^2+(pi/b)^2)*eV_J;
E_12 = Eg+H_rj^2/(2*m_r)*((pi/a)^2+(pi*2/b)^2)*eV_J;
E_22 = Eg+H_rj^2/(2*m_r)*((pi*2/a)^2+(pi*2/b)^2)*eV_J;
E_23 = Eg+H_rj^2/(2*m_r)*((pi*2/a)^2+(pi*3/b)^2)*eV_J;
E_33 = Eg+H_rj^2/(2*m_r)*((pi*3/a)^2+(pi*3/b)^2)*eV_J;

%% Fermi distribution
Na = 1e11;%acceptor doping concentration
Nd = 1e11;%donor doping concentration
Nc = 2*(2*pi*m_e*kB*T/H_j^2)^1.5*10^-6;
Nv = 2*(2*pi*m_h*kB*T/H_j^2)^1.5*10^-6;
for j=1:len_n
Fc(j)= kB*T*(log(n(j)./Nc) + 1/sqrt(8)*(n(j)./Nc))*eV_J;
Fv(j)= kB*T*(log(p(j)./Nv) + 1/sqrt(8)*(p(j)./Nv))*eV_J;
end

% Check Joyce-Dixon approximation applicable range -1<theta<7
```

```
theta = size(len_n);
for j=1:len_n
    theta(j)= log(n(j)/Nc)+2^(-1.5)*(n(j)/Nc);
end

Ec =size(k);
Ev =size(k);
for j=1:len_n
for i=1:k
k0_3D(i) = sqrt(2*m_r*((E_ph(i)-Eg)*J_eV)/H_rj^2);
Ev(i) = -H_rj.^2*k0_3D(i).^2/(2*m_h);
Ec(i) = Eg+H_rj.^2*k0_3D(i).^2/(2*m_e);
f_c(i,j) = (1 + exp((  m_r/m_e*(E_ph(i) - Eg) - Fc(j))/(kB*T*eV_J))).^-1;
f_v(i,j) = (1 + exp(( - m_r/m_h*(Eg - E_ph(i)) + Fv(j))/(kB*T*eV_J))).^-1;
end
end

figure;
plot(E_ph, f_c, E_ph, f_v, E_ph, f_c-f_v);

%% Gain Spectrum: Gain=Absorption Coefficent* fermi distribution (g(hw)=a0(hw)[fv(k0)
    -fc(k0)])
% Without Linewidth Broadening
fe = size(k,len_n);
for j=1:len_n
for i=1:k
if E_ph(i)< Eg
gain_3D(i,j) = 0;
else
gain_3D(i,j) = (sqrt(2)*m_r^1.5*(e*eV_J)^2*(1.5*m0*Ep*J_eV/6))/(3*pi*n_r*m0*eps_0*C*
    H_rj^2*E_ph(i))*(E_ph(i)-Eg)^0.5*(f_c(i,j)-f_v(i,j));
end

if E_ph(i)< E_e1h1
```

```
158     gain_2D(i,j) = 0;
159 elseif E_e1h1<= E_ph(i)
160     gain_2D(i,j) = (e^2*pi*H_r*(1.5*m0*Ep*J_eV/6)*2)/(3*n_r*eps_0*C*m0^2*E_ph(i))*
            m_r2D/(H_rj^2*pi*Lz)*(f_c(i,j)-f_v(i,j));
161 end
162
163 if E_ph(i)< E_11
164    gain_1D(i,j) = 0;
165 elseif E_11<= E_ph(i)
166    gain_1D(i,j) = (e^2*pi*H_r*Nwr)/(3*n_r*eps_0*C*m0^2*E_ph(i))*(m0*Ep*10*J_eV/6)*(
           m_r1D^1.5/(pi*H_rj*m_e*Lx*Ly))*((E_ph(i)-E_11))^-0.5*(f_c(i,j)-f_v(i,j));
167 end
168
169 maxgain_3D(j)= max(gain_3D(:,j));
170 maxgain_2D(j)= max(gain_2D(:,j));
171 maxgain_1D(j)= max(gain_1D(:,j));
172 enhance_abs(i,j) = gain_2D(i,j)/gain_3D(i,j);
173
174 end
175 end
176
177 %% Plotting the results
178 figure;
179 subplot(2,2,1);
180 plot (E_ph, gain_3D,'LineWidth',4)
181 title('Gain coefficient versus photon energy for 3D')
182 ylabel ('Gain coefficient (/cm)')
183 xlabel ('photon energy (eV)')
184 grid on,
185
186 subplot(2,2,2);
187 plot (E_ph, gain_2D,'LineWidth',4)
188 title('Gain coefficient versus photon energy for 2D')
189 ylabel ('Gain coefficient (/cm)')
```

```
xlabel ('photon energy (eV)')
grid on,

subplot(2,2,3);
plot (E_ph, gain_1D,'LineWidth',4)
title('Gain coefficient versus photon energy for 1D')
ylabel ('Gain coefficient (/cm)')
xlabel ('photon energy (eV)')
grid on,

subplot(2,2,4);
plot (n, maxgain_2D,'LineWidth',4)
title('Maximum gain versus carrier density')
ylabel ('Gain coefficient (/cm)')
xlabel ('Carrier density (1/cm^2)')
grid on,
%% Curve fitting in order to find the threshold carrier density
% which is nth = 4.533*10^18 (1/cm^3)

nth = 4.533*10^18; % Unit (1/cm^3)
% nth = Ntr*exp(gth/g0)

%% Fermi distribution for threshold carrier density
Fc_th= kB*T*(log(nth/Nc) + 1/sqrt(8)*(nth/Nc))*eV_J;
Fv_th= kB*T*(log(nth/Nv) + 1/sqrt(8)*(nth/Nv))*eV_J;

f_vth = size(k);
f_cth = size(k);
for i=1:k
f_vth(i) = (1 + exp(( - m_r/m_h*(E_ph(i) - Eg) + Fv_th)/(kB*T*eV_J))).^-1;
f_cth(i) = (1 + exp((  m_r/m_e*(E_ph(i) - Eg) - Fc_th)/(kB*T*eV_J))).^-1;
end

%% Calculating rsp and Rsp based on the threshold carrier density
```

```
224 % Spontaneous Emission Spectrum: sp_rate = Emission Probability * Density of States *
        fermi distribution
225 % (sp_rate(hw)=Pem*Nj(hw)*[fv(k0)-fc(k0)])
226
227 for i=1:k
228 if E_ph(i)< Eg
229 sp_rate3D(i) = 0;
230 else
231 sp_rate3D(i) = (n_r*e^2*E_ph(i)*Ep*J_eV/6)/(pi*m0^2*eps_0*C^3*H_r^2)*((2*m_r)^1.5)
        /(2*pi^2*H_r^3)*((E_ph(i)-Eg)*J_eV)^0.5*(f_cth(i)*(1-f_vth(i)));
232 end
233
234 if E_ph(i)< E_e1h1
235     sp_rate2D(i) = 0;
236 elseif E_e1h1<= E_ph(i)
237 sp_rate2D(i) = (n_r*e^2*E_ph(i)*J_eV*Ep*J_eV/6)/(pi*m0^2*eps_0*C^3*H_r^2)*(m_r2D*2)/(
        pi*H_r^2*Lz2D)*(f_cth(i)*(1-f_vth(i)));
238 end
239
240 if E_ph(i)< E_11
241    sp_rate1D(i) = 0;
242 elseif E_11<= E_ph(i)
243 sp_rate1D(i) = (n_r*e^2*E_ph(i)*J_eV*Ep*J_eV/6)/(pi*m0^2*eps_0*C^3*H_r^2)*(m_r1D
        ^1.5/(pi*H_r*m_e*Lz1D*Lz1D))*(E_ph(i)-E_11)^-0.5*(f_cth(i)*(1-f_vth(i)));
244 end
245
246
247 end
248
249 Rst_3D = trapz(sp_rate3D');
250 Rst_2D = trapz(sp_rate2D');
251 Rst_1D = trapz(sp_rate1D');
252
253 %% Threshold current calculation
```

```
254
255 Jth_3D = e*Lz*Rst_3D;
256 Jth_2D = e*Lz*Rst_2D;
257 Jth_1D = e*Lz*Rst_1D;
258
259 %% Optical Outpul Power
260
261 P_3D = (Eg+0.0257/2)*Lz*Rst_3D;
262 P_2D = (Eg+0.0257/2)*Lz*Rst_2D;
263 P_1D = (Eg+0.0257/2)*Lz*Rst_1D;
264 enhance_2D = P_2D/P_3D
265 enhance_1D = P_1D/P_3D
266
267 %% Plotting the results
268 figure;
269 subplot(2,2,1);
270 plot (E_ph, sp_rate3D)
271 title('Spontaneous Emission Rate versus photon energy for 3D')
272 ylabel ('Spontaneous Emission Rate (/cm)')
273 xlabel ('photon energy (eV)')
274 grid on,
275
276 subplot(2,2,2);
277 plot (E_ph, sp_rate2D)
278 title('Spontaneous Emission Rate versus photon energy for 2D')
279 ylabel ('Spontaneous Emission Rate (/cm)')
280 xlabel ('photon energy (eV)')
281 grid on,
282
283 subplot(2,2,3);
284 plot (E_ph, sp_rate1D)
285 title('Spontaneous Emission Rate versus photon energy for 1D')
286 ylabel ('Spontaneous Emission Rate (/cm)')
287 xlabel ('photon energy (eV)')
```

```
grid on,

subplot(2,2,4);
barx = [1 2 3];
bary = [Jth_3D, Jth_2D, Jth_1D];
bar (barx,bary);
set(gca,'YScale','log');
set(gca,'XTickLabel',{'3D', '2D', '1D'});
for i1=1:numel(bary)
    text(barx(i1),bary(i1),num2str(bary(i1),'%2.2E'),...
                'HorizontalAlignment','center',...
                'VerticalAlignment','bottom')
end
title('Threshold Current density for different dimensionality')
ylabel ('Threshold Current Density (A/cm^2)')
xlabel ('Dimensions')
grid on,


%% Additional overlapping Plot
figure;
ax1 = gca;
get(ax1,'Position');
set(ax1,'XColor','k',...
    'YColor','b');
line(E_ph,sp_rate1D, 'Color', 'b', 'LineStyle', '-', 'Marker', '.', 'Parent', ax1, '
    DisplayName', '1D','LineWidth',4)
legend show
ax2 = axes('Position',get(ax1,'Position'),...
           'XAxisLocation','bottom',...
           'YAxisLocation','left',...
           'Color','none',...
           'YLim',[0,10*10^4],...
           'YTick',[1*10^4, 3*10^4, 5*10^4, 7*10^4, 9*10^4],...
```

```
321             'XColor','k',...
322             'YColor','r',...
323             'XTick',[],'XTickLabel',[]);
324         set(gca, 'YTickLabel', num2str(reshape(get(gca, 'YTick'),[],1),'%.d') );
325         ylabel ('Spontaneous Emission Rate (/cm.s)')
326 line(E_ph,sp_rate2D, 'Color', 'r', 'LineStyle', '-', 'Marker', '.', 'Parent', ax2,'
        DisplayName', '2D','LineWidth',4)
327 legend show
328 ax3 = axes('Position',get(ax1,'Position'),...
329             'XAxisLocation','bottom',...
330             'YAxisLocation','right',...
331             'Color','none',...
332             'YLim',[0,10*10^3],...
333             'YTick',[1*10^3, 3*10^3, 5*10^3, 7*10^3, 9*10^3],...
334             'XColor','k',...
335             'YColor','g',...
336             'XTick',[],'XTickLabel',[]);
337 line(E_ph,sp_rate3D, 'Color', 'g', 'LineStyle', '-', 'Marker', '.', 'Parent', ax3,'
        DisplayName', '3D','LineWidth',4)
338 legend show
339 ylabel ('Spontaneous Emission Rate (/cm.s)')
340 xlabel ('Photon energy (eV)')
341 xlabh = get(gca,'XLabel');
342 set(xlabh,'Position',[get(xlabh,'Position') - [0 0.2 0]]);
343 grid on,
```

snippet/sourcecode/gain1band.m

VITA

Zhihuan Wang

Place and Date of Birth: Beijing, China — 15 August 1986
Address: 3602 Hamilton St., Apt. 2, Philadelphia, PA, 19104, US
Phone: +1 (215) 2068587
email: zw78@drexel.edu

Work Experience

Present - Jun 2015
Brookhaven National Laboratory, Long Island, NY, US
Visiting Scientist
- Performed SEM/TEM imaging of as-grown and dispersed core-shell nanowires in the clean room of center for fundamental nanomaterials.
- Developed contacts of dispersed single nanowire by FIB, then characterized the device by I-V, C-V measurement and Photoluminescence spectroscopy.

Present - Mar 2012
Drexel University, Philadelphia, PA, US
Graduate Research Fellow
The focus of my research is on characterizing the extremely enhanced optical properties of core-shell nanowires and analyzing the fundamental mechanism of such significant enhancement in light absorption, emission and lasing behavior. Specifically optoelectronic characteristics and light-matter interactions of this novel nano-structure are in my interest. Meanwhile, I also participated in writing proposals for research grants from National Science Foundation, and for access permission to center for fundamental nanomaterials at Brookhaven National Lab.

Present - Mar 2012
Drexel University, Philadelphia, PA, US
Teaching Assistant
Involved dynamically in teaching responsibilities, e.g. running lectures, managing labs and carrying recitations and office hours in various courses including Electronic Devices, Analog Devices, Design for Microcontrollers, Digital Systems, Electrical Engineering Lab, Evaluation and Present Experimental Data, Linear and Dynamic Engineering System, and Statistic Analysis of Engineering System, Introduction to Physics.

Aug 2011 - Feb 2011
IM Flash Singapore LLP., Singapore
(*A Joint-Venture of Intel* and *Micron*)
Process Integration Engineer
- Written analyze report for Special Work Requests and Global Conversion to align new process recipes and tools between Singapore and US.
- Developed, maintained and improved a process module on an advance NAND Flash Memory including design rules for alternative flows.
- Optimized existing process flows and developed creative solutions to meet product requirements.
- Extracted, monitored, analyzed and reacted to inline data, param data and probe data to fix yield issues, add process margin and reduce costs.

Education

Present -	**Drexel University**, Philadelphia, PA, US
Sep 2011	Doctor of Philosophy in Electrical Engineering
	Research Field: *Solid State and Photonic Devices* — Advisor: Dr. Bahram Nabet
	Gpa: 3.93/4
Dec 2010 -	**Nanyang Technological University**, Singapore
Aug 2009	Master of Science in Electronics
	Thesis: "Numerical Characterization of Nanowire Transistors
	and Logic Gates with Parametric Variations" — Advisor: Dr. Xing Zhou
	Gpa: 4.2/5
Jun 2009 -	**Huazhong University of Science and Technology**, Wuhan, China
Sep 2005	Bachelor of Engineering in Communication Engineering
	Thesis in Chinese: "Simulation of Wireless Streaming Media Distribution
	with Performance Evaluation" — Advisor: Dr. Xu Du
	Gpa: 82/100

Awards and Certificates

2011-present	Dean's List for graduate students
	with an outstanding curriculum, Drexel University
Jan 2016	Allen Rothwarf Endowed Fellowship, Drexel University
Oct 2015	Graduate Student Domestic Travel Grant
	The Graduate College of Drexel University
Sep 2015	Finalist for Jean Bennett Memorial Student
	Travel Grant out of 200 applications, The Optical Society (OSA)
Apr 2015	Best Poster Award of Drexel IEEE Graduate Forum's
	7^{th} Annual Research Poster Symposium
Apr 2013	Best Student Poster in Physics, Drexel Research Day
Nov 2010	Best M.S. Dissertation, NTU
Aug 2009	Graduate Fellowship from Minister of Education of Singapore, NTU
May 2009	Best Engineering Undergraduate Thesis, Internet Technology
	and Engineering Research Center at HUST
Oct 2010	GRE®: 1430 (q:800;v:630) 94^{th} percentile; awa: 3.0/6.0

Publications

1. Z. Wang, B. Nabet,"Nanowire Optoelectronics" *Nanophotonics*, 4.1 (2015): -. Retrieved 17 Mar. 2016, from doi:10.1515/nanoph-2015-0025.
2. Z. Wang, B. Nabet,"Enhancement of Optoelectronic Properties of Nanowires" Submitted to Physical Review Letter, 2017.
3. K. Montazeri, Z. Wang, B. Nabet,"Plasmonic Effect of Low-Dimensional Electron Gas in Core-Shell Nanowires" in Frontiers in Optics 2017, OSA Technical Digest (online) (Optical Society of America, 2017), paper JTh2A.6.
4. Z. Wang, B. Nabet,"Light and Rate Management in Nanowires" in Frontiers in Optics 2015, OSA Technical Digest (online) (Optical Society of America, 2015), paper FW5C.6.
5. Z. Wang, M. Currie, P. Prete, N. Lovergine, B. Nabet,"Lasing from As Grown GaAs-AlGaAs Core-Shell Nanowires up to Room Temperature" in Frontiers in Optics 2015, OSA Technical Digest (online) (Optical Society of America, 2015), paper LTh2I.4.
6. Z. Wang, M. Currie, P. Prete, N. Lovergine, B. Nabet,"Room Temperature Lasing of GaAs-AlGaAs Core-Shell Nanowires Grown on Silicon Substrate" Accepted in proceeding of: 2^{nd} EOS Topical Meeting on Optics at the Nanoscale (ONS15), At Capri, Italy. Sep 17-19, 2015.

7. Z. Wang, M. Currie, P. Dianat, G. Konica, P. Prete, N. Lovergine, et al., "On Dimensional Dependence of Interaction of Light and Nano Structures," In proceeding of: Frontiers in Optics, At Orlando, FL. Oct 10-12, 2013.
8. M. Currie, Z. Wang, P. Dianat, P. Prete, I. Miccoli, N. Lovergine, et al., "Large Light Emission Enhancement in GaAs/AlGaAs CoreShell Nanowires," In proceeding of: International Conference on One-Dimensional Nanomaterials, ICON2013, At Annecy, France. Sep, 2013.
9. Zhou, X., Zhu, G. J., Srikanth, M. K., Lin, S. H., Chen, Z. H., Zhang, J. B., ... & Wang, Z. (2010). Xsim: Benchmark Tests for the Unified DG/GAA MOSFET Compact Model. Proc. Nanotech, 2, 785-788.

Poster Presentations & Panels

1. Efficiency and Transition Rate Enhancement of Quantum Well and Core-Shell Nanowire Lasers, Drexel IEEE Graduate Forums 9th Annual Research Poster Symposium, March, 2017.
2. A Novel Alternative Infrastructure for Efficient High Volume Computation, Drexel IEEE Graduate Forums 7th Annual Research Poster Symposium, April, 2015.
3. Volumetric Optical Cavity Modes Allow Room Temperature GaAs/AlGaAs Core-Shell Nanowire Lasing, Drexel Research Day, April, 2014 & Nano for Business, Lehigh University, June, 2014.
4. As-grown GaAs/AlGaAs core-shell nanowire lase at room temperature, Drexel IEEE Forum, March, 2014.
5. Strong Photoluminescence Enhancement of Single GaAs/AlGaAs Core-Shell Nanowire, Drexel Research Day, April, 2013.

Languages

Chinese:	Native Proficiency
English:	Full Professional Proficiency
French:	Basic Knowledge

Research Skills

Semiconductor Fabrication and Characterization:	Photoluminescence\Electroluminescence Spectroscopy, Scanning\Atomic\Tunneling Microscopy, THz Time-Domain Spectroscopy, Electron Beam Induced Current, Low and High-Temperature Electronic Probing and e-beam Lithography
Computer:	Microsoft Excel, Word, PowerPoint, php, mySQL, html, Matlab, Meep, Python, Adobe Photoshop and Illustrator, Sketchup, Linux, ubuntu, LaTeX

Professional & Academic Membership

Starting Jun 2015	**OSA, Member**
Starting Jun 2015	**APS, Member**
Starting Aug 2013	**IEEE, Member**

Interests and Activities

Present - Aug 2015 | **Assistant Operation Officer**, Drexel IEEE Graduate (DIG)

• Served the Graduate IEEE community for contacting companies and academic professors for sponsorship and technical talks.

•Organized and served as judge for Drexel IEEE Graduate Forum's 8^{th} Annual Research Poster Symposium

Present - Aug 2015 | **First Drexel Diversity Council Advisory Board**, Student Center for Inclusion and Culture (SCIC)

• Encouraged open communication and dialogue, collaboration and promotion of inclusive programming on campus.

•Created a space where diverse student leaders collaborate and communicate with each other and the SCIC.

Technology, Open-Source, Programming
Paradoxes in Decision Making, Behavioral Finance, Stock
Basketball, Traveling, Running